Dipartimento di Fisica e Astronomia
Corso di Dottorato di Ricerca in Fisica
CICLO XXXI

The Study of ^{22}Ne(α,γ)^{26}Mg and ^{6}Li(p,γ)^{7}Be Reactions at LUNA

Vice Coordinatore del corso:
Prof.ssa C. Sada
Supervisore:
Dr. C. Broggini

Dottorando:
Denise Piatti

Abstract

In the current work the study of the ^{22}Ne(α,γ)^{26}Mg and of the ^{6}Li(p,γ)^{7}Be reactions are presented. Both reactions were investigated at LUNA, located under 1400 m of Gran Sasso rock (Italy). The rock coverage guarantees an unprecedented reduction of the cosmic rays background.
The ^{22}Ne(α,γ)^{26}Mg reaction plays a fundamental role in the nucleosynthesis of s-nuclei in low-mass AGB stars and in massive stars. Indeed, the ^{22}Ne(α,γ)^{26}Mg reaction is the competitor of the ^{22}Ne(α,n)^{25}Mg reaction, an effective neutron source for element synthesis through s-process. The ratio between the rates of these two reactions is crucial to estimate the impact of AGB stars and massive stars on the s-nuclei abundances. Currently this ratio is affected by high uncertainty because of the wide range of values proposed for the ^{22}Ne(α,γ)^{26}Mg 395 keV resonance strength (10^{-15} - 10^{-9} eV). All the results reported in literature are derived from indirect measurements. The present study represents the first direct measurement to estimate the strength of the 395 keV resonance and its impact on the ^{22}Ne(α,γ)^{26}Mg reaction rate. Because of the low resonance strength values an high efficiency detector was installed at the gas target beamline of LUNA400kV accelerator, where the Ne gas, 99% enriched in ^{22}Ne, was irradiated with a 399.9 keV α-beam. No significant signal was detected in the ^{22}Ne(α,γ)^{26}Mg region of interest, thus an upper limit for the 395 keV resonance strength was estimated.
The ^{6}Li is an important indicator of the stellar age and of mixing processes in stars. Indeed it is progressively depleted by stars during the pre-main and main sequence phase via both ^{6}Li(p,γ)^{7}Be and ^{6}Li(p,α)^{3}He reaction. The ^{6}Li(p,γ)^{7}Be reaction was studied by many groups but a recent work renewed the interest on this reaction. A resonance like structure was observed at $E_{cm} \sim 195$ keV ($E_x \sim 5.8$ MeV) which is neither predicted by theoretical studies nor seen in previous experiments. The new excited state could explain the angular distribution of the ^{6}Li(p,α)^{3}He reaction, which requires both negative and positive parity levels contribution. In addition, the new excited state may affect the Standard Big Bang Nucleosynthesis predictions and the extrapolation to low energy of the ^{3}He(α,γ)^{7}Be cross section. The present work has the goal of investigating the existence of the 195 keV resonance and of measuring the ^{6}Li(p,γ)^{7}Be cross section down to low energies to better constrain the S-factor extrapolation at energies of astrophysical interest. The measurement was performed at the solid target beamline of LUNA400kV accelerator, where a devoted scattering chamber was installed. Six targets of different composition and thickness were irradiated at energies between 80 keV and 390 keV. In addition to the HPGe detector, used to detect γ-rays produced by the ^{6}Li(p,γ)^{7}Be reaction, a Si detector was put in place to detect the charged particles produced by the ^{6}Li(p,α)^{3}He reaction. The results of this thesis do not confirm the resonance observed at $E_{cm} \sim 195$ keV.

Sommario

Nella presente tesi sono presentati gli studi sperimentali delle reazioni ^{22}Ne(α,γ)^{26}Mg e ^{6}Li(p,γ)^{7}Be. Entrambe le reazioni sono state studiate a LUNA, che si trova sotto 1400 m di roccia del Gran Sasso, per aver un'efficiente schermatura dal fondo creato dai raggi cosmici.
La reazione ^{22}Ne(α,γ)^{26}Mg ha un ruolo fondamentale per la nucleosintesi dei nuclei tramite il processo s in stelle AGB di piccola massa e nelle stelle massicce. Infatti essa compete con la reazione ^{22}Ne(α,n)^{25}Mg, un'efficiente sorgente di neutroni per il processo s. Il rapporto tra i rates di queste due reazioni è una quantità cruciale per stimare l'impatto delle stelle AGB e delle stelle massicce sulle abbondanze dei nuclei s. Attualmente questo rapporto non è noto con accuratezza poiché il contributo della risonanza a 395 keV della reazione ^{22}Ne(α,γ)^{26}Mg è ancora incerto. Tutti i risultati di intensità riportati in letteratura per questa risonanza sono stati dedotti da misure indirette. Il presente lavoro si propone di studiare il contributo della risonanza a 395 keV sul rate della ^{22}Ne(α,γ)^{26}Mg con una misura diretta. Poichè i valori di intensità per la risonanza stanno tra 10^{-15} eV e 10^{-9} eV un rivelatore ad alta efficienza è stato installato sulla linea gassosa collegata all'acceleratore LUNA400kV. Il gas Neon, arricchito al 99% in ^{22}Ne, è sato irradiato con un fascio di particelle α con un energia di 399.9 keV. Nessun segnale significativo è stato rilevato nella regione energetica dello spettro di interesse per la reazione ^{22}Ne(α,γ)^{26}Mg, perciò è stato calcolato un limite superiore per l'intensità della risonanza a 395 keV.
Il ^{6}Li è un importante indicatore dell'età stellare e dei processi di mescolamento nelle stelle. Infatti esso viene progressivamente distrutto dalle stelle nella fase precedente e durante la sequenza principale via le reazioni ^{6}Li(p,α)^{3}He e ^{6}Li(p,γ)^{7}Be. La reazione ^{6}Li(p,γ)^{7}Be è stata studiata da molti gruppi e un recente esperimento ha riacceso l'interesse per questa reazione. Una risonanza è stata osservata a $E_{cm} \sim 195$ keV ($E_x \sim 5.8$ MeV), né prevista da studi teorici né osservata in precedenti esperimenti. Il nuovo stato eccitato potrebbe però spiegare la distribuzione angolare della reazione ^{6}Li(p,α)^{3}He, che richiede il contributo sia di livelli con parità positiva e negativa. Inoltre, il nuovo stato eccitato potrebbe avere un effetto sulle predizioni della Standard Big Bang Nucleosynthesis e sull'estrapolazione a bassa energia della sezione d'urto della reazione ^{3}He(α,γ)^{7}Be. Lo studio attuale ha lo scopo di investigare l'esistenza della risonanza a 195 keV e di misurare la sezione d'urto della reazione ^{6}Li(p,γ)^{7}Be fino a basse energie così da meglio estrapolare il fattore astrofisico, S(E), a energie di interesse astrofisico. La misura è stata svolta usando la linea solida dell'acceleratore LUNA400kV dove una camera di scattering dedicata è stata montata. Sei bersagli di diversa composizione e spessore sono stati irradiati a energie tra 80 keV e 390 keV. Assieme al rivelatore gamma HPGe, un silicio è stato usato per rivelare le particelle cariche prodotte dalla reazione ^{6}Li(p,α)^{3}He. I risultati di questa tesi non confermano la risonanza a $E_{cm} \sim 195$ keV.

Contents

Introduction

Human beings have been investigating stars since they could point their eyes to the sky at night and see all those lights appear. At first stars were classified by eye according to their color and magnitude. Then they were observed using more sophisticated instruments. Finally stars were described as physical objects.
The source of the energy emitted by stars puzzled scientists for many years. Only in 1920 thermonuclear reactions were suggested as candidates to power stars. In this year Aston discovered the defect of mass between the helium atom and four hydrogen atoms. Sir Eddington suggested that fusion of hydrogen in helium particles could explain the energy produced by stars. Some years later Gamow discovered the quantum mechanical probability for particles to tunnel through potential barriers. This definitively proved that nuclear reactions can take place at temperature of stellar core.
Most of the energy irradiated by stars is provided by nuclear reactions. From this it follows that thermonuclear reactions play a fundamental role in the evolution of stars and they are also responsible for the production of new elements. These will be emitted into the interstellar medium in different stages of stellar evolution and eventually new generation of stars will born in a continuing cycle of chemical evolution.
Stellar nucleosynthesis was first described by Hoyle in 1954. Two years later Suess and Urey presented an improved abundance distribution of the solar system isotopes. They suggested that regularities and systematics in isotopical abundances should reflect specific mechanisms of nucleosynthesis, most of them taking place in stars. Nowadays the abundances of the elements in the stellar photosphere are known with unprecedented accuracy thanks to high resolution spectrometry. Several theoretical models try to reproduce with the same precision elemental abundances but they require an accurate knowledge both of astrophysical and of nuclear inputs. One of these is the cross section of the reactions involved in the nucleosynthesis network.
Measuring the cross section is one of the main goals of nuclear astrophysics. At stellar energies nuclear reactions can only proceed via tunneling effect, therefore the typical values of cross section vary from pico- to femtobarn. The extremely low values of the cross section result in very low counting rate, down to a couple of events per month, which gets lost in the background mainly produced by cosmic rays and environmental radioactivity. Indeed in most cases the cross section is extrapolated down to energies of interest starting from data collected at high energies. The extrapolation procedure leads to high uncertainty that affects the predicted abundances. Thus direct measurements at lowest possible energies are preferable to better constrain cross section values and to reduce the uncertainty of stellar models. A great improvement in this direction was the first experiment running an accelerator

deep underground at Laboratory for Underground Nuclear Astrophysics (LUNA). The LUNA facility is shielded against cosmic radiation by 1400 m of dolomite rock of Gran Sasso, leading to a reduction of the background by orders of magnitude. This extremely low background allowed to explore for the first time the low energy domain of nuclear astrophysics.
The present thesis reports on direct measurements of the cross section of two nuclear reactions, namely the ^{22}Ne(α,γ)^{26}Mg and the ^{6}Li(p,γ)^{7}Be at LUNA.
The former has a crucial role in the s-process in massive stars and in stars experiencing the Asymptotic Giants Branch (AGB) phase. Indeed the ^{22}Ne(α,γ)^{26}Mg reaction is the competitor of the ^{22}Ne(α,n)^{25}Mg which represents a fundamental source of neutrons for s-process. In order to simulate the s-process nucleosynthesis the ratio of their reaction rates should be known with high accuracy. Actually this ratio is poorly constrained because of the large uncertainty on ^{22}Ne(α,γ)^{26}Mg reaction rate. The main reason of this uncertainty is the wide range of values attributed to the 395 keV resonance strength (10^{-9} - 10^{-15} eV). In order to fix the contribution of the 395 keV resonance on the total reaction rate the first direct measurement was performed at LUNA. Because of the small resonance strengths reported in literature an high efficiency setup was exploited. A complete description of the importance and of the experimental details of this measurement will be presented in chapter 2 as well as the analysis and the results.
The second subject of the current thesis is the ^{6}Li(p,γ)^{7}Be reaction which plays a fundamental role in different astrophysical scenarios. In pre-main sequence and in main sequence stars ^{6}Li is progressively destroyed through the ^{6}Li(p,γ)^{7}Be reaction and the ^{6}Li(p,α)^{3}He reaction. Thus detection of ^{6}Li is an important tool to understand the early evolution of stars. A recent measurement of ^{6}Li(p,γ)^{7}Be cross section shows a resonance-like structure at $E_{c.m.} = 195$ keV (corresponding to the ^{7}Be excited state $E_x \sim 5800$ keV) in contrast with theoretical predictions and previous experimental results. The new excited state could explain the ^{6}Li(p,α)^{3}He angular distribution and it may affect the extrapolation down to low energies of the ^{3}He(α,γ)^{7}Be cross section. Finally the new excited state may have some role in our understanding of the Big Bang Nucleosynthesis. The measurement performed at LUNA covered a wide range of proton beam energies, allowing to verify the existence of the resonance. The experimental details and the analysis are described in chapter 3.
The thesis is organized as following: in chapter 1 some general aspects of thermonuclear reactions and experimental astrophysics are described, then LUNA is presented. The study of the ^{22}Ne(α, γ)^{26}Mg is reported in chapter 2, in particular the first sections are devoted to describe the experimental setup and its characterization, then the data acquisition and the analysis are presented and finally the results are discussed. The third and final chapter of the thesis is focused on the study of the ^{6}Li(p,γ)^{7}Be reaction and it has the same structure of the previous.

Chapter 1

General Aspects

Stars are sustained energetically by thermonuclear reactions which are also responsible for the production of chemical elements. All but the lightest elements (from hydrogen to boron) are synthesized in stars [1].
Nuclear astrophysics aims to understand energy generation in stars and to explain the origin of the observed isotopical abundances. Several theoretical models have been developed in order to investigate the evolution of stars and to reproduce the abundances of elements. A key input value for these models is the thermonuclear reaction rate at different temperatures, which is the subject of sec. 1.1. Then in sec. 1.2 some experimental issues in estimating of the reaction rate are described. Some of these are overcome going underground as it was done for the first time by LUNA (Laboratory for Underground Nuclear Astrophysics) which is described in sec. 1.3.

1.1 Thermonuclear Reaction Rate

The reaction rate r is defined as the number of occurring reactions per unit volume and per unit time [2]:

$$r \;=\; \frac{N_R}{V \,\cdot\, t} \;=\; n_1\, n_2\, \sigma(v)\, v \;=\; n_1\, n_2\, \langle \sigma v \rangle, \tag{1.1}$$

where n_1 and n_2 are the densities of interacting nuclei and v is their relative velocity. The cross section $\sigma(v)$ represents the probability that the nuclear reaction will occur and it depends on the relative velocity. The reaction rate per particle pair is $\langle \sigma v \rangle$. In a nondegenerate stellar plasma at thermodynamic equilibrium the relative velocity of the interacting nuclei follows a Maxwell-Boltzmann distribution:

$$P(v)dv = 4\pi v^2 \left(\frac{\mu}{2\pi kT}\right)^{3/2} e^{\left(-\frac{\mu v^2}{2kT}\right)} dv\,, \tag{1.2}$$

where $\mu = \frac{M_1 M_2}{M_1 + M_2}$ is the reduced mass of the system, T is the temperature of the stellar gas and k is the Boltzmann constant.

The equation 1.2 can be written as a function of the kinetic energy of the system, $E = \frac{1}{2}\,\mu\,v^2$:

$$P(E)dE = \frac{2}{\sqrt{\pi}}\,\frac{1}{(kT)^{3/2}}\,\sqrt{E}\,e^{-\frac{E}{kT}}\,dE\,. \tag{1.3}$$

The Maxwell-Boltzmann distribution is plotted in fig. 1.1 for three different T values, each of them corresponding to a different stellar evolutionary phase. It increases linearly with the energy until it reaches a maximum at E = kT and for E > kT it drops to zero exponentially.
Using eq. 1.3 the reaction rate per particle pair, $\langle\sigma v\rangle$, can be written as:

$$\langle\sigma v\rangle = \left(\frac{8}{\pi\mu}\right)^{1/2}\frac{1}{(kT)^{3/2}}\int_0^\infty E\sigma(E)e^{-E/kT}dE\,. \tag{1.4}$$

The integral extends from E = 0 to E = ∞ because we are considering exothermic reactions with Q> 0 (Q is the difference between the initial interacting nuclei masses and the final products masses). In order to evaluate the reaction rate one should derive an analytic expression for $\sigma(E)$, which reflects the reaction mechanism. The processes of interest for this work are the charged-particle-induced reactions which are responsible for the production of isotopes up to ^{56}Fe [3]. In stellar plasma the charged-particle-induced reactions may proceed simultaneously via nonresonant mode and through resonances [3]. Resonances can be devided into narrow resonances and broad resonances. For the purpose of this work only the narrow resonances case will be discussed. Nonresonant and resonant cases will be described in the following sections.

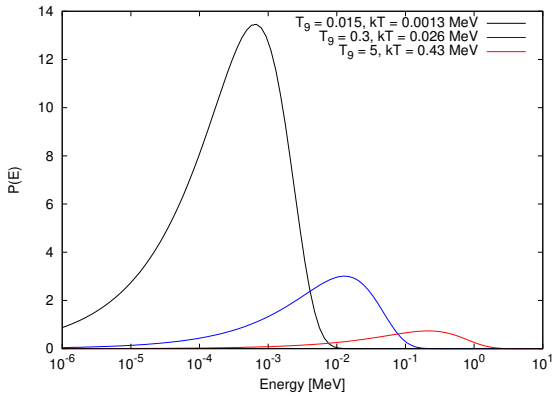

Figure 1.1: Maxwell-Boltzmann distribution at three different temperatures corresponding to different stellar evolutionary phases: main sequence, classical novae and type II supernovae.

1.1.1 The Nonresonant Case

Nuclei are positively charged and repel each other. The potential energy associated to this repulsive force is called the Coulomb potential and it ahs the form:

$$V_C(r) = \frac{Z_1 Z_2 e^2}{d}, \tag{1.5}$$

where Z_1 and Z_2 are the atomic numbers of the interacting nuclei and d is the distance between them. When nuclei are approaching the Coulomb potential increases preventing the reaction to occur. Classically a nuclear reaction could occur only when the energy of the projectile exceeds the height of the Coulomb barrier. However, at stellar temperatures, the kinetic energy of the interacting nuclei is much lower than their Coulomb repulsion. Therefore thermonuclear reactions only occur by quantum mechanical tunneling and the cross section can be written as:

$$\sigma(E) = \frac{1}{E} exp\Big(-\frac{2\pi}{\hbar}\sqrt{\frac{\mu}{2E}} Z_1 Z_2 e^2\Big) = \frac{1}{E} e^{-2\pi\eta} S(E), \tag{1.6}$$

where $1/E$ term is the quantum mechanical approximation for the classical geometrical cross section, $\sigma(E) \propto \pi\lambda^2 \propto 1/E$ (where λ is the de Broglie wavelength). $S(E)$ is referred as the S-factor and it contains all the strictly nuclear effects. The S(E) factor is a smoothly varying function of the energy. The term $e^{-2\pi\eta}$ is the Gamow factor and it represents an approximation for the s-wave transmission probability at energies well below the height of the Coulomb barrier. At low energies the Gamow factor dominates the cross section which, thus, drops even more rapidly than a simple exponential.
The reaction rate per particle pair can be written, combining eq. 1.4 and eq. 1.6, as:

$$\langle \sigma v \rangle = \Big(\frac{8}{\pi\mu}\Big)^{1/2} \frac{1}{(kT)^{3/2}} \int_0^\infty S(E) e^{-2\pi\eta} e^{-E/kT}\, dE\,, \tag{1.7}$$

The integrand is the convolution of Coulomb barrier penetrability ($e^{-2\pi\eta}$) and the Maxwell-Boltzmann energy distribution ($e^{-E/kT}$) which results in a peak, the Gamow peak in fig. 1.2.
The Gamow peak represents the energy window over which most of the thermonuclear reactions occur. It depends on interacting nuclei mass and charge and on the temperature of the stellar environment of interest. The Gamow peak can be approximated by a gaussian function:

$$(e^{-2\pi\eta} e^{-E/kT}) = I_{max} \cdot exp\left[-\left(\frac{E - E_0}{\Delta/2}\right)^2\right]. \tag{1.8}$$

In this approximation E_0 corresponds to the maximum of the gaussian and it is called effective burning energy. $(E_0 \pm \Delta/2)$ is the energy window wherein thermonuclear reactions take place.

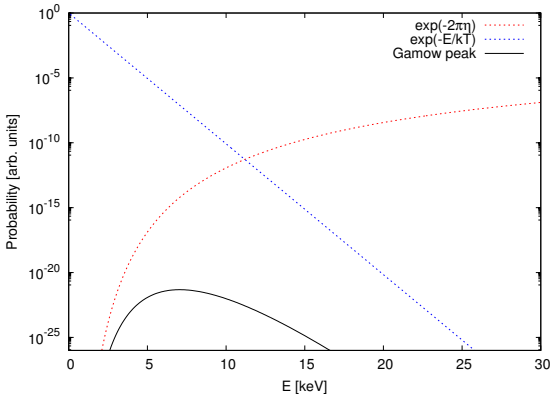

Figure 1.2: The gamow peak for ^{6}Li(p,γ)^{7}Be reaction at energies corresponding to T = 5 MK. At T > 3 MK pre-main-sequence stars ignite lithium [4].

1.1.2 The Case of Isolated and Narrow Resonances

A nuclear reaction proceeds through a resonance if the following condition is fullfilled:

$$Q + E_r = E_x. \tag{1.9}$$

The left side of eq. 1.9 is referred as the entrance channel and it is the sum of the Q value and the energy of the projectile E_r in the center of mass system. The right side corresponds to the energy of the compound nucleus excited state populated through the reaction. Indeed the resonant mechanism is said to be a two-steps process. The compound nucleus is produced in an excite state, step one, and then it decays to lower states, second step. The cross section is proportional to the probability of each step to occur which is usually represented by a partial width Γ_i:

$$\sigma \propto \Gamma_a \Gamma_b, \tag{1.10}$$

where Γ_a is the partial width for the production of the compound nucleus and Γ_b is the probability for the compound nucleus to decay. Partial widths and the resulting cross section can vary widely depending on the properties of the nuclear states involved. An excited state may decay through multiple transitions chains and the sum of the partial widths of all open decay channels and Γ_a is the so called resonance width (Γ). A resonance is narrow if $\Gamma \ll E_r$ and it is isolated if the separation of nuclear levels is large compared to their width. The full analytical expression of the cross section, in case of isolated and narrow resonances, is the Breit-Wigner formula:

$$\sigma(E) = \pi\left(\frac{\lambda}{2\pi}\right)^2 \frac{2J+1}{(2J_1+1)(2J_2+1)} (1+\delta_{1\,2}) \frac{\Gamma_a \Gamma_b}{(E - E_r)^2 + (\Gamma/2)^2} \tag{1.11}$$

which can be devided in three components:

- The geometrical cross section is $\pi\left(\frac{\lambda}{2\pi}\right)^2$.
- The statistical factor $\frac{2J+1}{(2J_1+1)(2J_2+1)}\,(1+\delta_{1\,2})$ takes into account the distribution of the spinorbit among the nuclei involved in the reaction. J_1 is the projectile spin-orbit while J_2 is the target. J is the angular momentum of the excited state of the compound nucleus. If the particles in the entrance channel are identical the cross section is enhanced by a factor 2. This effect is included through the term $(1 + \delta_{12})$.
- The last term of eq. 1.12 reflects the description of the damped oscillator response which is known to be resonant.

Inserting the Breit Wigner formula for the cross section (σ_{BW}) in the definition of the reaction rate per particle pair one obtains the contribution of the resonance to the reaction rate per particle:

$$\langle \sigma v \rangle = \left(\frac{8}{\pi\mu}\right)^{1/2} \frac{1}{(kT)^{3/2}}\, E_r\, exp\left(-\frac{E_r}{kT}\right) \int_0^\infty \sigma_{BW}(E) dE\,, \tag{1.12}$$

where the Maxwell-Boltzmann function $E\, exp\left(-\frac{E}{kT}\right)$ varies very little around the resonance energy and it was taken outside the integral.
The integrand in eq. 1.12 is also called resonance strength, defined as:

$$\omega\gamma \;=\; \frac{2J+1}{(2J_1+1)(2J_2+1)}\,(1+\delta_{1\,2})\,\frac{\Gamma_a\Gamma_b}{\Gamma}. \tag{1.13}$$

Finally the resonance contribution to the total reaction rate per particle pair can be expressed as:

$$\langle \sigma v \rangle \;=\; \left(\frac{2\pi}{\mu kT}\right)^{3/2} \hbar^2 (\omega\gamma)_r\, exp\left(-\frac{E_r}{kT}\right). \tag{1.14}$$

In case of several resonances their contributions to the reaction rate are summed. The most important resonances are those in the Gamow window and the resonances with E_r near kT dominate the stellar reaction rate.
At this point an analytic description of σ for the cases of interest was obtained. However measuring the experimental quantities related to the cross section at astrophysical energies is still difficult. In the next section the main experimental issues are described.

1.2 Underground Measurements

The cross section at astrophysical energies ranges from pico- to femtobarn. Because of these low values of the cross section its measurement is often challenging in surface

laboratories because the signal to background ratio is too small. Indeed the cross section is extrapolated to stellar energies starting from the observed data at higher energies. However the extrapolation is an icy procedure, leading to substantial uncertainties. At low energies the extrapolation may not take into account the contribution of possible unknown narrow or broad sub-threshold resonances. Thus direct measurements would be preferable. Going underground allows to perform the measurement down to low energy in a ultra low background environment.
In the next section the background in γ spectra will be treated widely because of interest for the reactions under study. The background populating the experimental γ spectra can be classified into the environmental background and the beam induced background, which are described in the next sections. Finally sec. 1.3 is devoted to LUNA.

1.2.1 Environmental Background

Environmental background includes the contributions by cosmic rays and by the natural radioactivity of experimental hall and setup materials.
The Earth's atmosphere is constantly exposed to cosmic particles rain, mainly protons and alphas. Most of these particles interacts with the atmosphere particles producing pions which decay via gamma channel ($\pi^0 \rightarrow 2\gamma$) or (anti)muons-(anti)neutrinos production ($\pi^{\pm} \rightarrow \mu^{\pm} + \nu_{\mu}(\bar{\nu_{\mu}})$). While nucleonic component of cosmic rays background can be reduced using passive and active shields, muons are highly penetrating particles. In addition muons can produce neutrons by spallation reactions. Finally they can activate nuclei in the detector and in the shielding materials. Several studies were devoted to investigate technical methods to reduce the muon induced background [5–8]. It was found that the most efficient way to suppress the muon-induced background is to perform experiments in underground laboratories [9]. Deep underground the muon-induced background is reduced of several order of magnitude. However, deep underground a second source of neutrons, which is buried on the surface by the cosmic rays, emerges: spontaneous fission of ^{238}U and (α, n) reactions which take place in the surrounding rock and in the concrete walls of the experimental hall [10]. This residual flux of energetic neutrons affects spectra up to 12 MeV. Fast neutron background can be mitigated using moderators [11].
The second source of the environmental background consists of the direct and indirect effects of long-lived radioisotopes in the experimental hall and setup, which affect both surface and underground γ spectra. They can be reduced by using suitable materials for shields, detectors and targets [12]. In case of shielded setup an additional problem may be the bremsstrahlung events generated by β emitters in the shield itself, for example the ^{210}Bi, decay product of the ^{210}Pb, in lead bricks [13]. In this case the solution is limiting the level of ^{210}Pb in lead shields.

Another problem is radioactive radon gas, which emits a number of γ rays when decaying. This can be solved enclosing the target and the detectors in an anti-radon box, flushed with radon free gas. Radioisotopes and bremsstrahlung effects populate the low energy part of a spectrum ($E_\gamma \leq 3.7$ MeV) [14].

1.2.2 Beam Induced Background

Contaminants in the experimental setup which are reactive to the incident ion beam generate the beam induced background. For example the most troublesome contaminant in case of proton beams is the ^{19}F, which produces two γ rays at 6 and at 7 MeV via ^{19}F(p,$\alpha\gamma$)^{16}O reaction. This reaction has a very high cross section dominated by the resonances at 224 keV and at 340 keV [2]. Other examples are the ^{11}B(p,γ)^{12}C (resonance at E_p = 163 keV) and the ^{18}O(p,γ)^{19}F (resonance at 151 keV). Both these reactions produces γ-rays in the energy region between 4 MeV and 16 MeV of interest for thermonuclear reactions. In addition the 278 keV resonance γ-rays of the ^{14}N(p,γ)^{15}O reaction lay between 5 MeV and 7 MeV and at $E_\gamma < 3.7$ MeV. At higher energy than 16 MeV a source of beam induced background may be the ^{7}Li(p,γ)^{8}Be reaction. These are some examples but the list of the sources of beam induced background may change depending on the region of the spectrum and the beam energies of interest.
If a contaminant reaction is recognized in the spectrum a cleaning procedure must be applied to the setup. For the case of carbon, deuterium and oxygen, which may be found in the beam line as residual gases, in order to avoid these elements to be transported to the target surface a cold trap or a high efficiency vacuum system can be used. If the cleaning procedure could not improve the situation then the beam induced background must be subtracted with proper methods [15].

1.2.3 LUNA

The Laboratory for Underground Nuclear Astrophysics (LUNA) was the first laboratory in the world to offer the possibility to measure cross section down to astrophysical energies in an extremely low background environment.
LUNA facility is located at the Italian National Gran Sasso underground laboratory (LNGS), operated by the Italian National Institute for Nuclear Physics (INFN), see fig. 1.3. The dolomite rock overhead the experimental hall (1400 m equivalent to 3800 meters of water) is a natural shield against cosmic rays flux. Indeed at LUNA laboratory the nucleonic component of cosmic rays background is completed suppressed. The expected reduction of the muons flux and the muons-induced neutrons is of a factor $\sim 10^8$, see fig. 1.4. However it was observed that the muon-induced neutron flux is reduced only of a factor $\sim 10^6$ at LUNA laboratory [14], see fig. 1.5. This excess of neutrons at E_γ 3 MeV is due to the ^{238}U and ^{232}Th spontaneous fission

together with (α, n) reactions, which take place in the surrounding rock where the α-particles are provided by the natural decay of the rock element [10].

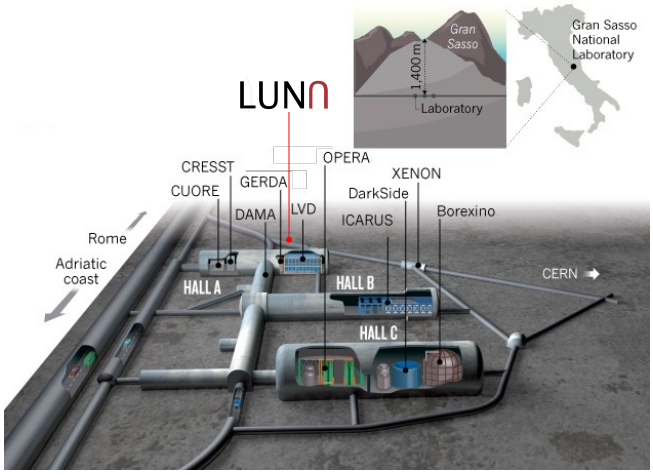

Figure 1.3: Current LUNA accelerator location inside the Gran Sasso laboratory.

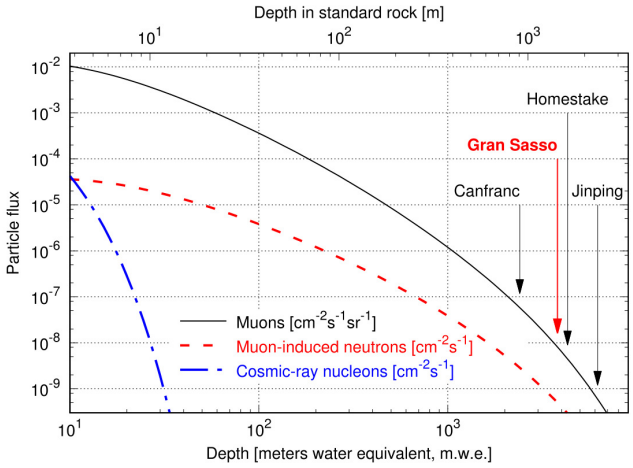

Figure 1.4: Muon, muon-induced neutron and cosmic-ray nucleon fluxes as function of depth. In addition to Gran Sasso, also other laboratories with underground accelerator projects are indicated. The underground depth is expressed in meters water equivalent. [16].

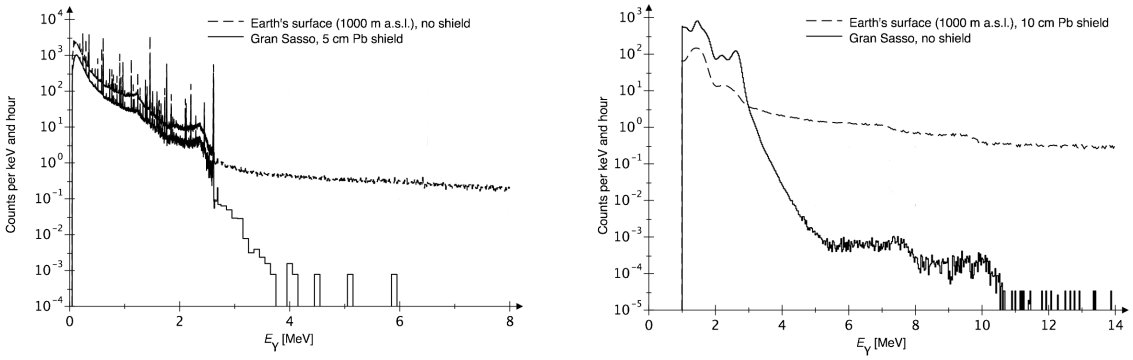

(a) (b)

Figure 1.5: a): Laboratory background measured with the germanium detector: at the surface with a lead shield of 10 cm thickness and underground at LNGS [14]. b): The same as in a) but acquired with the BGO scintillator detector [14].

At $E_\gamma < 3.7$ MeV the background due to radioactive isotopes in the rocks and in laboratory hall can be reduced adding shields to detectors fig. 1.6 [17]. The radioactive radon gas can be dealt with by enclosing target and detector in an airtight anti-radon box that is flushed with radon-free gas [16].

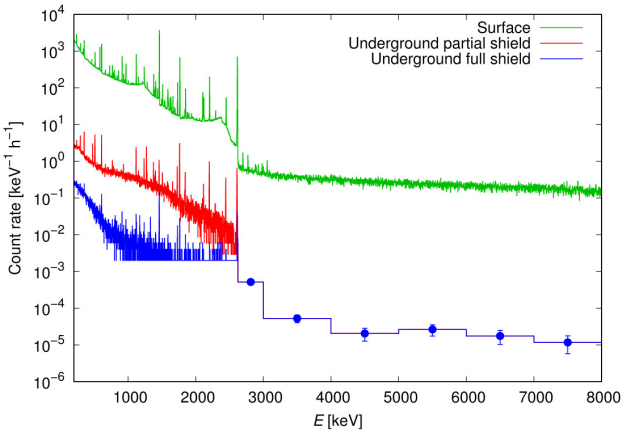

Figure 1.6: Laboratory background measured with the germanium detector: at the surface, underground at LNGS with the full shield (Cu+Lead+anti-Rn) and with the partial shield (Cu+Pb and a second Ge detector inside the shield. [16].

Recently for the study of the ^{17}O(p,α)^{14}N reaction the advantage of going underground to measure also reactions producing charged particles was demonstrated [17].

In particular it was found that in the region of interest, indicated with vertical dashed lines in fig. 1.7, the background was reduced of a factor 15. However an overall reduction of the background is evident in fig. 1.7 except for the peak around 5 MeV which is produced by intrinsic alpha activity in the silicon detector [17].

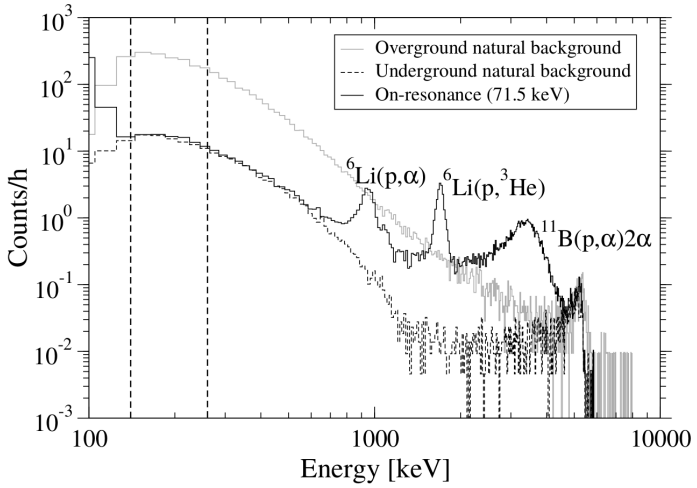

Figure 1.7: Background spectra taken overground (gray line) and underground (dashed line) showing a factor of 15 background reduction in the region of interest (vertical lines) for the E_r = 64.5 keV resonance in ^{17}O(p,α)^{14}N. The full energy spectrum (black line) taken on resonance at E_p = 71.5 keV with labeled peaks from beam-induced reactions. The peak around 5 MeV is ascribed to intrinsic alpha activity in the silicon detectors [17].

Thanks to the unprecedented low environmental background, see fig. 1.6, LUNA can explore the low energy domain of nuclear astrophysics. LUNA started its activity in 1991 as a pilot project with a 50kV electrostatic accelerator [18]. The scientific program of the 50kV was focused on the study of two fundamental reactions for the hydrogen burning via the proton-proton (pp) chain: the ^{3}He(^{3}He,2p)^{4}He reaction [19] and the ^{2}H(p,γ)^{3}He reaction [20]. This first homemade accelerator was operated from 1991 to 2001 and it included a duoplasmon ion source for intense hydrogen and helium beams. It was a hot cathode plasma source combined with an intense axial magnetic field in the discharge region which provided a well focused ion beam. The short lifetime of the ion source made the experiment-maintenance intensive. In order to solve this issue in 2001 the activity was moved to a new commercial 400kV accelerator by High Voltage Engineering Europe.

The 400kV accelerator is embedded in a tank filled with an insulating gas mixture composed of N_2 and CO_2 at a pressure of 20 bar, see fig. 1.8b. The ion source is directly mounted in the accelerator tube and it provides high intensity ^{1}H$^+$ and ^{4}He$^+$ beams. It consists of a glass tube containing hydrogen or helium gas, see fig. 1.8a.

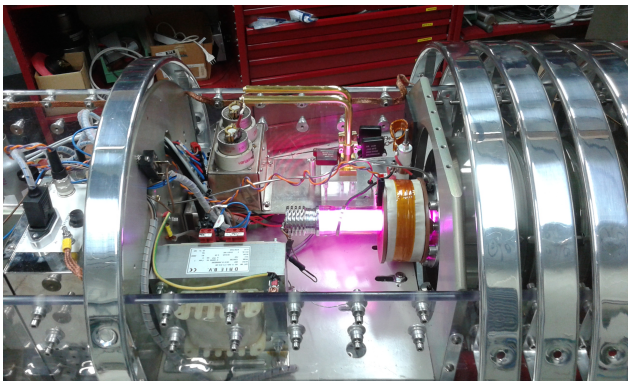

(a)

(b)

Figure 1.8: a): LUNA400kV ion source. b): LUNA400kV accelerator.

A radio frequency field is applied, ionizing the gas inside the tube. The ions are then extracted from the ion source and accelerated. The high voltage is generated by an Inline-Crockcroft-Walton power supply located inside the tank. A RC-filter and an active feddback loop based on a chain of resistors stabilize the high voltage at the terminal. The accelerator tube is equipped with an adjustable shortening rod and a magnetic X-ray suppression system. The radiation level in the control room is kept below 0.5 mS/h thanks to 5 mm thick Pb shield around the tank. The current at the exit of the accelerator is of 1 mA for H^+ and of 500 μA for He^+. The beam can be delivered to a solid target or to a gas target thanks to an analyzer magnet installed next to the accelerator exit. The proton beam current on the target is typically 500 μA in the energy range 150-400 keV. During the calibration of the accelerator the energy stability was estimated in 5 eV/h and the energy spread of the beam was found to be $\leq$ 100 eV [21]. The accelerator, the experimental equipment, and

the data handling is controlled by a PLC based computer, which allows for a safe operation over long periods of running time without the constant presence of an operator on site.
The scientific program of the 400kV covered different astrophysical scenarios. One of the first reactions investigated using LUNA400kV was the ^{3}He(^{4}He,γ)^{7}Be reaction on whose cross section the ^{7}Be and ^{8}B neutrinos production in the Sun depends almost linearly [22]. The LUNA collaboration activity was devoted also to the CNO cycle, for example with the study of the ^{14}N(p,γ)^{15}O reaction [23] and of the ^{17}O(p,α)^{14}N reaction [17]. In addition the ^{22}Ne(p,γ)^{23}Na reaction of the NeNa cycle [24], and the ^{23}Na(p,γ)^{24}Mg reaction of the MgAl cycle [25] were studied. Finally the ongoing measurements and analysis at LUNA400keV are focused on four reactions: the ^{2}H(p,γ)^{3}He reaction at Big Bang Nucleosynthesis energies, the ^{22}Ne(α,γ)^{26}Mg reaction and the ^{13}C(α,n)^{16}O reaction, which play a fundamental role in determining the s-process in AGB stars and finally the ^{6}Li(p,γ)^{7}Be reaction relevant in many astrophysical scenarios.
The next step is exploring helium and carbon burning. This will be reached using a 3.5MV accelerator which is going to be installed at LNGS within 2019.

Chapter 2

The Study of the ^{22}Ne(α,γ)^{26}Mg Reaction at LUNA

2.1 Astrophysical Motivations

The ^{22}Ne(α,γ)^{26}Mg reaction is mainly involved in two stellar scenarios. First it competes with the ^{22}Ne(α,n)^{25}Mg reaction which is an efficient source of neutrons for s-process in low-mass asymptotic giant branch (AGB) stars [26], and in massive stars (with initial mass $M_i > 8$ $M_\odot$) [27]. Then it was recently found that the uncertainty of the ^{22}Ne(α,γ)^{26}Mg reaction rate affects the nucleosynthesis of isotopes between ^{26}Mg and ^{31}P in intermediate-mass AGB stars [28]. Both the above cases are described in the following sections.

2.1.1 The s-process

The s-process produces half of all elements heavier than iron [29], it consists of sequences of neutron captures that are slower than the competing β decay. The typical neutron densities for s-process to occur are $N_n \leq 10^{11}$ cm^{-3}. The isotopes produced are close to the stability valley and lay in the mass region $60 \leq A \leq 204$. In particular isotopes with $A \leq 90$ are the so called *weak* component of the s-process. Those isotopes are produced in massive stars [30]. On the other hand the low-mass AGB stars are the nuclear production sites for the *strong* component of the s-process ($A > 90$) [31].
The ^{22}Ne(α,n)^{25}Mg reaction is an efficient neutron source for s-process in massive stars and in AGB stars, both scenarios are described in the next sections. It has been argued that the ^{22}Ne(α,γ)^{26}Mg reaction may compete strongly at low temperature with the neutron channel [30]. A precise knowledge of the ^{22}Ne(α,n)^{25}Mg reaction rate together with its competitor reaction is required in order to constrain the several models built to reproduce the observed s-isotopes abundances. The

^{22}Ne(α,γ)^{26}Mg reaction is investigated by the present work. A devoted experiment will be performed at LUNAMV to study the ^{22}Ne(α,n)^{25}Mg reaction. Because of their impact on stellar nucleosynthesis and thus on the chemical evolution of galaxies both the ^{22}Ne(α,γ)^{26}Mg and the ^{22}Ne(α,n)^{25}Mg reactions were inserted in the Chemical Elements as Tracers of the Evolution of the Cosmos (ChETEC) Action program. The ChETEC Action is supported by COST (European Cooperation in Science and Technology) and it aims to coordinate the research efforts astronomy, astrophysics, and nuclear physics in all Europe.

Low-mass AGB Stars

The production of isotopes with $A > 90$ takes place in low-mass AGB stars. AGB stars are the final evolution stage of low- and intermediate-mass stars driven by nuclear burning. This phase of the stellar evolution is characterized by nuclear burning of hydrogen and helium in thin shells on top of the electron-degenerate core of carbon and oxygen, or for the most massive super-AGB stars a core of oxygen, neon, and magnesium. AGB stars are sites of rich nucleosynthesis thanks to the complex mixing mechanisms which take place in the H and He shells and in the convective envelope [26]. Furthermore they are sites of mass loss thus AGB stars play an important role in the chemical evolution of galaxies [32]. A precise model of these stars would be of great importance in our understanding of the processes taking place inside these stars and of the isotopes abundances in the Galaxy.
The accepted evolution up to the AGB phase involves stars with an initial mass $M_i > 1.8\,M_\odot$, which, after having run out of the H fuel, experienced the red giant branch phase (RGB). Then they start to ignite He, ash of the H burning phase, while the residual H from the H-burning phase moved to the outer layers. The He-core burning phase is about a factor of 10 shorter than the H-core burning phase ($t_{He} \sim 10^6$ ys). He-core burning leaves a C/O core behind that is surrounded by both a He- and a H-burning shell. For stars with initial mass lower than 8 $M_\odot$, as low-mass AGB stars whose initial mass is lower than $4\,M_\odot$, carbon does not ignite, and the C/O core starts to contract and becomes increasingly electron-degenerate, A schematic structure of a low-mass AGB star is presented in fig. 2.1.
During the early AGB phase, the He shell burning dominates nuclear production. It burns outward in mass and reaches the H shell. At that point, nuclear energy release is dominated by the H shell and interrupted periodically by He thermonuclear runaway. These He-shell flashes initiate a complex series of convective and other mixing events. In AGB stars the He-shell flash arises after a prolonged quiescent interpulse phase during which the dormant He shell accretes helium from the dominant nuclear source, the H shell. The large energy generation of the He shell during the flash is driven mainly by the triple-α reaction and induces a temporary convective instability throughout the region between the shells, called *Pulse Driven Convective Zone* (PDCZ), see fig. 2.1. During the PDCZ phase the ingested ^{14}N (ash of the

H burning via CNO cycle) is converted into ^{22}Ne, which is accumulated at the base of the He shell over all thermal pulses. Because of the high temperatures reached at its base ($T \geq 0.25$ GK) the PDCZ has a key role in AGB nucleosynthesis. The ^{22}Ne(α,n)^{25}Mg reaction can take place only at the bottom of the PDCZ, while the ^{22}Ne(α,γ)^{26}Mg reaction is active even at lower temperatures [26]. The ratio between the two reactions rate is crucial to determine the amount of neutrons available for the s-process. In the current models the neutrons are released with high density ($\log(N_n) \sim 9 - 11$) in a short burst, which lasts for only about a year. Then a neutron-density tail follows for a few years, depending on model assumptions. In fig. 2.1 the sites and the evolution of both the ^{22}Ne(α,n)^{25}Mg reaction and the ^{13}C pocket are indicated. In addition in the right panels of fig. 2.1 the strength and time-dependence of the neutron density produced by the ^{22}Ne(α,n)^{25}Mg reaction and by ^{13}C(α,n)^{16}O reaction.
During the advanced AGB phase the increasing mass loss leads to the ejection of the envelope, enriching the interstellar medium of the products of the AGB nucleosynthesis.

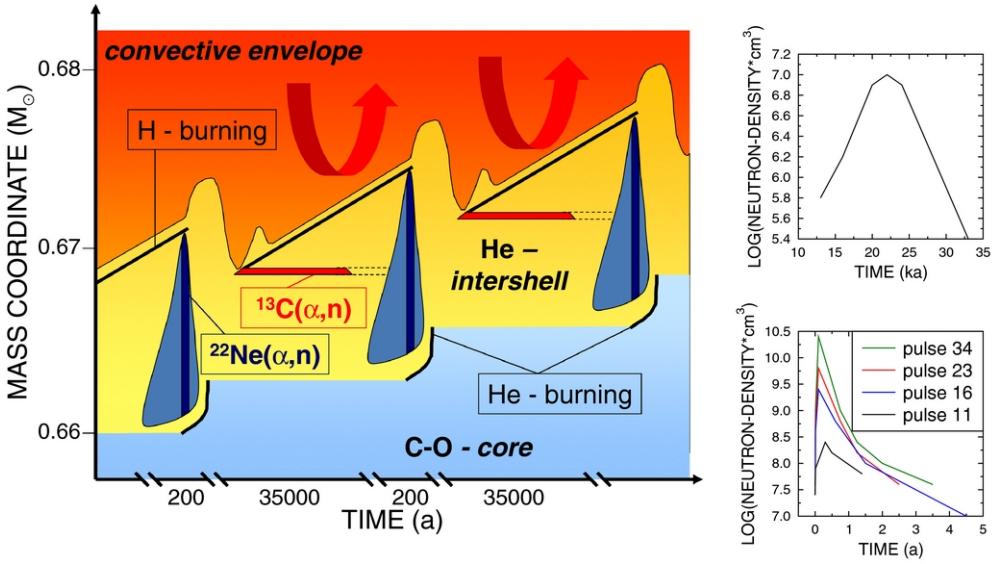

Figure 2.1: Left: Schematic structure (y-axis) and evolution (x-axis) of a low-mass AGB star showing recurrent H and He burning episodes with indications for the related s-process sites. Right: the evolution of neutron density by (α, n) reactions on ^{13}C (top right) and on ^{22}Ne (bottom right). Figure from [33].

Massive Stars

The s-process in low-mass AGB stars fails to reproduce the s-isotopes abundances below A = 90. This gap is actually closed by the complementary s-process taking place in massive stars with initial mass $M_i > 8$ $M_\odot$.
In massive stars the s-process is driven by the ^{22}Ne(α,n)^{25}Mg reaction, first during convective core He burning at $T \sim 3 \cdot 10^8$ K and subsequently during convective shell C burning at 10^9 K [27]. The available ^{22}Ne is produced from the initial CNO isotopes, which are converted to ^{14}N during the H-burning phase, and then to ^{22}Ne via ^{14}N(α,γ)^{18}F($\beta^+\nu$)^{18}O(α,γ)^{22}Ne during He-burning. During this latter phase both the ^{22}Ne(α,n)^{25}Mg and the ^{22}Ne(α,γ)^{26}Mg occur. When the He is exhausted in the core, not all the ^{22}Ne is consumed [34]. Thus the two reactions are re-activated during shell C-burning, where the α particles are provided by the ^{12}C(^{12}C,α)^{20}Ne reaction [35]. It was showed that the s-process occurs during convective shell C-burning at a high neutron density and with a neutron exposure comparable with the one in the previous He-burning core [36].
The predictions on s-process in massive stars can be more difficult and more model dependent than in the case of AGB stars, for which, however, several parameters are needed to take into account the several process taking place in the outer layer (for example thermal pulses and mixing processes). As a matter of fact massive star evolution proceeds through all the burning phases up to the Si burning stage. The iron core cannot be ignited and the star explodes as a Supernova Type II [33]. The chemical composition of the core up to a mass of 3.5 $M_\odot$ (for example for a star of 25 $M_\odot$) is modified during explosive nucleosynthesis in the supernova. Any previous s-process signature is destroyed. However, the ejecta still contain an important mass fraction ($\sim$2.5 $M_\odot$) that preserves the original s-process abundances produced by the hydrostatic nucleosynthesis phases of the pre-supernova evolution. On the other hand the He shell material is further processed during the supernova explosion. Indeed, a significant amount of ^{22}Ne is still present at the shock wave passage, and the high neutron flow generated by the ^{22}Ne(α,n)^{25}Mg can significantly modify the pre-supernova abundance signature in this small region [37]. In order to build a model of the nucleosynthesis network during the evolution of a massive stars the reaction rate of the processes involved must be known very precisely.

2.1.2 Intermediate-mass AGB Stars Nucleosynthesis

Magnesium is one of the few elements for which we can obtain isotopic information from stellar spectroscopy. The isotopic ratio between ^{24}Mg, ^{25}Mg and ^{26}Mg was derived from high-resolution spectra of cool dwarfs in the thin and thick disk of the Galaxy [38] and of giants stars in the globular cluster (GC) NGC 6752 [39]. The observed ratios are not in complete agreement with the Galactic Chemical Evolution models (GCE), which consider the C and the Ne shell in massive stars as the

main sites of production of the three stable isotopes of Mg. In order to fill the gap between models and observations intermediate-mass AGB stars were proposed as site for the synthesis of Mg isotopes [40].
Intermediate-mass AGB stars have a similar evolution as for low-mass AGB stars. However, according to model calculations, thermal-pulse AGB evolution is strongly mass dependent thus their evolution is not completely identical. For example s-process is present only in low-mass AGB stars. Intermediate-mass AGB stars, on the other hand, experience the Hot Bottom Burning (HBB) while low-mass AGB stars do not [26].
The HBB corresponds to the H-shell burning condition in which the outer part of the shell is included in the envelope convection. The H shell has enhanced access to fuel, convectively mixed into its outer layers. This leads to an overluminosity of massive AGB stars compared to the core-mass luminosity relation derived from evolution calculations of low-mass AGB stars. The HBB is important for nucleosynthesis because it occurs at high temperature thus it sustains proton capture nucleosynthesis, for example at $T \geq 60\,MK$ the NeNa and the MgAl cycles are activated. The latter is important for the consumption of ^{24}Mg in intermediate-mass AGB stars, thus it is important for the final abundance of the ^{24}Mg. The other two isotopes, ^{25}Mg and ^{26}Mg, are produced by the $^{22}Ne(\alpha,n)^{25}Mg$ reaction and by the $^{22}Ne(\alpha,\gamma)^{26}Mg$ reaction respectively. Both reactions take place in the He shell during the thermal pulse as already described for the low-mass AGB stars. The final abundances of ^{25}Mg and ^{26}Mg depend also on the $^{25}Mg(n,\gamma)^{26}Mg$ reaction, for which neutrons are provided by the $^{22}Ne(\alpha,n)^{25}Mg$ reaction.
A recent sensitivity study on the production of Mg isotopes in intermediate-mass AGB stars showed the lack of knowledge of several phenomena taking place in AGB stars, for example convective mixing events, but it also reported the strong dependence of results on the reaction rate used for the $^{22}Ne(\alpha,n)^{25}Mg$ and the $^{22}Ne(\alpha,\gamma)^{26}Mg$ reactions [28]. Moreover, the uncertainty on the final abundance of Mg isotopes and of isotopes up to ^{31}P was strongly related to the uncertainties on $^{22}Ne(\alpha,\gamma)^{26}Mg$ reaction rates. Indeed as it was already noted by [41] both the two key α-capture reaction rates suffer from large uncertainties at the stellar energies appropriate for AGB stars. In particular the uncertainty increases up to 2 order of magnitude for the $^{22}Ne(\alpha,\gamma)^{26}Mg$ reaction rate and up to 1 order of magnitude for the $^{22}Ne(\alpha,n)^{25}Mg$ reaction rate at $T \leq 0.3$ GK, at which the (α,γ) channel dominates. This affects specifically the reliability for nucleosynthesis predictions in low temperature environmental. At higher temperature the $^{22}Ne(\alpha,n)^{25}Mg$ reaction dominates, however the data available for the rates of both the α-capture reactions are not enough stringent to define the exact temperature of the cross-over. In the paper a new reaction rate was suggested for the $^{22}Ne + \alpha$ reactions based on available data for the ^{26}Mg excited states. The new calculated final abundances for the three isotope of Mg are compared with those obtained using the reaction rates

for the ^{22}Ne(α,n)^{25}Mg and for the ^{22}Ne(α,γ)^{26}Mg reactions recommended in [42]. The abundances of Mg isotopes were calculated and compared for different metallicity model of a 5 $M_\odot$ AGB star. The new yields of ^{25}Mg were smaller than those predicted using reaction rates by [42]. In particular increasing the metallicity the discrepancy increases from 20% up to 45%. For the yields of ^{26}Mg the reduction was between 9% and 16% going to lower metallicity. The lower uncertainty of the recommended reaction rate resulted in smaller uncertainties of the abundance of ^{25}Mg and ^{26}Mg compared to those obtained using the previously adopted reaction rate compilation (from $\sim$400% to less than 30%). In addition the uncertainty on the production of all isotopes between ^{22}Ne and ^{31}P was reduced, for example the uncertainty on the production of P was at a level of 35% while using NACRE the uncertainty was of 400%. One of the paper aim was to encourage future work to reduce the uncertainties on $^{22}\mathrm{Ne}+\alpha$ reactions rates in order to improve the AGB models situation.

2.1.3 State of Art

Because of the importance of s-process as well as the impact of AGB star nucleosynthesis on galactic chemical evolution, as described in previous sections, several studies were devoted to investigate the ^{22}Ne(α,n)^{25}Mg reaction and its competitor, the ^{22}Ne(α,γ)^{26}Mg reaction. Because of the low cross sections involved most of the studies used indirect methods.
It is known that the non-resonant contribution is small and the ^{22}Ne(α,γ)^{26}Mg reaction rate is dominated by mainly two resonances at $E_\alpha = 395$ and 831 keV. A recent study found that the hypothetical 637 keV resonance cannot play any role in the $^{22}\mathrm{Ne}+\alpha$ reactions because of the unnatural parity assigned to the corresponding excited state $E_x = 11154$ keV [43]. Only low upper limits are reported in literature for the resonances between 395 and 831 keV, thus they do not contribute to the total reaction rate. The $E_\alpha = 831\,\mathrm{keV}$ ($E_x = 11318$ keV) resonance strength is known within 6% of uncertainty [44]. This resonance is common to both the $^{22}\mathrm{Ne}+\alpha$ reactions.
The most debated contribute to the ^{22}Ne(α,γ)^{26}Mg reaction rate is from the resonance at $E_\alpha = 395$ keV ($E_x = 10950\,\mathrm{keV}$). Indeed, the resonance strength values reported in literature for the 395 keV resonance lay in a 6 orders of magnitude wide range, see table 2.1.
The reaction rates for the $^{22}\mathrm{Ne}+\alpha$ fusion processes are determined by the level structure of the compound nucleus ^{26}Mg above the α-threshold at $T_\alpha = 10615\,\mathrm{keV}$ and near the neutron threshold $T_n = 11093\,\mathrm{keV}$. The first survey to observe the $E_x = (10950 \pm 3)\,\mathrm{keV}$ excited level for ^{26}Mg was performed in 1976 exploiting the inelastic proton scattering pattern from the ^{26}Mg(p,p') ^{26}Mg reaction [45]. Some years later the ^{22}Ne(^{6}Li,d) α-transfer reaction was exploited to investigate the spin-

parity value (J^π) and the spectroscopic factor (S_α) of the ^{26}Mg levels of interest for resonant α-capture on ^{22}Ne [46]. The angular distribution for the ^{22}Ne(^{6}Li,d)^{26}Mg transitions to the populated states in^{26}Mg was used to assign the spin-parity. For the excited state at 10950 keV a $J^\pi = 3^-$ was suggested but $J^\pi = 2^+$ and 4^+ could not be excluded. The S_α was found to be 0.025 relative to the $E_\alpha = 831$ keV resonance. The resonance strength was calculated for each spin and parity value. The suggested value for the resonance strength of $1.7 \cdot 10^{-13}$ was calculated for $J^\pi = 3^-$, while the lower and upper limits were calculated for $J^\pi = 4^+$ and $J^\pi = 2^+$ respectively, see tab. 2.1.
The results of [46] were adopted in NACRE reaction rate compilation [42], but slightly lower values were assigned to the suggested resonance strength and for the upper limit. The lower limit was put to zero without any explanations [42]. NACRE reaction rate compilation was the one adopted for the astrophysical models, for example to describe the nucleosynthesis in intermediate-mass AGB stars. However a recent study on the production of Mg in AGB stars proposed a new reaction rate based on data available in literature [28]. The astrophysical impact of uncertainties of $^{22}\mathrm{Ne} + \alpha$ reactions rates shown in [28] incites to perform a new attempt to fix the level structure of ^{26}Mg and the possible corresponding resonances strengths.
The new study was performed with the same method as in [46] but with higher energy resolution [47]. This new experiment claimed the existence of two excited levels where the previous experiment found one. The excited state at $E_x = 10950$ keV was resolved into two states: $E_x = (10808 \pm 20)$ keV, $S_\alpha = 1.9 \cdot 10^{-2}$ and $E_x = (10953 \pm 25)$ keV, $S_\alpha = 2.8 \cdot 10^{-3}$. Thus the upper limit for the ^{22}Ne(α,γ)^{26}Mg reaction rate was recalculated using $J^\pi = 0^+$ and 5^- for the $E_x = 10808$ keV level and the $E_x = 10953$ keV level respectively. To calculate the lower limit the spin and parity value of $J^\pi = 4^+$ was assigned to the lower excited state and the value $J^\pi = 7^-$ to the higher energy level.
Two years later a nuclear resonance fluorescence experiment was performed to determine the energy and quantum numbers of excited states in ^{26}Mg [43]. The observed intensity pattern in the ^{26}Mg(γ,γ')^{26}Mg reaction was investigated in order to obtain unambiguous spin and parity values for the excited states in ^{26}Mg. A $J^\pi = 1^-$ was attributed to the $E_x = 10949$ keV excited level. The explanation proposed for the disagreement with the previous studies was the presence of a doublet at the energy of the excited level of interest.
The results from the photo-excitation study on ^{26}Mg was adopted both in a new reaction rate compilation, [44] and in a new study, which was devoted to calculate a new reaction rate for investigating s-process in AGB stars [48]. The former assigned to the 395 keV resonance strength an upper limit of $3.6 \cdot 10^{-9}$ eV without entering in further details. The latter computed an upper limit of $8.7 \cdot 10^{-15}$ eV for the same resonance using the S_α found in [47] normalized to the $E_\alpha = 1434$ keV resonance, instead to the $E_\alpha = 831$ keV resonance as in [46]. Indeed scaling the S_α to the 831

keV resonance was shown to lead to biased results for the levels widths in disagreement with the predictions. Following the criticism by [48] and using the results in [46] it was obtained a new corrected result for the 395 keV resonance strength $\omega\gamma = 4.7 \cdot 10^{-13}$ eV, second row of table 2.1.
In 2013 a new reaction rate compilation was published [49], which took into account both the previous more recent works [44,48] and improved their methods to calculate the reaction rate. In this case the upper limit for the 395 keV resonance strength is the same as in [44] but for the rest of the analysis it follows what found in [48].
From the description above is evident that a direct measurement, even if it results in an upper limit for the 395 keV resonance strength, would greatly clarify the contribution of this resonance to the total reaction rate. This is even more evident looking at fig. 2.2, here the reaction rate ratio is plotted as a function of the temperature. The reaction rate ratio is strongly affected by the uncertainty of $E_\alpha = 395$ keV resonance, in particular for $0.25 \leq T \leq 0.5$ which are of interest for the s-process in low-mass AGB stars and in massive stars. NACRE error bars of the reaction rate ratio lay between a factor 10 to a factor 1000 the adopted value for temperature corresponding to the He burning. NACRE error bars are even larger for lower temperatures, at which the ^{22}Ne(α,γ)^{26}Mg reaction rate dominates. The uncertainty of Longland reaction rate ratio is smaller than NACRE, it is a factor 1.3 - 1.6 the adopted values at He burning temperatures. In addition the ratio proposed by Longland makes the ^{22}Ne(α,γ)^{26}Mg negligible at He burning temperatures. Indeed if one assumes the reaction rates adopted in [48] the neutron production is effective for all the temperature range of interest for He-burning, even using the lower limit for the reaction rate ratio. In the case of NACRE the huge uncertainty of the ratio makes everything possible, for example the neutron production is suppressed during He burning phases completely if one assumes the lower limit. More interestingly if the highest value attributed to the 395 keV resonance strength is taken into account [44], then the neutron production is suppressed at $T < 0.4$ GK.

Reference	Lower Limit [eV]	$\omega\gamma$ [eV]	Upper Limit [eV]
Giesen et al. 1993 [46]	$1.4 \cdot 10^{-14}$	$1.7 \cdot 10^{-13}$	$1.6 \cdot 10^{-12}$
Giesen et al. corrected	-	$4.7 \cdot 10^{-13}$	-
NACRE 1999 [42]	-	$1.4 \cdot 10^{-13}$	$1.3 \cdot 10^{-12}$
Iliadis et al. 2010 [44]	-	-	$3.6 \cdot 10^{-9}$
Longland et al. 2012 [48]	-	-	$8.7 \cdot 10^{-15}$
STARLIB 2013 [49]	-	-	$3.6 \cdot 10^{-9}$

Table 2.1: Values for the strength of $E_\alpha = 395$ keV resonance reported in literature.

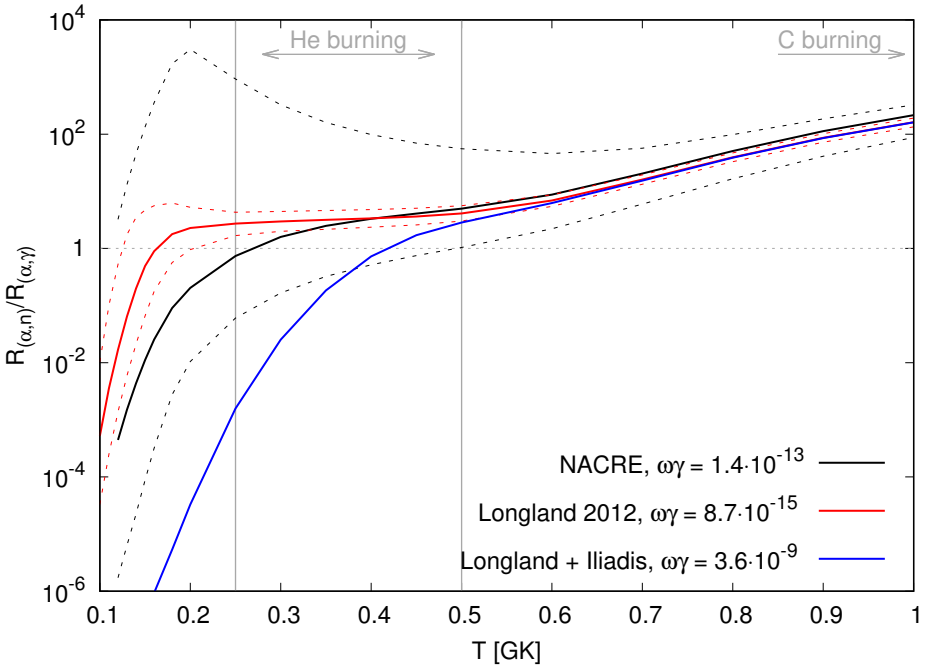

Figure 2.2: Ratio of reaction rates of the $^{22}\mathrm{Ne}+\alpha$ reactions. For scenarios with a ratio much below 1, the s-process neutron source is effectively closed down.

2.2 Experimental Setup

The high intensity beam provided by the LUNA400kV accelerator can be switched between two different beamlines: the gas target and the solid target. The current measurement was performed exploiting the gas target beamline combined with an high efficiency detection system. The high intensity He^+ beam was delivered to a devoted scattering chamber through three differential pumping stages. At the entrance of the scattering chamber no window were installed in order to prevent the beam energy loss and straggling as well as the possible beam induced reactions taking place in the entrance foil. The cylinder chamber was partially occupied by the calorimeter on which the beam stopped. The calorimeter was used to measure the beam intensity run by run. Both the scattering chamber and the calorimeter were located inside the borehole of the detector which consists of six optically indipendent BGO crystals. The setup used for the study of the $^{22}\mathrm{Ne}(\alpha,\gamma)^{26}\mathrm{Mg}$ reaction was the same employed for the second campaign on the $^{22}\mathrm{Ne}(\mathrm{p},\gamma)^{23}\mathrm{Na}$ reaction [50], to which I took part as it was my master degree thesis subject [51]. The setup was characterized during the study of the $^{22}\mathrm{Ne}(\mathrm{p},\gamma)^{23}\mathrm{Na}$ reaction and it is described in the next sections.

2.2.1 The Gas Target System

The use of the gas target is advantageous compared to solid target for many reasons. As a matter of fact a gas target does not deteriorate because of intense beam irradiation, thus it is stable for long periods. Then gas target can achieve very high isotopical purity especially in case of noble gases, which helps in reducing the possible beam induced background. On the other hand it requires complex and expensive pumping systems as well as a full control and knowledge of density profiles and detection efficiency along the beam path. The details of the LUNA gas target beamline are provided in the following sections.

Pumping System and Recirculation Mode

The α-beam from the LUNA400kV accelerator is delivered to a differential pumped windowless gas target system, which consists of three pumping stages, namely the third, the second and the first pumping stages going from the accelerator to the target chamber, see fig. 2.3. A LabVIEW software and a NI FieldPoint based system are used for the slow control of the gas target. The pressures inside the pumping stages are monitored and logged, as well as the pressure inside the buffer and at the purifier entrance. The software allows to open and close the remotely controlled valves inside the accelerator room and monitor the status of the pumps. The three pumping stages and the target chamber are connected by long apertures with different dimensions:

- Aperture AP3, between the third and the second stage, $l = 80$ mm, diameter $= 25$ mm;
- Aperture AP2, between the second and the first stage, $l = 80$ mm, diameter $= 15$ mm;
- Aperture AP1, between the first stage and the target chamber, $l = 40$ mm, diameter $= 7$ mm;

The apertures have the additional purpose of collimating the beam thus they are water cooled. The impedance of the apertures is the optimal one in order to have a pressure in the mbar range inside the target chamber. The evacuation proceeds in the opposite direction than the beam, the gas is flushed out from the target chamber through the pumping stages. Following the gas flow:

- In the first stage the most of the gas ($\geq$ 90%) is removed thanks to a large volume Leybold RUVAC WS 2001 roots pump (2050 m^3/h). The typical pressure level reached here is of the order of 10^{-3} mbar.
- The second stage is connected to three Leybold turbo molecular-pumps: two TMP1000 pumps on the side (TP2L, TP2R), and one higher capacity TMP1500

pump in the center (TP2M) (3600 m^3/h). Pressures of the order of 10^{-6} mbar are usually obtained in this stage.

- The residual gas is evacuated in the third stage by a Leybold TURBOVAC 361 pump (1250 m^3/h). The pressure reached here is of the order of 10^{-7} mbar

All the pumps are sustained by a Leybold RUVAC WS 501 roots pump (505 m^3/h). A remotely controlled valve, V1 in fig. 2.3, connects the roots pump to an additional ECODRY pump (48 m^3/h) through which the gas is finally delivered to the laboratory exhaust pipeline.
In order to study the $^{22}Ne(\alpha,\gamma)^{26}Mg$ a 99.999% chemically pure and 99.9% isotopically enriched ^{22}Ne gas was used. Because of the high price of the target gas the pumping system works also in recirculation mode. The gas from the RUVAC WS 501 pump is collected by an Alcatel ACP28 dry vacuum pump (27 m^3/h) into a 1 L stainless steel buffer. Before reaching the buffer the gas passes through a Monotorr PS4-MT3-R-2 with a PS4-C3-R-2 heated getter, designed to remove hydrocarbons, oxygen and nitrogen from noble gases. Finally the purified gas is redirected from the buffer to the target chamber through the inlet valves, namely VBuffer and VT in fig. 2.3.
The buffer is inserted between the purifier and the target chamber to store the gas, for example if a venting procedure is needed. Indeed, in this case nitrogen gas is used to vent the entire system. The nitrogen flows from a bottle outside LUNA box into the gas target system thanks to a devoted pipeline. The ^{22}Ne gas was kept inside the buffer also during the beam induced background measurements and the efficiency measurements at high energy. In the former case Ar gas was used while N_2 gas was used to study efficiency at high energies Both the gases flowed from a bottle outside LUNA box into the gas target system thanks to a devoted pipeline that can be open by the VHe4 valve in fig. 2.3.
After several runs the gas can be deteriorated, for example because of contaminants, as nitrogen isotopes, introduced by leaks in the setup. In order to monitor the target composition a MKS-RGA mass spectrometer was mounted between the first and the second pumping stages. As a matter of fact the most of the gas is flushed to the purifier through these two pumping stages. The mass spectrometer was controlled by the PPT430 software which allowed to display the logged data in two different modes: the ANALOG and the BAR mode. The ANALOG mode provided a scan of the selected mass region in steps of 0.1 amu. The BAR mode provided a histogram in the selected mass range where each bin corresponds to 1 amu. Both modes were used in order to monitor the status of the target gas and to estimate the possible concentration of contaminants. In addition to this, the pressure of the buffer was checked periodically. When both an increase of the buffer pressure and an increase of the concentration of contaminants were observed then the gas target system was switched from recirculation mode to evacuation mode. The exhausted target gas

was flushed away and thanks to the complex valves system the components of the gas target beamline were cleaned accurately. Then new fresh ^{22}Ne was injected into the empty buffer through a devoted pipeline connected to the ^{22}Ne bottle inside the LUNA box. When a pressure of about 800 mbar was reached inside the buffer the VHe3 in fig. 2.3 was closed as well as the ^{22}Ne bottle. The fresh target gas stayed inside the buffer while the pumping system was switched to recirculation mode again. Then the new ^{22}Ne gas was injected inside the scattering chamber by opening the VT valve, see fig. 2.3.

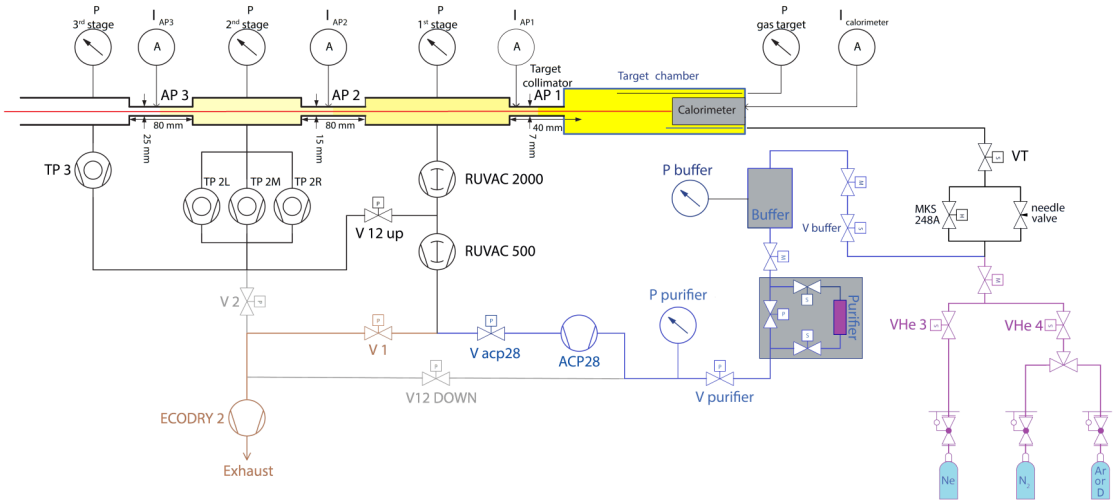

Figure 2.3: Differential pumping system scheme. The beam comes from the accelerator on the left, passes through the apertures AP3, AP2 and AP1, enters the target chamber and stops on the calorimeter. The blue path is the gas path in recirculation mode. The brown is the gas path to exhaust pipeline.

Target Chamber

The target chamber consists of a stainless steel cylinder of 54 mm of diameter and 475 mm of length, and it was designed to fit inside the borehole of the detector as well as the connected tubes and the calorimeter. The reaction volume is only 108 mm long, the rest of the target chamber is occupied by the calorimeter, see next section.

The chamber was provided with two copper tubes, see fig. 2.4, the one ended in the middle of the scattering chamber is the gas inlet, the other, was connected to a MKS baratron type 626 pressure gauge. This gauge, together with its controller and the MKS 248A valve, provided the feedback to keep the chamber pressure stable.

The scattering chamber is insulated from the rest of the setup as well as the aperture AP1. Thus both the empty target chamber and the last collimator (following beam direction) measured independently the beam current helping to optimize the beam transmission and focus. During the focusing procedure, since the beam impinging on the calorimeter liberates a large number of secondary electrons which compromise the charge collection, the chamber was equipped with a secondary electron suppression electrode. This thin, ring shaped electrode was positioned just after the target collimator and a negative potential of typically -100 V was applied to it.

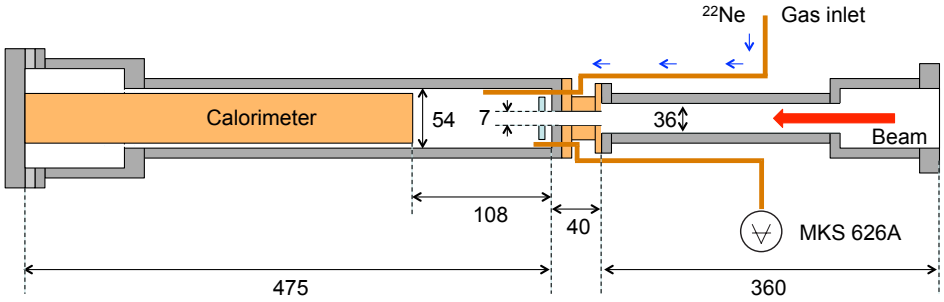

Figure 2.4: Target chamber design with its dimensions in mm (beam enters from the right)

Calorimeter

When the gas was inside the chamber any direct current reading is useless, because of the interaction of the beam with the target and the beam stop. Several secondary electrons can be emitted as well as many beam protons could be neutralized. Therefore an alternative method was required to measure the beam intensity, for this reason a calorimeter was inserted inside the chamber to monitor the beam intensity, see fig. 2.4.
The calorimeter consisted of three parts, see fig. 2.5: the hot side, the resistors and the cold side. A chiller provided the circulation of a refrigerating liquid, at T = -5 C°, which kept the cold side at a temperature of about (7 ± 0.1)°C. The hot side was kept at the constant temperature of (70 ± 0.2)° by eight heating resistors. Four platinum resistors Pt100 were located for the temperature measurement as following: one on the cold side and three on the hot side. Indeed the Pt100 resistance changes with temperature allowing to the measurement of the temperature from its resistance values. The platinum resistors were chosen because of their linear resistance-temperature relationship on wide range of temperature.

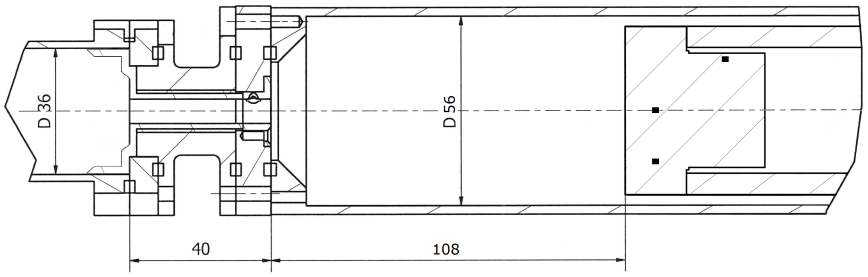

Figure 2.5: Cross section of the interaction chamber. The beam comes from the connecting tube on the left, passes through the AP1 collimator and enters the interaction chamber. The collimator defines the target region, causing the quick drop in the gas density towards the pumping stages on the left. After crossing the chamber, the beam impinges on the beam stop (i.e. the calorimeter hot side). The small black rectangles (right side) represent the temperature detectors installed in the beam stop.

When the beam deposited its energy on the calorimeter it heated up the hot side. Consequently the temperature sensor of the Pt100 regulated the power supply of the resistors in order to keep the temperature constant. From the difference in the power supply required to keep the hot side at a constant temperature without, W_0, and with the beam, W_{run}, it was possible to evaluate the beam intensity:

$$I = \frac{W_0 - W_{run}}{E_\alpha - \Delta E}\, q\,, \tag{2.1}$$

where $(W_0 - W_{run})$ is the power provided by the beam, W_{beam}. E_α is the energy of the beam entering the scattering chamber. ΔE is the beam energy loss inside the target along the path to the calorimeter.
The calorimetric power was calculated by measuring the heating resistors voltage (V) and current (I), according to the relation $\mathrm{W} = \mathrm{V} \cdot \mathrm{I}$. In order to decouple from the power circuit both the measurements two different dividers are used. The current divider was a LEM LAH 25-NP current transducer completely decoupled from the power circuit. A passive resistive series with high resistance ($3 \times 300\,\Omega$) was the divider used to get the voltage output. The high resistance of the voltage divider makes any possible influence on the power circuit negligible. The dividers outputs are measured by a NI cRIO 9207 module and logged every second by the LabVIEW control software.
The calibration of the calorimeter was performed in vacuum for two temperatures of the cooling liquid ($\mathrm{T} = -5°$ and $\mathrm{T} = -20°$). The current measured by the calorimeter was compared with the one measured by the scattering chamber, which works as a Faraday Cup in vacuum. The beam current was read by an ORTEC 439 digital current integrator and an ORTEC 994 counter. The measurement was performed

at different beam energies in order to obtained a calibration function, see fig. 2.6. The final calibration obtained is [50]:

$$W_{elec} = (0.936 \pm 0.002) \cdot W_{calo} + (-0.67 \pm 0.13)\, Watt\,. \tag{2.2}$$

In order to estimate the uncertainty of the calorimetric current measurement some tests and different factors were taken into account: the calorimeter uncertainties, the error on the electrical reading and the calibration. The final estimated uncertainty of the beam intensity was 1.5% [50].

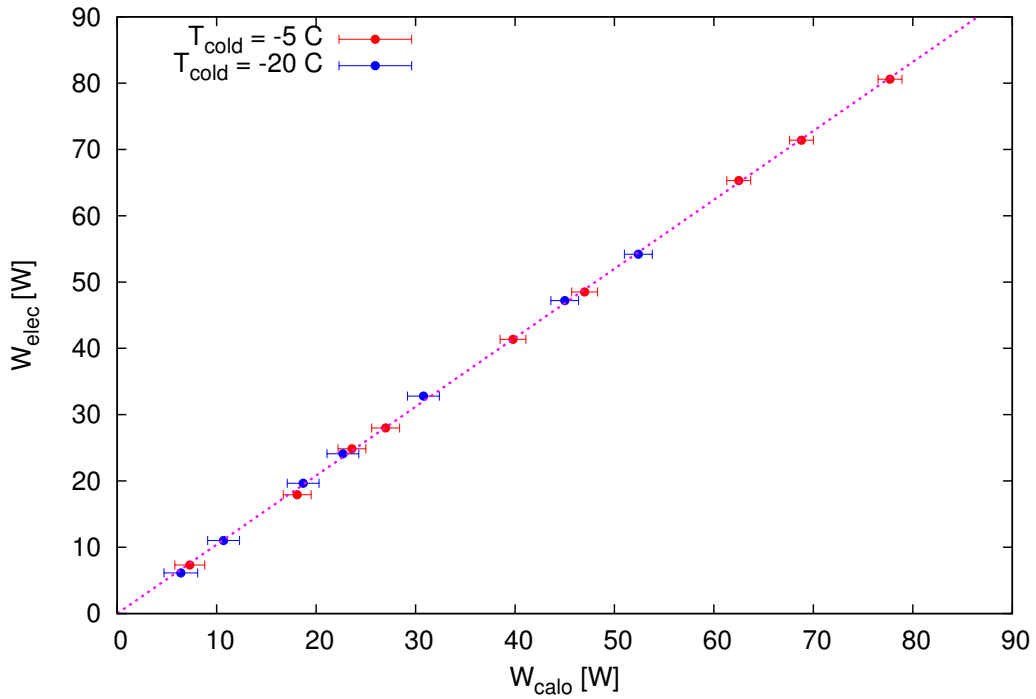

Figure 2.6: Calibration of the calorimeter. On the x-axis the beam power measured with the calorimeter and on the y-axis the beam power as read by the scattering chamber. The calibration was performed at two different temperature of the cooling liquid, here referred as T_{cold}.

2.2.2 Target Density Profile

When the beam entered into the target chamber, due to collision with gas atoms of the target, it lost energy. The total beam energy loss along the path to the beam stop depends on the target density:

$$\Delta E = \int_{beampath} \epsilon\, \rho(z)\, dz\,, \tag{2.3}$$

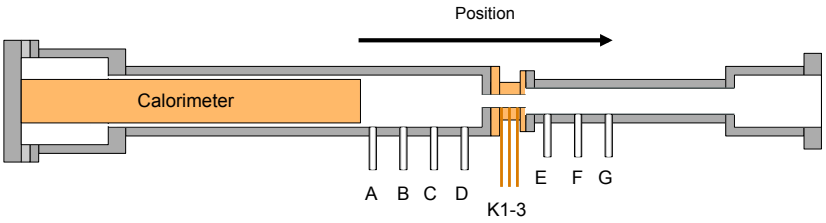

(a)

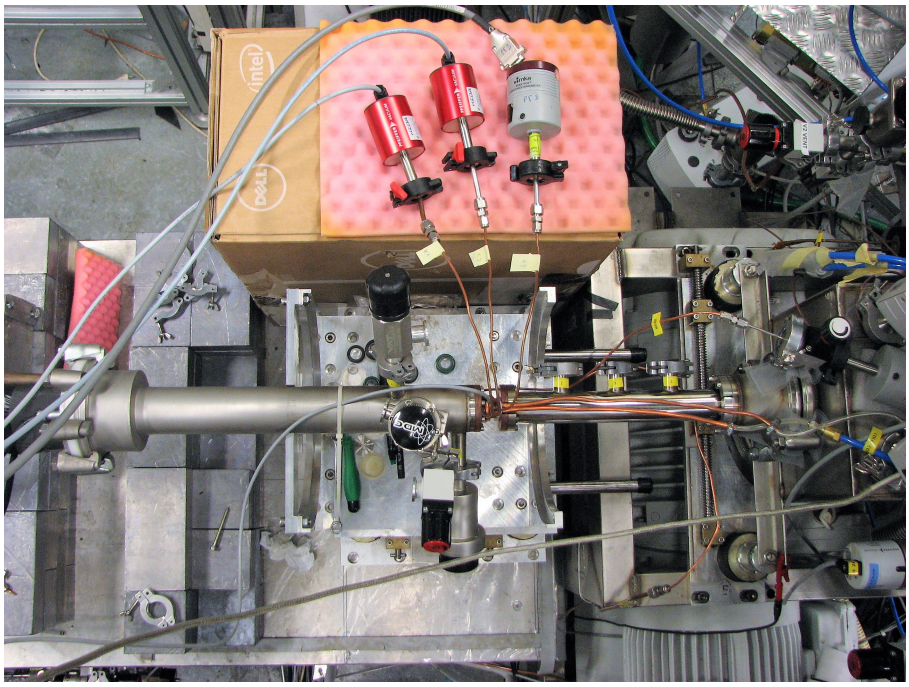

(b)

Figure 2.7: a): A draw of the *flute* chamber used for the pressure and the temperature profile measurement. b): The *flute* chamber seen from the top. The different tools used to measure the pressure and the temperature are visible.

where ϵ is the stopping powere defined as the energy loss per unit length and density $\frac{dE_p}{d\rho(z)}$, which can be taken from SRIM2013 [52] and it represents the energy loss of a specific beam per unit path length in a specific target. The energy loss is a fundamental quantity in beam intensity calculation, see eq. (2.1), thus a precise knowledge of the gas density along the beam path, $\rho(z)$, is required.
According to the ideal gas law, the density can be derived directly from the pressure and temperature profiles:

$$\rho(z) = \frac{P(z)}{kT(z)}\,. \tag{2.4}$$

In order to obtain the pressure and the temperature profiles inside the target a modified version of the original chamber was used, see fig. 2.7. The so called *flute* chamber was identical to the current scattering chamber except for seven additional KF25 flanges welded on its side. In particular four of these flanges, from A to D in fig. 2.7, were on the chamber side while the other three, from E to G, were on the interconnection tube between the chamber and first pumping stage of the gas target system. In addition 3 holes, namely K1, K2 and K3, were drilled on the AP1 collimator in order to investigate the pressure drop inside it. While for the measurement of the pressure in the chamber and in the interconnection tube the sensor were mounted directly on the KF25 flanges, in the case of the collimator it was required to mount 30 cm long copper tubes on each hole, see fig. 2.7. The other end of these copper pipes were equipped with a KF25 flange pipes.
The pressure measurement were performed with 4 pressure sensors: two MKS Baratron 626A type absolute pressure transducers with 10 torr (13.3 mbar) range (0.25% accuracy), and two Pfeiffer CMR 363 ceramic capacitive gauges with 10 mbar range (0.20% accuracy). The Baratrons were used in combination with the MKS Valve Controller unit, while the Pfeiffer gauges were connected to a Pfeiffer MaxiGauge controller unit. One of the MKS baratrons were positioned in the same configuration as during the current experiment and this was used as reference for the pressure during the pressure profile investigation. To perform the calibration the three gauges were connected with a cross connector to a side tube of the interaction chamber and measurements were taken from 0 up to 5 mbar in steps of 0.5 mbar. A slope-intercept calibration curve was used for each pressure gauge. The linearity of the gauges was proved, although a difference of about 4% was found between the slope of one of the CMR 363 and the slope of the reference gauge.
The pressure profile was studied in 0.5 mbar steps from a target pressure of 0.5 mbar to 5 mbar using the ^{22}Ne gas. The results are shown in fig. 2.8.
The agreement between the four pressures measured inside the chamber and the reference pressure was better than 0.5%. Inside the chamber the pressure profile is flat, while inside the collimator the pressure drops of 1 order of magnitude. The decreasing of the pressure is smoother inside the interconnection tube. The overall uncertainty of the pressure profile was estimated to be 1% [50].
Because of the presence of the calorimeter the temperature inside the chamber was expected to not be flat as it was found for the pressure. The temperature was measured only inside the chamber mounting on the KF25 modified blind flanges the already mentioned Pt100. The resistance of the Pt100 sensors was measured by two NI 9217 modules. The same modules also converted the measured resistance (based on their inner calibration) into temperature readings for the LabView system. The

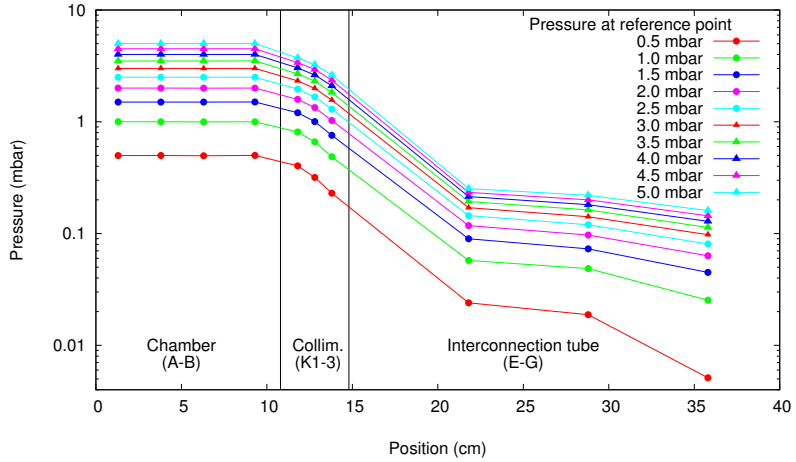

Figure 2.8: Pressure profile in the gas target. The lines are just to guide the eye.

measured temperature gradient from the position "Calo", which is located close to the calorimeter, to the target chamber entrance, position "K", is plotted in fig. 2.9. The temperature inside the connecting tube was supposed to be the same as the room temperature, which was logged by a Pt100 located in the accelerator room. Two more temperature measurements were available: one on the collimator, measured by a resistive temperature detector (RTD) located outside it, and one on the calorimeter hot side, kept constantly at 70°.
Combining the pressure profile, fig. 2.8, and the temperature profile, fig. 2.9, according to eq. 2.4 the density profile of the target was obtained, fig. 2.10. Because the experiment was performed with the ^{22}Ne at a pressure of 1 mbar the density profile was derived for only this value of the pressure.
The density increases with decreasing of the temperature from the calorimeter to the collimator, inside which the density drops and then it decreases slowly in the interconnection tube.
The trend observed in the collimator, points K_1, K_2 and K_3, was in good agreement with the one extrapolated from the density data in the chamber and in the interconnection tube.
Taking into account the uncertainties from the pressure and temperature measurements and the extrapolation in the collimator, a total uncertainty of 1.3% was found for the integrated gas thickness.
It is now possible to define the effective length:

$$l_{eff} = \frac{1}{\rho_c} \int_{z_0}^{z_1} \rho(z) dz \,, \tag{2.5}$$

where the integral is from the first stage to the calorimeter and ρ_c is the reference density in the middle of the chamber. The effective length calculated for the setup

described at p = 1 mbar is l_{eff} = 13.92 ± 0.5 cm. The 0.5 cm uncertainty is estimated considering alternative extrapolated density profiles from 10.8 cm to 14.8 cm positions in fig. 2.10 (inside the collimator). The chamber contributes 10.4 cm to l_{eff}, the collimator 2.4 cm and the interconnection tube 1 cm. This means that the beam had to travel a path of 8.6 cm to reach the center of the target.
The effective length is useful to estimate the energy loss of the beam along the path through the beam stop at a reference target density, ρ_{ref}:

$$\Delta E = \rho_{ref}\, \epsilon\, l_{eff}\,, \tag{2.6}$$

where ϵ is the already mentioned stopping power.

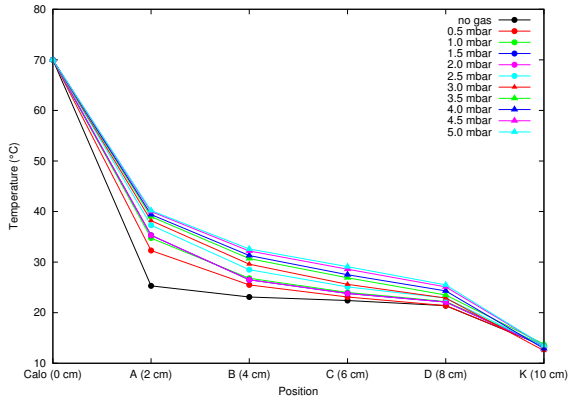

Figure 2.9: Temperature profile in the target chamber for several different target pressures. The lines are just to guide the eye.

Beam Heating Effect

The energy loss, important for the beam intensity estimation, is a function of the target $\rho(z)$, see eq. 3.28. On the other hand when the beam loses its energy because of the interactions with the target atoms these lead to a local heating of the gas and thus to a local density decrease. This effect is the beam heating effect and it makes necessary a correction to the density profile. The higher the beam power, the larger the correction is.
The beam heating correction in neon was studied during the first experimental phase on the ^{22}Ne(p,γ)^{23}Na reaction at LUNA, exploiting the resonance scan technique [24]. The target gas used for the beam heating study was natural neon, 90.48% ^{20}Ne, 0.27% ^{21}Ne and 9.25% ^{22}Ne. The resonance considered was the strong and narrow resonance ($\omega\gamma$ = 83 meV, Γ = 3 eV) at proton beam energy E_{res}^{lab} = 271.6 kev in the ^{21}Ne(p,γ)^{22}Na reaction. A collimated NaI detector was placed perpendicularly to the beam. The maximum yield is observed when the resonance is populated in

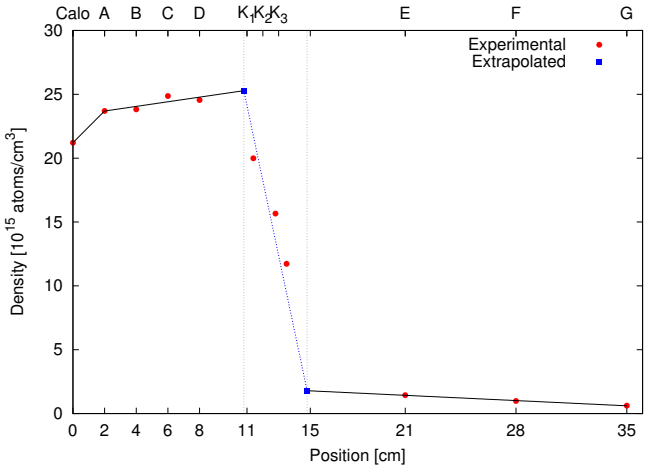

Figure 2.10: Gas density profile along the beam axis (beam from the right). The black line represents the adopted density profile.

front of the detector, thus the experimental energy loss for that target length can be calculated as:

$$\Delta E = E_p^{init} - E_{res}^{lab} \tag{2.7}$$

The energy loss was evaluated for several gas pressure and beam current values in two different position of the NaI detector. Then the energy loss $\Delta E_p^{exp}(p_T, I)$ were extrapolated to zero current and finally the reduction factor was calculated:

$$\frac{\rho}{\rho_0} = \frac{\Delta E_p^{exp}(p_T, I)}{\Delta E_p^{exp}(p_T, 0)} . \tag{2.8}$$

It is known that the beam heating effect is proportional to the specific power dissipation (power dissipated per unit length) of the beam in the target gas [53]:

$$\frac{dW}{dx} = \frac{dE}{d(\rho \cdot x)} \rho I , \tag{2.9}$$

therefore the reduction factor can be write as:

$$\frac{\rho}{\rho_0} = 1 - C\frac{dW}{dx} , \tag{2.10}$$

where the coefficient C was found to be $(0.44 \pm 0.05) \times 10^{-3}$ cm/mW.
The results found in the first campaign on ^{22}Ne(p,γ)^{23}Na could not be directly adopted for the current setup for two main differences: the target chamber geometry was different and the α-beam was used for the current study. Both these differences were took into account applying analytic corrections.

The ΔT caused by the beam heating depends on dimension of the chamber as following [54]:

$$\Delta T = \frac{H}{2\pi K} ln\Big(\frac{b}{a}\Big), \tag{2.11}$$

where H is the heat flow, K is the thermal conductivity of the gas, b is the inner and the outer radius of the target chamber and a is the beam radius. During the first phase of the study of the ^{22}Ne(p,γ)^{23}Na reaction the beam dimension was defined by the same 7 mm aperture as the current one. The target chamber was rectangular with an equivalent inner radius of 120 mm. Inserting the previous setup data together with the current ones into eq. (2.11) it was found:

$$C_{current} = C_{previous} \frac{ln(b_{current}/a)}{ln(b_{previous}/a)} = 0.32 cm/W \tag{2.12}$$

In order to check the result a second method was used to derive the reduction factor for the current setup. During the ^{14}N(p,γ)^{15}O LUNA experimental campaign [23] the current target chamber was used. The beam heating coefficient C found was 0.54×10^{-3} cm/mW, which must be converted to the ^{22}Ne case taking into account the different thermal conductivity of the two gases. The beam heating for proton beam in neon can be derived from the one in nitrogen as follows:

$$C_{Ne} = C_{N_2} \frac{K_{N_2}}{K_{Ne}} = 0.29 \frac{cm}{W}. \tag{2.13}$$

Since both methods yield comparable results the accepted beam heating coefficient for the current setup with proton beam was (0.31 ± 0.09) cm/mW [50].
In order to correct the reported value for the α-beam one have to take into account that the dissipated power depend on the stopping power of the ion beam in the target [53], see eq. 2.9. Thus the correction to be applied is simply the ratio between the stopping powers of the α-beam and the proton beam:

$$C_\alpha = C_p \frac{(dE/dx)_\alpha}{(dE/dx)_p} = 0.84 \frac{cm}{W}. \tag{2.14}$$

With this assumption, the typical beam heating correction was of about 15%. Due to the fact that the determination of these value relies on measurements either in different geometry or in different target gas or with different ion beam, as a conservative assumption 50% uncertainty was assigned.

2.2.3 Detector and DAQ

The low values reported in literature for the 395 keV resonance strength make the high efficiency setup used for the study of the ^{22}Ne(p,γ)^{23}Na reaction suitable also for the study of the ^{22}Ne(α, γ)^{26}Mg reaction. In the next sections the details on the detector and on data acquisition (DAQ) are described.

BGO Detector

A large segmented bismuth germanate scintillator ($Bi_4Ge_3O_{12}$ hereinafter referred to as BGO) by Scionix was used to detect gamma rays from the $^{22}Ne(\alpha,\gamma)^{26}Mg$ reaction [55]. Thanks to bismuth high density (ρ = 7.13 g/cm^3) and high atomic number (Z = 83) the BGO has the highest detection efficiency among the scintillators. On the other hand its high refractive index (n = 2.15) and the low light yield are the main causes of the BGO low resolution. Moreover the high sensitivity to temperature of the light collection makes the energy calibration of the BGO unstable. At room temperature of 20°C the light yield decreases by 1% with every 1°C increase of the temperature [56]. A change in the energy calibration may cause a worsening of the resolution during long runs (1 day long or more).
The detector consists of six optically separated segments, 28 cm long and 7 cm thick, arranged in hexagonal configuration in order to be housed inside a steel casing, see fig. 2.11a. The case is provided with a coaxial hole, 6 cm of diameter, where the target chamber with the tubes and the calorimeter was located, see fig. 2.11. This configuration of the detector results in a covered solid angle of about 4π. The BGO case was on a frame which can move along the beam line if necessary. Each crystal is read out by one photomultiplier (PMT) on the calorimeter side while on the pumping stages side six reflective caps were installed as shown in fig. 2.11b.

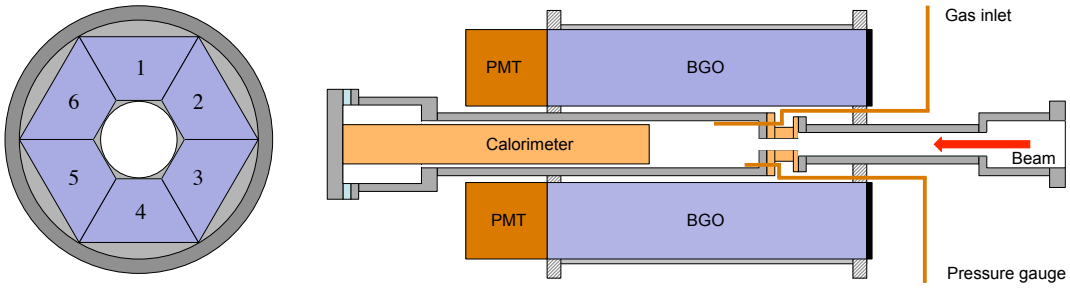

(a) (b)

Figure 2.11: a): Cross section of the BGO detector. b): BGO detector with target chamber

DAQ

The Data Acquisition electronics is presented in fig. 2.12. Each crystal had a devoted digital acquisition chain and independent power supply. The high voltage power supply was provided by a CAEN V6533P HVPS which was controlled via GeCo2020 software. In order to match the gain of the 6 crystals typical values of

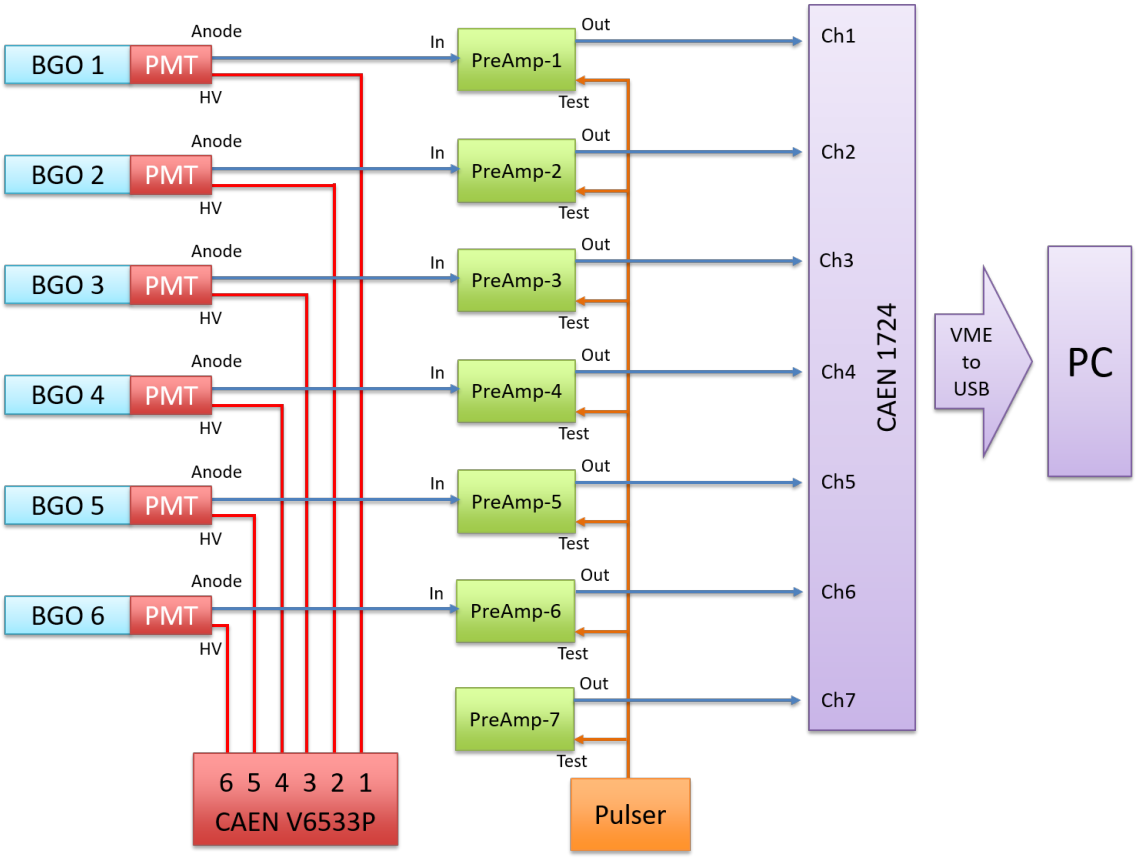

Figure 2.12: DAQ electronics scheme

about 900 V were needed for the PMTs. However differences up to 50 V occurred among the PMTs. The signals from the six anodes were independently amplified by six ORTEC 113 scintillation preamplifiers. A pulse generator was connected to the preamplifiers to check the stability of the electronics. The output from each amplifier was then acquired by a separated channel of a CAEN V1724 (8 channels, 14 bit, 100 MS/s) digitizer. Each channel had independent and tunable parameters for the trapezoid filter used by the CAEN V1724 card to process the signal. The digitizer is connected to the PC through a CAEN VME-USB bridge and it is read out by the MC2 Digital MCA Data Acquisition and Analysis Software. The MC2 software allows to check and save online each channel spectrum. In addition the timestamp and the energy for each event were saved in a binary file.
An homemade software program converted the binary file in ROOT file [57] and built the spectrum for each segment. In addition the program created the addback spectrum, which contains the sum of the coincident signals in two or more crystals. Indeed the BGO detector, thanks to its high efficiency and its solid angle, could

detect multiple radiation emitted in the same nuclear decay. Events laying in a 3.5 μs wide window were considered coincident by the program and their energies are summed and recorded in the addback spectrum. The so called sum peak arises in the addback spectrum at $E_\gamma = Q + E_\alpha^{cm} = E_{\gamma_0} + E_{\gamma_1} + ...E_{\gamma_n}$, where E_{γ_i} are the energies of the gammas in the decay chain. In fig. 2.13 the simple case of the decay radiation by the ^{60}Co is reported. The ^{60}Co decay produces two γ-rays corresponding to the de-excitation of its daughter nuclei, the ^{60}Ni, through the 1332 keV level. The spectrum acquired by only one BGO cristal with the ^{60}Co source positioned in the middle of the scattering chamber is shown in fig. 2.13a. The two peaks corresponding to the primary and the secondary transitions described above are evident. At $E_\gamma \sim 2500$ keV a peak is visible. This is the sum peak and it is visible in the single-crystal spectrum because the probability of coincident acquisition of two γ-ray is not zero for the single crystal. In fig. 2.13b) the addback spectrum for the same configuration is presented. The sum peak arises. The most of the complete decay chains can be reconstructed. The single transitions still visible in the addback spectrum originated by the escape of one of the two γ-rays outside the crystals. Since the timestamp and the energy of each event was recorded, it was possible to recover coincidence information offline. Indeed the single event that contributed to a peak could be recovered gating on a proper energy window in the addback spectrum.

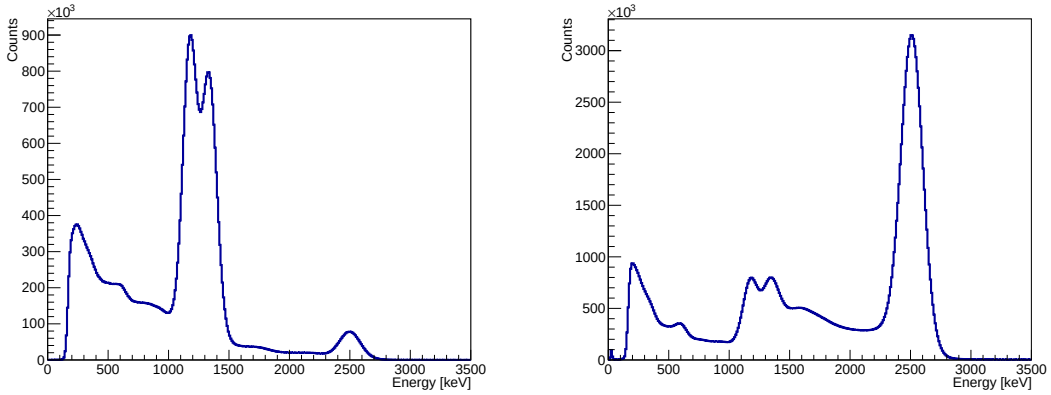

(a) (b)

Figure 2.13: a): Spectrum acquired by a single BGO crystal with the ^{60}Co source inside the scattering chamber. b): The corresponding addback spectrum.

Isotope	Half-life [yr]	Manufacturer	Ref. Activity [kBq]	Ref. Date [dd/mm/yy]
^{7}Be	$0.15 \pm$	MTA-ATOMKI	112.6 ± 2.4	18^{th} April 2014
^{60}Co	$5.27 \pm 3.8E-04$	PTB	9.12 ± 0.04	1^{st} January 2005
^{88}Y	$0.29 \pm 5.8E-05$	Eckert & Ziegler	36.8 ± 0.4	1^{st} April 2014
^{137}Cs	30.08 ± 0.09	PTB	11.30 ± 0.06	1^{st} January 2005

Table 2.2: Properties of the radioactive calibration sources (The given uncertainty on the source activity corresponds to 1σ.)

Detection Efficiency

The BGO efficiency was studied during the second campaign of the ^{22}Ne(p,γ)^{23}Na reaction study combining two methods: an experimental approach and Monte Carlo simulations. The efficiency of the single crystal can be easily studied using standard sources and nuclear reactions, but the addback mode efficiency is more difficult to understand. Indeed an analytic description of the addback efficiency exists [58] but it becomes impractical if the decay of the excited state proceeds via large number of intermediate states or if the branching ratios are not well determined as well as the single crystal efficiency at the proper energy. Therefore Geant3 and Geant4 codes were used to simulate the setup design and to derive the detection efficiency [57,59]. The codes were tested and validated independently on a wide range of energies (from 0.5 MeV up to 7.6 MeV) using the efficiency measurements performed with four pointlike sources (^{7}Be, ^{60}Co, ^{88}Y and ^{137}Cs, see table 2.2 for the sources properties) and exploiting the well known resonance at $E_p = 278\,\mathrm{keV}$ in the ^{14}N(p,γ)^{15}O reaction [60]. The sources were mounted on a special target holder which can move along the beam direction, see fig. 2.14. To minimize the attenuation in the source holder this was shaped in frame-like design and it was made of plastic. The source was kept in place by small pins. The source holder was mounted on an aluminum rod which could slide inside a guide at the end of the target chamber, see fig. 2.14. Because of the source holder geometry it was not possible to measure the efficiency in every position along the beam path.

The measurement with the sources provided informations on the efficiency at low energies (up to $E_\gamma = 3$ MeV), which were useful to fix the geometry. But since the expected signal from the ^{22}Ne(α, γ)^{26}Mg lays at energies around $E_\gamma = 11$ MeV new measurements at higher energies were necessary.

The decay of the well known resonance at $E_p = 278\,\mathrm{keV}$ in the ^{14}N(p,γ)^{15}O reaction proceeds through the excited states plotted in fig. 2.15, then the gammas originated by the decay of the ^{14}N(p,γ)^{15}O resonance can be used to tune the simulation at high energies (up to 7.5 MeV), see fig. 2.16.

The simulation codes were developed and validated independently. They have no

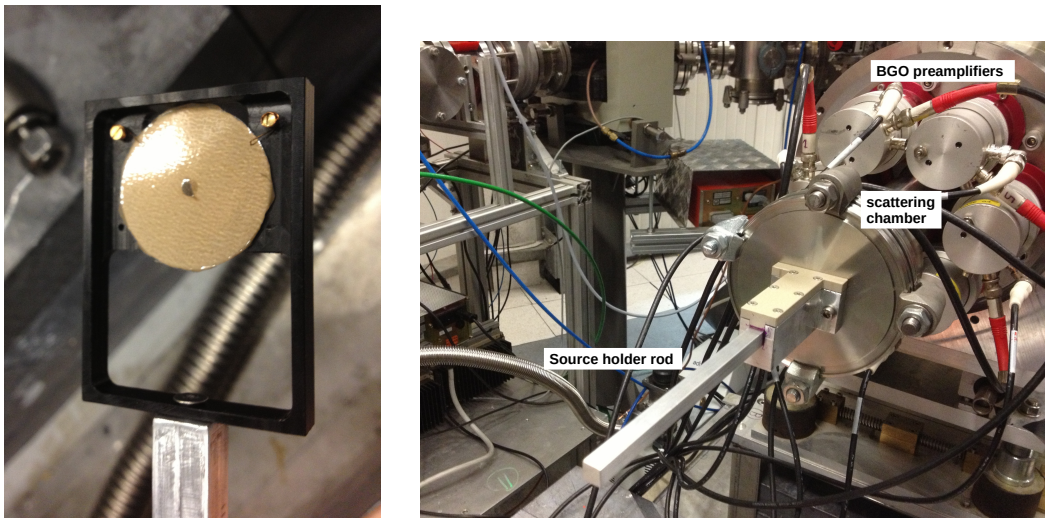

(a) (b)

Figure 2.14: a): Source holder for efficiency measurement. b): Modified end flange and positioning rod for efficiency measurement

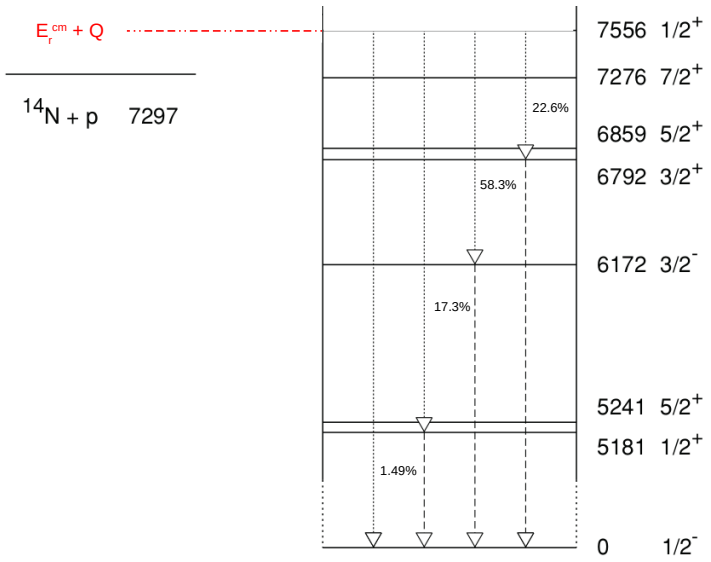

Figure 2.15: ^{15}O levels scheme with transitions occurring at $E_p = 278\,\text{keV}$ resonance. The branching ratios of the transitions are reported too [60].

main differences in the treatment of the decay radiation from the sources. However

the Geant3 code provided a full description of a nuclear reaction taking into account physical effects as the straggling of the beam and the beam heating effect.
The Geant4 code described the nuclear reaction as a radioactive decay, the user can specify the beam energy at the position of the gamma rays emission. The development and validation of the codes were performed by multiple comparison between the experimental spectra and the simulated data. Both single crystal and addback spectra were used to understand how to improved the codes, see fig. 2.16. Once the codes were validated, the simulation of the ^{22}Ne(α,γ)^{26}Mg was performed. The efficiency in the region of interest at the position x was calculated from the simulated spectra as:

$$\eta_{fe}(x) = \frac{N_{ROI}(x)}{N_{init}}, \tag{2.15}$$

where $N_{ROI}(x)$ is the number of counts in the simulated spectrum in the region of interest and N_{init} are the initial simulated events/decays. For the simulation of the 395 keV resonance it was assumed a single transition to the ground state. The efficiency was found to be of the 60% in the ^{22}Ne(α,γ)^{26}Mg region of interest. The uncertainty to the validation of the simulations has been assumed to be 4% [50].

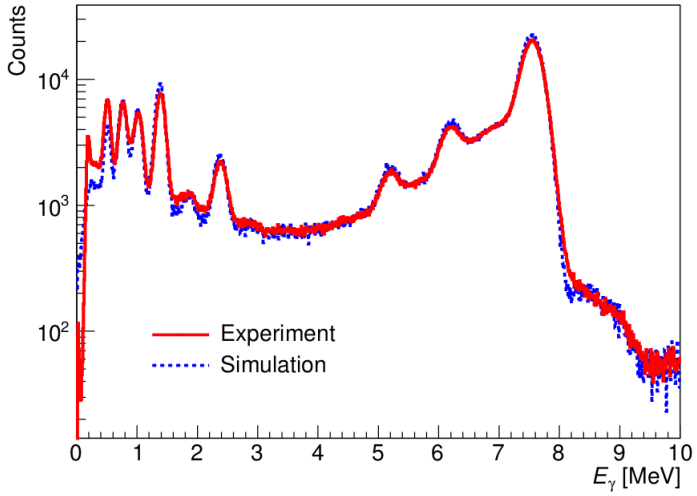

Figure 2.16: The ^{14}N(p,γ)^{15}O addback spectrum at the resonance E$_p$ = 278 keV. Comparison between the experimental spectrum and simulation [50].

2.3 Data Analysis and Results

The measurement time was allocated, following some experimental issues encountered during the experiment, as described in table 2.3.

t_m days	Charge [C]	Target Gas	Target Pressure [mbar]	E_α [keV]	Aim
49	-	-	-	-	Laboratory background
0.5	13.5	Ar	0.468	399.9	Beam induced background
21.2	430	^{22}Ne	1	399.9	395 keV resonance

Table 2.3: Time of measurement (t_m) and collected charge for each experiment task.

Because of the low values of the 395 keV resonance strength and the low counting rate expected it was crucial to estimate precisely the contributions from the laboratory background and from the beam induced background in the region of interest for the current study. The former was widely studied with a 49 days long acquisition which was divided into 4 sets of data. The first spectra were acquired in December (t_m = 25 days), six months before the start of the experiment. Then the other laboratory background spectra were collected immediately before (t_m = 6 days), during (t_m = 1 day) and immediately after (t_m = 16.8 days) the ^{22}Ne(α, γ)^{26}Mg reaction measurement. The spectra for the study of the laboratory background were acquired with the beam off, using the acquisition in the same geometry as during the experiment and both with and without gas in the target chamber.
The beam induced background was studied delivering the 399.9 keV α-beam to 0.468 mbar of Ar gas in the target chamber. The argon gas is expected to be not reactive to the ion beam at this energy. This feature allows to identify contaminants in the target chamber which can be source of background for the experiment. The pressure was calculated as the optimal to have the same beam energy loss as in ^{22}Ne, reproducing the measurement conditions. The beam induced background study was supposed to match the same collected charge as for the investigation of the 395 keV resonance. Because of some experimental issues and delays the data acquired were insufficient for the purpose, see table 2.3.
The study of the 395 keV resonance was performed impinging an high intensity α-beam (I$>$ 200 μA), accelerated up to 399.9 keV, on 1 mbar of enriched ^{22}Ne target gas. The energy of the beam and the pressure of the target gas were chosen in order to have the beam at the resonance energy exactly at the location of the maximum detection efficiency, the middle of the chamber. The data for the study of the ^{22}Ne(α,γ)^{26}Mg reaction, as well as the laboratory and the beam induced background, were acquired in 12 hours long runs because of the instability of the detector energy calibration, see sec. 2.2.3. The total collected charge was $C_{tot} > 400$ C. All the data acquired for the laboratory background and the ^{22}Ne(α,γ)^{26}Mg reaction are plotted as sum of all the corresponding addback spectra in fig. 2.17.
For the ^{22}Ne(α,γ)^{26}Mg the expected gamma-rays have $E_\gamma = Q + E_\alpha^{c.m.} = (10614 + 334)$ keV$= 10950$ keV, a region of interest (R.O.I.) centered at this energy is shown

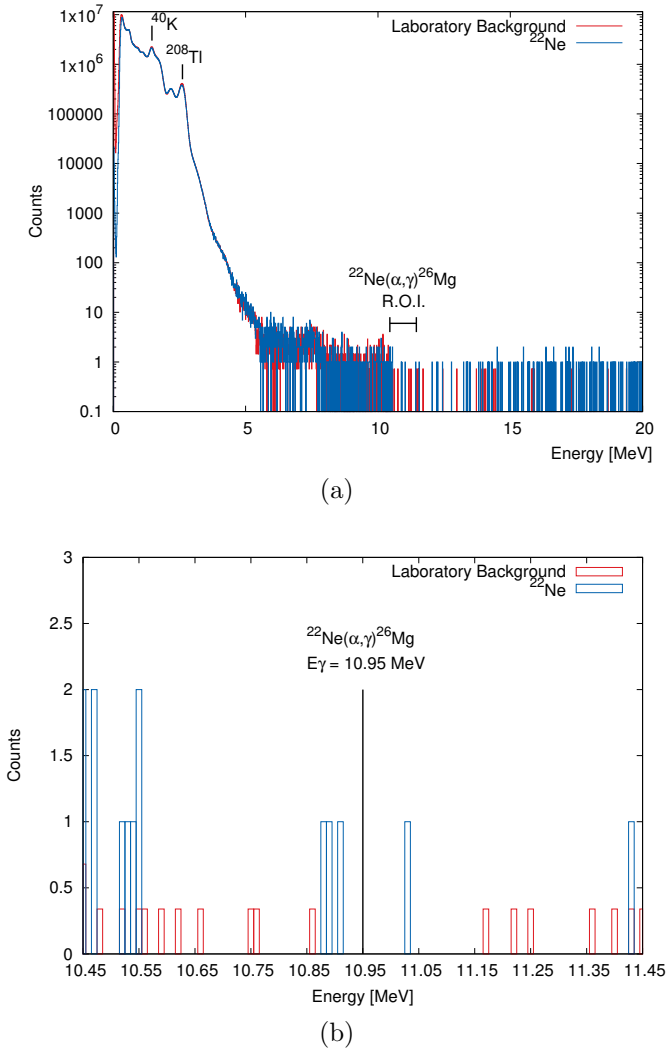

Figure 2.17: a): In red the sum of all the addback spectra acquired to investigate the laboratory background. In blue the same for the study of ^{22}Ne(α,γ)^{26}Mg reaction. The region of interest (R.O.I) for the 395 keV resonance is also reported. b): zoom of the region of interest for the current study of the ^{22}Ne(α, γ)^{26}Mg reaction

in fig. 2.17. Indeed the first step of the analysis was the energy calibration of all the spectra.
Each spectrum was self calibrated, because no reference spectra acquired before or during or after the measurement could be useful. However, in each spectrum the only peaks available for the energy calibration were those of the natural background, in particular the gamma rays from ^{40}K (E_γ = 1461 keV) decay and from ^{208}Tl (E_γ = 2614 keV) decay, see fig. 2.17. Thus the energy calibration could

be fixed only up to E_γ = 2614 keV, quite far from the region of interest for the ^{22}Ne(α,γ)^{26}Mg reaction. In addition it is known that the energy calibration of the BGO deviates from linearity for $E_\gamma > 9$ MeV, that is the current case.
In order to estimate the deviation from the linearity two addback spectra were analyzed which were acquired during the previous experiment performed at LUNA with the BGO. In these two spectra the peak of the resonances of the ^{22}Ne(p,γ)^{23}Na (E_p = 156.2 keV and 189 keV) is evident and it corresponds to $E_\gamma \sim 9$ MeV, see fig. 2.18. At low energies there are the laboratory background peaks while at higher energies there are the two peaks (at $E_\gamma \sim 11$ MeV and $E_\gamma \sim 16$ MeV) from the ^{11}B(p,γ)^{12}C reaction. A linear calibration based on ^{40}K and ^{208}Tl peaks, as the one performed on current experiment data, was applied to the two spectra. The ^{22}Ne(p,γ)^{23}Na peak was shifted of about 60-70 keV from the nominal position, while the peaks at higher energies from the ^{11}B+p reaction were shifted of about 200-400 keV depending on the spectrum, see fig. 2.18 for the run acquired to investigate the 189 keV resonance. Because of this result and the low resolution of the BGO it was decided to use a region of interest of 1000 keV (10450-11450 keV) in order to take into account possible shifts due to the non linearity of the BGO energy calibration and the counts distribution because of the BGO resolution.

Because there were no evident peaks in the identified region of interest, see fig.

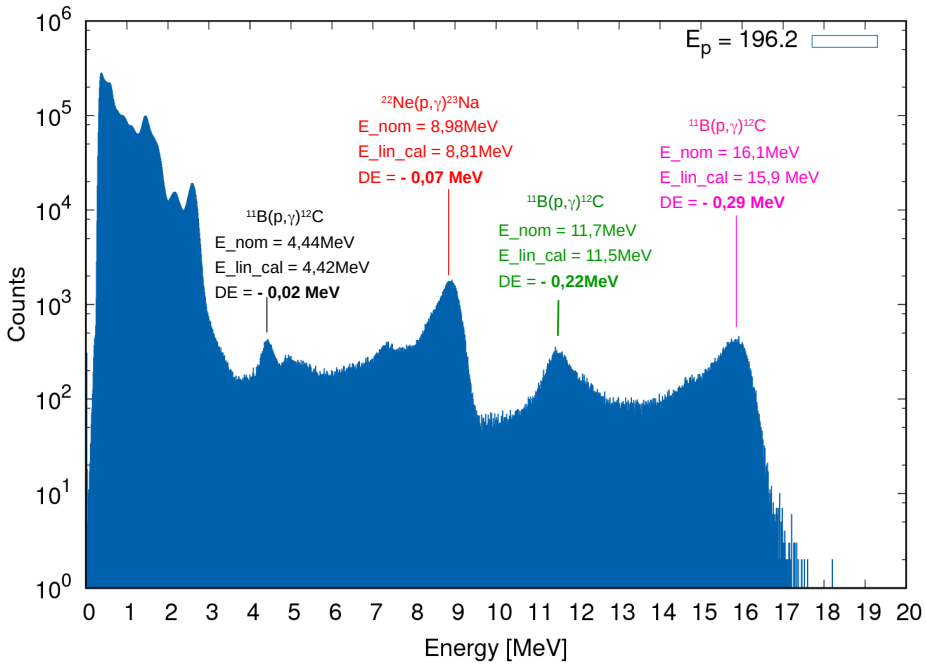

Figure 2.18: Test on linearity of BGO energy calibration.

2.17, the analysis had to proceed through a precise comparison with the laboratory background in order to understand the origin of the counts in the region of interest. It is known that the laboratory background may change during the year because of the different percentage of humidity and water in the atmosphere and in the rock. The laboratory background spectra were acquired, as already described, mainly in winter and during the summer, thus it was necessary to check the stability of the background in order to identify the spectra to be used to perform the comparison with the ^{22}Ne(α,γ) spectra. In particular the analysis was focused on two regions of the spectra: between 6 and 8 MeV, where the thermalized neutron background lays, and on the region of interest of ^{22}Ne(α,γ)^{26}Mg reaction, where the more energetic muons contributes to the laboratory background.
The rate (number of counts per unit of time) was calculate in these regions of interest for the laboratory background spectra acquired in December, then for those acquired in the summer, before and after the measurement. The result are shown in fig. 2.19. Even if the difference between the winter data and the summer acquisition is not significant because of the low statistics collected before and after the measurement, a trend is visible in the plots of fig. 2.19. Thus in order to be conservative it was decide to compare the ^{22}Ne spectra only with the laboratory background data acquired before and after the measurement.

After having summed all the addback spectra for the laboratory background and those for the 395 keV resonance measurement the Net Count (N) was calculated for the region of interest between 10450 and 11450 as following:

$$N = A - c \cdot B, \tag{2.16}$$

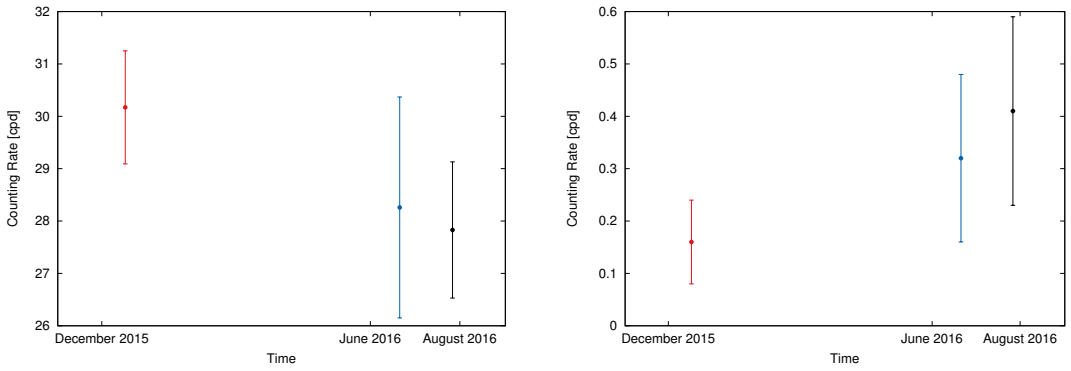

(a) (b)

Figure 2.19: The background was acquired during three different periods of the year. a): The counting rate as counts per day between 6 and 8 MeV in each set of the laboratory background spectra is plotted. b): The counting rate in the region of interest for the ^{22}Ne)α,γ) for each set of the laboratory background spectra.

where A and B were the counts in the region of interest for the ^{22}Ne spectra and for the laboratory background respectively. The latter was corrected for the factor c which was the ratio between the live time of the ^{22}Ne and of the laboratory background spectra.
In order to understand if the Net Count was significant it must be compared with the *critical limit* (L_C) [58]. The L_C is the level above which the net count is significant with a certain degree of confidence. To estimate this level it is supposed that a sample with no radioactivity was measured a large number of times. A series of counts would be obtained for which the mean net count above background was zero but distributed in a Gaussian fashion with a standard deviation, σ_0. A measurement is truly zero if $N < k_\alpha \cdot \sigma_0$ where k_α is selected to provide a predetermined degree of confidence. If $N > k_\alpha \cdot \sigma_0$ the measurement is a true positive count. The values for the factor k_α are tabulated and for example for a 95% confidence level it is 1.645 [58]. In case of single counts σ_0 is [58]:

$$\sigma_0 = \sqrt{var(N)} = \sqrt{2B}. \tag{2.17}$$

Finally the critical limit with 95% degree of confidence can be written as:

$$L_C = 1.645 \cdot \sqrt{2B} = 2.33 \cdot \sqrt{B}. \tag{2.18}$$

In the current case it was found that N= 5.5 and $L_C = 6$. Thus no significant signal was detected.
At this point the aim of the analysis was focused on estimate an upper limit for the 395 keV resonance strength. Thus it was calculated the *upper limit* (L_U).
The L_U is defined as the maximum statistically reasonable value for the expectable counts with a defined degree of confidence. It is defined as [58]:

$$L_U = N + k_\alpha \sigma_N, \tag{2.19}$$

where σ_N is the standard deviation of the current measured value N. Using the same method as for σ_0 and taking into account that N was different from zero, it was possible to rewrite the upper limit as [58]:

$$L_U = N + 1.645\sqrt{(N + 2B)}, \tag{2.20}$$

where k_α was selected in order to have a 95% degree of confidence on the obtained value for L_U.
Because of the missing information on the beam induced background for the current experiment two approaches were used to calculate the upper limit. First the net count found was treated as due to the beam induced background, which, as already described, was not really measured. Under this assumption N was put to zero and B is the sum of the contributions from the laboratory background and the supposed

beam induced background, N. The second approach was to not take into account the beam induced background, that really cannot be estimated from data acquired, thus N is 5.5 and B is due only to the laboratory background. Both the results were used to determine the upper limit for the 395 keV resonance strength as it follows:

$$\omega\gamma_{u.l.} = \left(\frac{\lambda^2}{2}\right)^{-1} \cdot \frac{Y \cdot \epsilon_r}{\eta}, \tag{2.21}$$

where Y is the observed Yield defined as $\frac{detected\ reactions}{incident\ beam\ particles}$ and calculated for the current case as:

$$Y = \frac{L_U}{C \cdot 1.602 \cdot 10^{-19}}. \tag{2.22}$$

The factor $(\lambda^2/2)^{-1}$ is the de Broglie wavelength factor. The already introduced detection efficiency and the stopping power at the resonance energy are η, and ϵ_r respectively. The total charge collected is C and it is expressed in Coulomb. The values obtained were $\omega\gamma_{u.l.} = 0.7 \cdot 10^{-10}$ using the first approach and $\omega\gamma_{u.l.} = 1.1 \cdot 10^{-10}$ in the case of the second approach.
The two results differ less than the 40% and they are located between the result reported in [44, 49] and the result in [42]. The two values obtained for the 395 keV resonance strength were used to calculate its contribution to the ^{22}Ne(α,γ)^{26}Mg reaction rate as [3]:

$$N_t\langle\sigma v\rangle = \frac{1.5399 \cdot 10^{11}}{(\mu\, T_9)^{3/2}} (\omega\gamma)\, e^{-11.605 E_r/T_9}, \tag{2.23}$$

where μ is the already mentioned reduced mass of the system, T_9 is the temperature expressed in GK. The resonance strength ($\omega\gamma$) and energy (E_r) are in MeV. The new contribution was inserted in the ^{22}Ne(α,γ)^{26}Mg reaction rate reported in [48]. The ^{22}Ne(α,n)^{25}Mg reaction rate was taken from [48] too and then a new ratio of the two ^{22}Ne + α reactions rates was calculated. LUNA preliminary results are plotted in fig. 2.20 with those reported in literature.

2.4 Discussion

The ^{22}Ne + α reactions rate ratios obtained by LUNA with the two methods previously described do not differ significantly between each other in the temperatures range of interest for He burning (0.25 - 0.5 GK), see fig. 2.20. Indeed the maximum discrepancy is of about a factor 2 at T $\leq$ 0.25 GK.
Comparing LUNA results with those reported in literature there is a good agreement at T $>$ 0.5. On the other hand in the He burning temperature range the LUNA reaction rate ratios lay between those suggested by NACRE and Iliadis. In the new

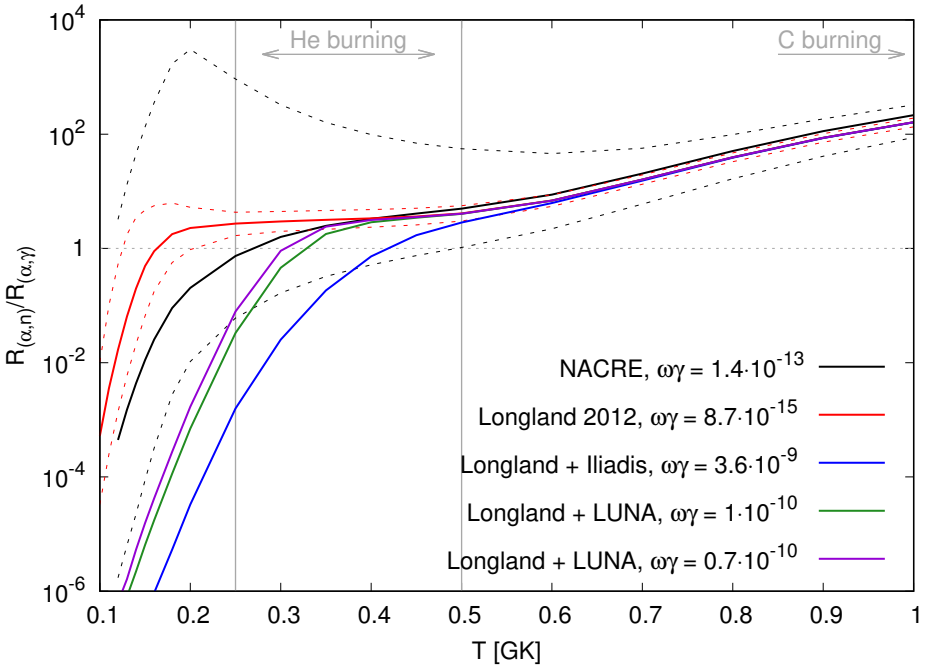

Figure 2.20: Ratio of the ^{22}Ne + α reactions rates suggested in literature and measured by LUNA (yellow lines). For scenarios with a ratio much below 1, the s-process neutron source is effectively closed down.

scenario the neutron production starts to be effective at T > 0.31 GK with great impact on the predicted s-nuclei production in low-mass AGB stars and in massive stars. The new cross-over temperature is in disagreement with all the previous ratios proposed in literature. As a matter of fact the (α,n) channel dominates at T corresponding to the He burning for both NACRE and Longland, while Iliadis suggested the neutron production to be effective at T > 0.4 GK. The discrepancy between LUNA results and NACRE and Longland reaction rate ratios increases for T $\leq$ 0.25 0.25 GK at which the ^{22}Ne(α,γ)^{26}Mg reaction dominates and the reaction rate ratio is more sensitive to the contribution of the 395 keV resonance. The LUNA result at low temperatures is expected to affect the predicted nucleosyinthesis in intermediate-mass AGB stars at T $\leq$ 2.5 GK.
Some problems were encountered and identified during the present study data acquisition and analysis:

- The contaminants in the target gas were monitored with a mass spectrometer and their amount was kept under a safety level for the analysis. However it was noticed an anomalous increasing of the nitrogen amount during the measurement. This was related to the presence of a leak in the gas target system.

- The energy calibration could be fixed up to $E_\gamma = 2.6$ MeV using the natural background peaks. The region of interest for the $^{22}Ne(\alpha,\gamma)^{26}Mg$ is at higher energy where the BGO energy calibration is known to be not linear anymore.
- The beam induced background was acquired with insufficient statistics. The missing knowledge of the beam induced background may lead to an incomplete evaluation of the background and thus to a wrong interpretation of the net count. Indeed possible contaminants may contributes to the ROI of the $^{22}Ne(\alpha,\gamma)^{26}Mg$ reaction.
- The neutron background, as visible in fig. 2.17, lays immediately on the left of the ROI of the $^{22}Ne(\alpha,\gamma)^{26}Mg$ reaction. In particular looking at the zoom in fig. 2.17 there are some counts in the ^{22}Ne sum of the addback spectra gathering on the left of the ROI, which may be a tail of neutron background or gammas from the $^{22}Ne(\alpha,\gamma)^{26}Mg$ reaction.

A new campaign of the $^{22}Ne(\alpha,\gamma)^{26}Mg$ reaction is actually ongoing at LUNA, for which some solutions were designed in order to avoid the problems encountered during the previous experiment. The setup of the previous campaign was almost entirely remounted and some parts, which were believed to be responsible for inlet of nitrogen in the system or which had to be repaired, were replaced. The nitrogen contamination will be monitored by performing periodic scans of the resonance at $E_p = 278$ keV, which will be used for the calibration of the BGO up to 7 MeV. More points for the calibration will be obtained decreasing the protons energy to 163 keV corresponding to a strong resonance of the $^{11}B(p,\gamma)^{12}C$ reaction. Indeed some boron contamination seems to be unavoidable in the setup, but this may not be a problem but an advantage because of its peaks at $E_\gamma \sim 4$ MeV, $E_\gamma \sim 11$ MeV and at $E_\gamma \sim 16$ MeV which can help in fixing the calibration up to high energies. The BGO is now shielded with a polyethylene borate box, 10 cm thick, in order to reduced the neutron background on the left of the region of interest for the $^{22}Ne(\alpha,\gamma)^{26}Mg$ reaction. The laboratory background and the beam induced background spectra were decided to be acquired in sequence with the run at $E_\alpha = 399.9$ keV, in order to be sure to collect the same statistics and at the same time. The expected impact of the new campaign on the previous results is either to measure the resonance or to reduce the upper limit found in the current study by one order of magnitude. This would definetely make the contribution of the 395 keV resonance to the $^{22}Ne(\alpha,\gamma)^{26}Mg$ reaction rate negligible and it would fix the role of the $^{22}Ne(\alpha,n)^{25}Mg$ reaction as neutron source for the s-process. In addition, it would better constrain both the AGB star and massive star model parameters and their impact on the chemical evolution of galaxies.

Chapter 3

The Study of the ^{6}Li(p,γ)^{7}Be Reaction at LUNA

3.1 Astrophysical Motivations

Cosmic-rays interactions in the interstellar medium are the main responsible for the ^{6}Li production. The cosmic-ray particles strike interstellar atoms, and, in those collisions involving carbon and oxygen atoms, fragments of the nuclei are broken off. These are called spallation nuclear reactions.
The predicted total amount of ^{6}Li produced during the Big Bang is $^6\mathrm{Li/H} = (1.34 \pm 0.44) \cdot 10^{-14}$ [61]. Stars are net destroyers of ^{6}Li and when finally their ejecta return to the interstellar material this is ^{6}Li-poor. In stars, ^{6}Li consumption proceeds via ^{6}Li(p,α)^{3}He and ^{6}Li(p,γ)^{7}Be reactions which are activated at $\mathrm{T} \sim 3\,\mathrm{MK}$. ^{6}Li is progressively depleted during the pre-main and the main sequence phases [1].
The so-called pre-main-sequence (PMS) phase is usually described with the following simple approach [62]. Stars are formed from interstellar gas by a gravitational instability. Whenever a sufficiently large mass of gas is compress to a small enough volume, its self-gravity guides the collapse. While the gas is contracting isotropically the gravitational potential is converted into thermal energy and only a small part of the energy is radiated, as a consequence the interior heats up. The star keeps on contracting along the so called Hayashi line. This represents the evolution of fully convective protostars whose luminosity drops because of the high opacity of the internal layers and because contraction decreases the surface area. The temperature, instead, remains almost constant along the Hayashi line. Stars with $\mathrm{M} < 0.35\,\mathrm{M}_\odot$ are fully convective all the way to the main sequence [63]. Stars with $\mathrm{M} > 0.35\,\mathrm{M}_\odot$ have lower central densities and as the temperature in the core, T_c, rises during PMS contraction, the opacity falls sufficiently to allow the formation of a radiative core which pushes outward to include a rapidly increasing fraction of the stellar mass. The age at which ^{6}Li depletion starts increases with decreases mass. For

more massive stars some amount of ^{6}Li remains which will restarts burning during the main-sequence phase at the bottom of the convective surface [1]. Because of the progressive depletion of ^{6}Li, its detection is a powerful tool to determine stellar age. In addition the ^{6}Li(p,γ)^{7}Be and the ^{6}Li(p,α)^{3}He reactions take place in the convective region of stars, thus ^{6}Li is considered a useful tool to study mixing processes in stellar interiors and to tune model parameters [63].
For an accurate determination of the stellar age as well as for a precise description of the mixing and magnetic processes taking place in stars a deep knowledge of the depletion processes of ^{6}Li is required.
In addition one of the unresolved problem of the Standard Big Bang Nucleosynthesis (SBBN) is the so-called *lithium problem* [64]. The original lithium problem consisted of the under abundance of ^{7}Li, detected in metal-poor Population II stars, with respect to (w.r.t.) the SBBN predictions. In addition to this in the same stars spectroscopic measurements, obtained with high resolution, indicate an over-abundance of ^{6}Li, about 3 order of magnitude larger than SBBN predictions [65]. Recently the possibility that the radiative decay of long-lived particles has affected the ^{6}Li production during the Big Bang was explored [66]. The primary and secondary nucleosynthesis triggered by the radiative decay processes of long-lived relic particles was calculated. It was found a parameter region leading to final abundances which are in agreement with the observations. One of the non-thermal photon induced reaction taken into account for the calculation is the ^{7}Be(γ_{nt}, p)^{6}Li. This was found to efficiently destroy ^{7}Be and produce ^{6}Li. In order to better constrain the calculation it would be preferable to have accurate data for the ^{7}Be(γ_{nt},p)^{6}Li reaction. A way to study the ^{7}Be(γ_{nt},p)^{6}Li reaction is through its inverse reaction, the ^{6}Li(p,γ)^{7}Be. The two reactions are related by the principle of detailed balance. The SBBN model would benefit from an improved determination of the cross section of the ^{6}Li(p,γ)^{7}Be reaction.
Despite its astrophysical importance the ^{6}Li(p,γ)^{7}Be cross section is still affected by high uncertainty. The current state of art for the ^{6}Li(p,γ)^{7}Be reaction is described in the next section.

3.1.1 State of Art

The ^{6}Li(p,γ)^{7}Be reaction was studied by many groups in the past and a recent warok renewed the interest.
The first search for the ^{6}Li(p,γ)^{7}Be reaction (Q_{val} = 5606 keV) was performed in 1939 and it had a negative result [67]. However in 1954 a complicated pattern of γ-rays was observed for bombarding energies from 400 keV to 2.2 MeV [68]. In order to clarify the γ-rays transitions scheme, one year later a new measurement was performed for proton energies between 180 keV and 415 keV [69]. At these energies three γ-rays were observed corresponding to the direct capture to the ground

state, the transition to the first excited state of ^{7}Be (E_x = 429 keV), which decays to the ground state, see fig. 3.1. The relative intensities were determined, 35% for the transition to the 429 keV state and 65% for the direct capture to the ground state. A following work found compatible results for the relative intensities but in the energy range from 400 keV to 1 MeV [70].
All the described studies were not properly devoted to the ^{6}Li(p,γ)^{7}Be cross section measurement. Indeed the cross section for the decay of the capture state through the 429 kev state was obtained at E_p = 415 keV in [69] while the differential cross section at the proton beam energy of 750 keV was reported in [70]. The first campaign to direct measure the ^{6}Li(p,γ)^{7}Be cross section took place in 1979 and it covered the energy range from 200 keV to 1.2 MeV [71]. Two types of targets were used, metal Li and lithium oxide both enriched to 99% ^{6}Li. The S-factor was calculated using the 429 keV γ-radiation and then analyzing the direct capture to the ground state transition. The results of the two analysis were in agreement. The S-factor was found to increase with decreasing energy, except for the last two points, see fig. 3.2. In addition new relative intensities for γ_0 and γ_1 were estimated and those were in agreement with the previous results. The cross-section was found to be in good agreement with the predictions from the optical potential model [72]. The direct-capture potential parameters were taken from the mirror reaction, the ^{6}Li(n,γ)^{7}Li as suggested in [73]. Both the model and the experimental results showed a negative slope for the S-factor at low energies, see the blue line in fig. 3.2.
Some years later, in 1992, a new measurement of ^{6}Li(p,γ)^{7}Be cross section found an opposite trend for the S-factor at low energies [74]. The measurement covered the proton energy range between 40 and 180 keV and it aimed to determine the angular distribution and the γ-ray-to-charged-particle branching ratio of the ^{6}Li(p,γ)^{7}Be reaction. The latter was used to deduce the S-factor of ^{6}Li(p,γ)^{7}Be reaction using a relative approach. As a matter of fact the γ-ray-to-charged-particle branching ratio is proportional to the ratio between the S-factors of the γ-channel and the charged particle channel. The ^{6}Li(p,γ)^{7}Be S-factor found with this approach showed a decreasing trend with decreasing energy, see the magenta dashed line in fig. 3.2.
A new theoretical study was performed in order to solve the puzzle of the slope of the ^{6}Li(p,γ)^{7}Be S-factor [75]. A four-cluster microscopic model was used to investigate the ^{6}Li(p,γ)^{7}Be cross section at low energy. The resulting S-factor increases with decreasing proton beam energy, in agreement with the experimental data by [71]. Two years later, in 2004, this result was confirmed by a new experimental study [76]. A polarized proton beam with energies between 80 keV and 130 keV was used to determine the slope of the ^{6}Li(p,γ)^{7}Be S-factor at low energies. The S-factor curve was extracted by fitting the integrated yields obtained from the spectra. The slope of the S-factor was found to be negative, see the green line in fig. 3.2. A following theoretical work came to the same result applying a simple two-body treatment to the ^{6}Li(p,γ)^{7}Be reaction [77].

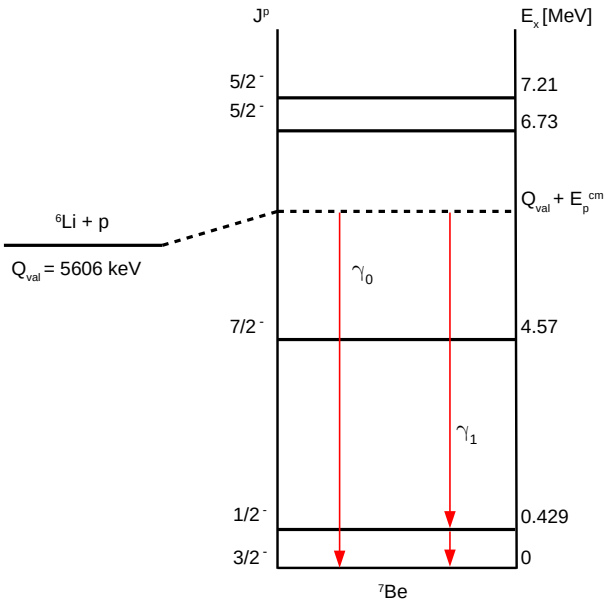

Figure 3.1: ^{7}Be levels scheme and the γ-rays produced by the ^{6}Li(p,γ)^{7}Be reaction for proton energies of interest for the present study.

More recently the interest for the puzzle of the ^{6}Li(p,γ)^{7}Be S-factor slope was renewed by the results reported in [78]. The direct measurement covered the proton beam energies between 60 and 300 keV. A relative approach was used to determine the ^{6}Li(p,γ)^{7}Be S-factor. The results were in agreement with the previous experimental data by [71] in the overlapping energy region, see the black dots in fig. 3.2. However they showed a resonance like structure at E_{cm} $\sim$195 keV never observed before, see the black dots in fig. 3.2. A positive parity, J^{π} $1/2^{+}$ or $3/2^{+}$ was assigned to the corresponding new excited state E_x $\sim$5.8 MeV [78]. This new positive parity level would solve the puzzle of the ^{6}Li(p,α)^{3}He angular distribution, which requires the contribution by both negative and positive parity excited states. Indeed it was observed that the ^{6}Li(p,α)^{3}He angular distribution is dominated by the A_1 coefficient [79]. An R-matrix fit of the data for A_1 requires the contribution of both negative and positive parity levels [80]. In addition the new resonance might also have some effect on the extrapolation of ^{3}He(α,γ)^{7}Be cross section at low energies. As a matter of fact the new resonance would affect the cross section of the ^{3}He(α,γ)^{7}Be reaction at higher energies w.r.t. those of astrophysical interest, $\sim$20 keV corresponding to the hydrogen burning through pp-chain temperatures. Nevertheless the new resonance may affect the extrapolation down to low energy. The new resonance was not confirmed by a more recent theoretical work [81]. The Gamow shell model, formulated in a coupled-channel representation, was applied

to the ^{6}Li(p,γ)^{7}Be reaction. The obtained curve was in qualitative agreement with the results obtained using either the microscopic cluster model [75] or the potential model [77]. The slope of the S factor was found to be negative and the resonance was not confirmed. The results reported in [71] and in [78] have been recently re-analyzed taking into account a new determination of the spectroscopic factor for the ^{7}Be ground state [82]. The direct capture component was calculated using the FRESCO code. The analysis of the experimental data for the total S-factor was performed with the R-matrix code AZURE. The best fit was used to obtain the 195 keV resonance parameters.
From the picture described above it is clear that there are still many open questions on the ^{6}Li(p,γ)^{7}Be S-factor. Because of the impact the new resonance would have and because of the still unsolved puzzle of the S-factor trend at low energies, which are those of interest to constrain better the extrapolation to the gamow peak energies, between 3 and 20 kev corresponding to T = 5 MK (see fig. 1.2) a new direct measurement is needed.

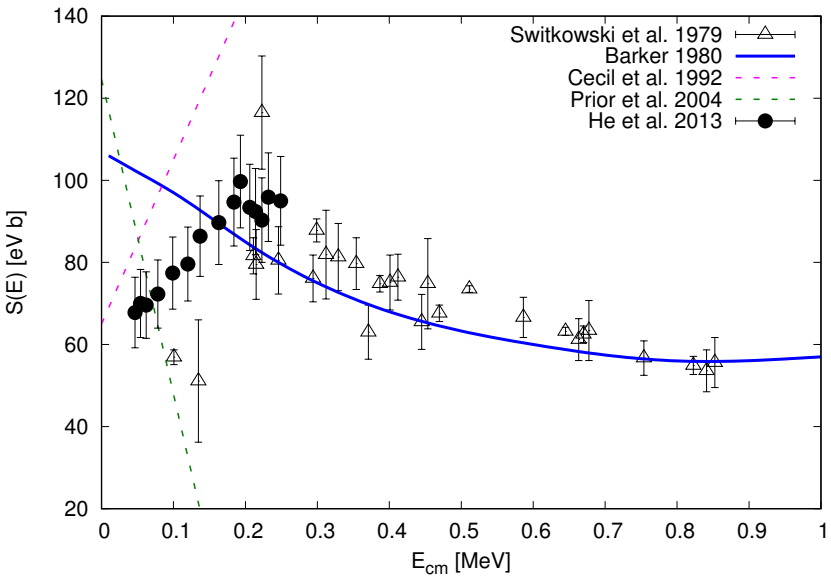

Figure 3.2: Experimental ^{6}Li(p,γ)^{7}Be S-factor data reported in [71, 78]. The theoretical prediction by [72] is shown for comparison.

3.2 Experimental Setup

The study of the ^{6}Li(p,γ)^{7}Be was performed at the solid target beamline at LUNA400kV. Many focusing and collimating steps were installed on the beamline

to improve the beam transmission. The scattering chamber and the target holder were designed to minimize target degradation, to guarantee a correct reading of the beam current and in the most convenient geometry for the measurement. An High Purity Germanium detector (HPGe) and a Silicon (Si) detector were added to the beamline in order to detect the γ-rays from ^{6}Li(p,γ)^{7}Be reaction and the α-particles from the ^{6}Li(p,α)^{3}He reaction. The next sections are devoted to the description of the experimental setup.

3.2.1 The Solid Target Beamline

The high intensity proton beam passes through different focusing and collimating sections (fig.3.3) before reaching the scattering chamber, which is described in the next section. Once extracted from the source and accelerated the proton beam is guided to the target station by the following tools, see fig. 3.3:

- The magnetic steerer allows to optimize the vertical position of the beam and thus the transmission through the beamline;
- The magnetic quadrupole lenses allow both to focus and to optimize the shape of the beam;
- An analyzer magnet switches the beam by an angle of 45° to the scattering chamber;
- The Wobbler, positioned at 45° w.r.t. the plane perpendicular to the beam, generates a wave function along this direction. The wobbler system induces an oscillator motion of the centroid of the beam which leads to a uniform irradiation over a defined region of the target;
- The *upstream aperture* is the first static collimator encountered by the beam. Three different circular apertures are available, 16.4 mm, 6 mm and 4 mm diameter respectively. Two actuators allow to move from one to the the other aperture and to optimize the vertical and horizontal position. For the current measurement the 16.4 mm diameter aperture was used;
- The *downstream aperture* is the last static collimator before reaching the scattering chamber. Three apertures are available: two circular collimators, 3 mm and 5 mm diameter respectively, and one slit 1.5 mm large and 4 mm long. Similarly to the upstream collimator two actuators allow to select the aperture and to optimize the position. For the current measurement the 3 mm diamater aperture was used; The downstream aperture ensures the final beam size can fit inside the target area. The final configurations for the two apertures were find as optimal after the beamline alignement with optical tools and with beam transmission tests;

Both the upstream and the downstream apertures allow monitoring the beam current, which is fundamental in order to optimize the beam transmission and focussing. In addition two insertable Faraday cups, namely FC0 and FC45, were positioned at the exit of the accelerator and after the analyzer magnet respectively, see fig. 3.3. Because of the high intensity of the beam both the collimators and the faraday cups are water cooled. All the materials used for the beam line and in particular for the collimators and the faraday cups were chosen in order to minimize the beam induced background. The focusing and collimating tools parameters can be set by a PLC-based computer located in the control room. Moreover the Faraday cups are remotely controlled.
The beamline between the analyzer magnet and the scattering chamber is kept at a pressure of about 10^{-6} mbar by a turbomolecular pump by Leybold installed after the downstream aperture.

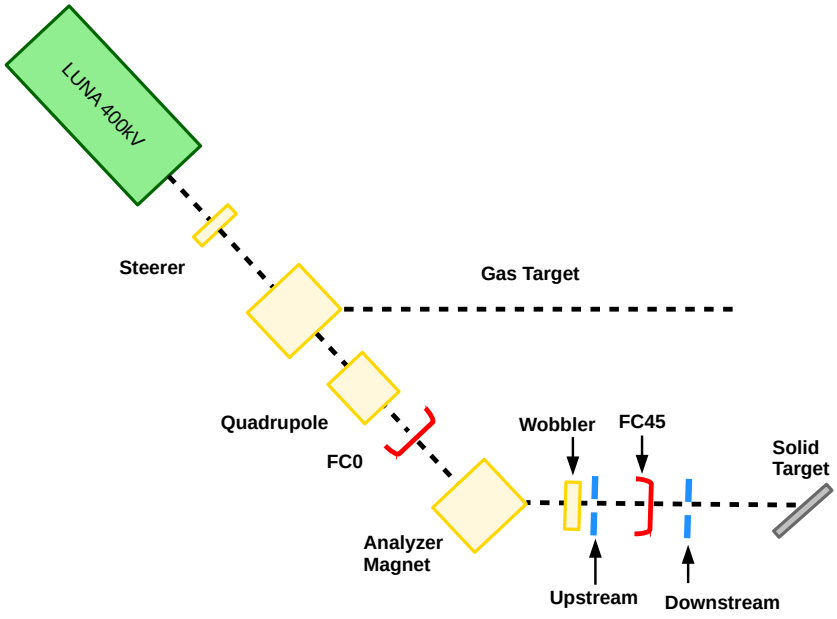

Figure 3.3: A schematic draw of the solid target bemline at LUNA. The optics and beam collimators along the solid target beamline are indicated.

3.2.2 The Scattering Chamber

After passing through the downstream aperture the beam enters the scattering chamber and finally it reaches the target, described in the next section. Both the scattering chamber and the target are insulated from the target beamline, thus they work as a Faraday cup allowing to determine the total charge accumulated during

a measurement.

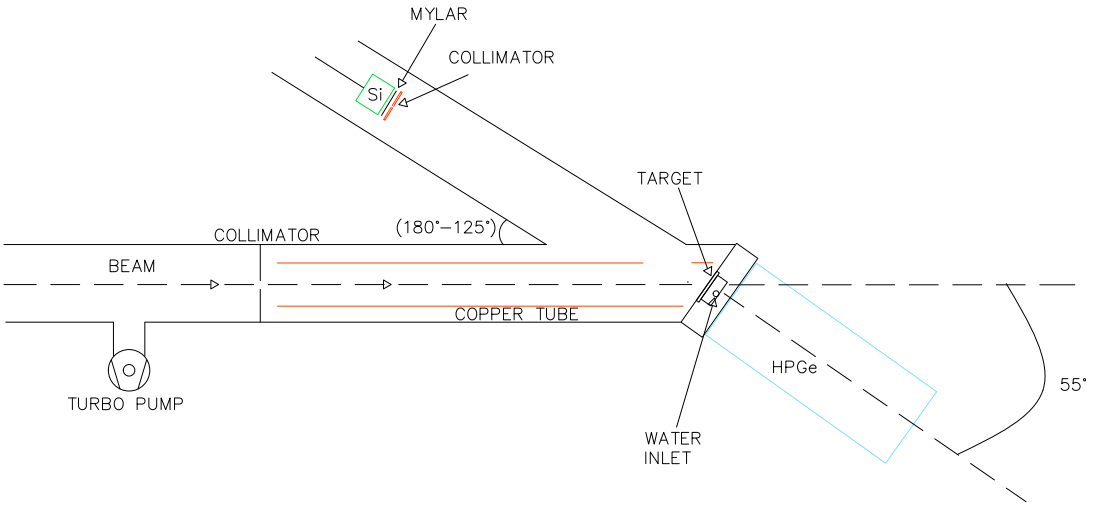

Figure 3.4: A plot of the scattering chamber. Not to scale

Because of the interaction of the beam particles with the target, electrons may escape the target leading to an incorrect current reading. A copper tube was installed after the downstream aperture to which a negative potential of 300 V was applied to deflect electrons emitted from the target back onto it, see fig. 3.4. The exit end of the copper tube was cut in order to be parallel to the target surface. The distance between the copper tube and the target was about 10 mm. The copper tube was insulated from the scattering chamber and the target beamline. In addition the copper tube was used as cold finger to prevent deposition of carbon on target during the measurement. In order to keep the copper tube cold this was in thermal contact with LN_2.
At the end of the copper tube a oval aperture was cut, see fig. 3.5, allowing the α-particles and the ^{3}He particles produced by the ^{6}Li(p,α)^{3}He reaction to be detected by the Si detector. This was located inside the scattering chamber arm at 125° w.r.t. the beam direction, see fig. 3.4. The γ-rays by the ^{6}Li(p,γ)^{7}Be are detected by a coaxial HPGe (hereinafter HPGe) located in close geometry in front to the target

holder, see fig. 3.4. In the following sections the detectors and the data acquisition system are described and characterized.

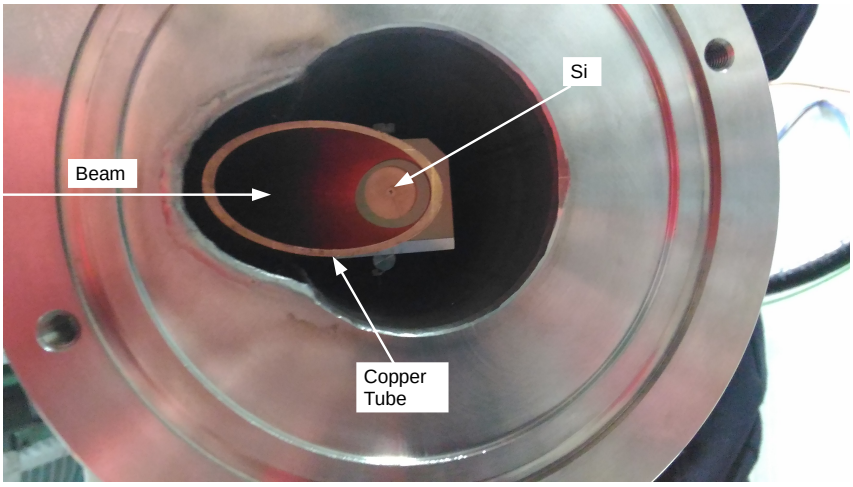

Figure 3.5: The scattering chamber as seen from the target side. The copper tube coming installed inside the beamline. Through the hole in the copper tube the Silicon detector is visible.

3.2.3 The Target

The target was mounted on a brass flange positioned at 55° w.r.t. the beam axis, see fig. 3.4 and fig. 3.6. The flange was customized in order to hold the target and to house the water cooling system. In order to minimize any damage due to beam-heating effects the target must be directly cooled. The cooling water was free to flow directly on the back of the target inside a circular hole (9.8 mm depth) obtained in the flange and connected to the inlet and the outlet tubes, see fig. 3.6. For the present measurement six targets of different composition and thickness were irradiated and they are listed with corresponding features in tab. 3.1.
The lithium is known to oxidize rapidly in air, thus in order to get a stable target it was decided to use enriched lithium compounds, namely lithium oxide, lithium tungstate and lithium chloride.

The powder of Li_2O was produced by the chemistry laboratory at LNL (Laboratori Nazionali di Legnaro), while the powder of Li_2WO_4 was bought from Sigma

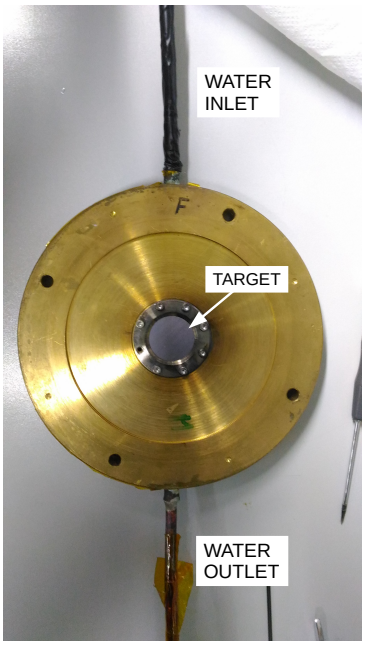

Figure 3.6: Left the target holder without the targets in order to appreciate the water cooling system. Right the target holder with a lithum target. The picture was taken during the feasibility test some month before the measurement.

Aldrich company, chemical purity $\geq 98\%$. Finally the LiCl was produced by the chemistry laboratory at University Federico II of Naple. The nominal enrichment in ^{6}Li is 95% for all the compounds.
Except for the LiCl, the enriched lithium compounds were evaporated on a disk shape tantalum backing 0.25 mm thick. In order to reduce the beam induced background, before the evaporation, the backings were cleaned at LNL using a mix of nitric and hydrochloric acids which was found to be very effective in past experiments.
The evaporation procedure was performed at the ATOMKI laboratories in Debrecen (Hungary). The evaporation was done using a Leybold UNIVEX 350 evaporator. The Li_2O or the Li_2WO_4 powder was put into a tantalum holder, referred as the *boat*, which was resistively heated by DC current (~ 60 A). During the evaporation the vacuum inside the evaporator was of about 10^{-5} mbar. The tantalum backing was positioned 10 cm above the boat in order to obtain a uniform deposition layer. The evaporation process was controlled with a quartz thickness monitor, which can measure the thickness of the deposition online. Target composition can change during the procedure and the nominal target thickness estimated starting from evaporation parameters is affected by high uncertainty. For these reason the target thickness and composition are usually measured experimentally. The methods exploited for

the current study are described in sec. 3.3.
The low melting LiCl was heated directly on the copper backing. Once melted the LiCl expands on the backing and then it solidifies in a thick film. The stoichiometry is hard to monitor with this technique.

Producer	Nominal Composition	Nominal Thickness [μg/cm^2]
LNL	Li_2O-7	40
LNL	Li_2O-9	20
Sigma Aldrich	Li_2WO_4-3	100
Sigma Aldrich	Li_2WO_4-4	100
Univ. Naple	LiCl	Infinite
Sigma Aldrich	Li_2WO_4-1	130

Table 3.1: List of the targets used for the current study, the number following the compound is an identification number. The targets are sorted by irradiation order. The producer and the different thickness are listed too.

3.2.4 Detectors and DAQ

HPGe Detector

The HPGe detectors are based on semiconductive properties of germanium. Thanks to the small band gap of Ge (0.7 eV) which guarantee a high number of charge carriers, the HPGe have high resolution ($\sim$ 2 keV at $E_\gamma = 1.3$ MeV [83]). On the other hand they have a low efficiency w.r.t. the scintillators for $E_\gamma \geq 1$ MeV, due to the limited volume and to the lower atomic number of germanium detectors compared with scintillators [83]. The HPGe low efficiency is not a limit for the current study because the expected counting rate is high and in a region of the γ-spectra where the background is higly suppressed at LUNA.
But for the study of the ^{6}Li(p,γ)^{7}Be reaction the HPGe high resolution is a fundamental requirement. The transition to the first excited state is 82 keV apart from the *first escape* of the direct capture to the ground state, more details will be provided in sec. 3.3. Keeping in mind that the DC peaks are naturally broad because it represents the convolution of the cross section, the target profile and the detector resolution, we could encounter problems to distinguish the two peaks with a low resolution detector. Finally the analysis of the peak at 429 keV may provide some important cross checks. The 429 keV peak is in the low energy part of the spectrum dominated by the laboratory background. In order to perform a correct identification and analysis, this peak must be well separated by the background peaks, thus

a high resolution is needed.
An ORTEC coaxial HPGe detector, model number: GEM-120225-P-ST, was used for the gamma-ray spectroscopy of the ^{6}Li(p,γ)^{7}Be reaction. After the last maintenance in 2016 the reported relative efficiency at 1.33 MeV is 104%. The crystal dimensions reported in the original datasheet are: 84.6 mm diameter, 87.8 mm length.
The HPGe was positioned parallel to the target holder, thus at 55° w.r.t. the beam direction, see fig. 3.7, to reduce possible angular correlation effect. Indeed the relative probability that a photon will be emitted at an angle θ w.r.t. a previously emitted photon of the cascade is denoted as $W(\theta) = 1 + a_2Q_2P_2(\cos\theta) + a_4Q_4P_4(\cos\theta)$. The terms $a_{2,4}$ are angular coefficients typical for each transition and $Q_{2,4}$ represent the attenuation factors due to the finite solid angle. For $\theta = 55°$ the second order polynomial $P_2(\cos\theta)$ is zero and thus the angular correlation effects are minimized.
The HPGe was positioned at 4 mm from the target holder, which corresponds to a real target to detector distance $d \sim 1.7$ cm, taking into account the dimensions of the flange (see fig. 3.7).

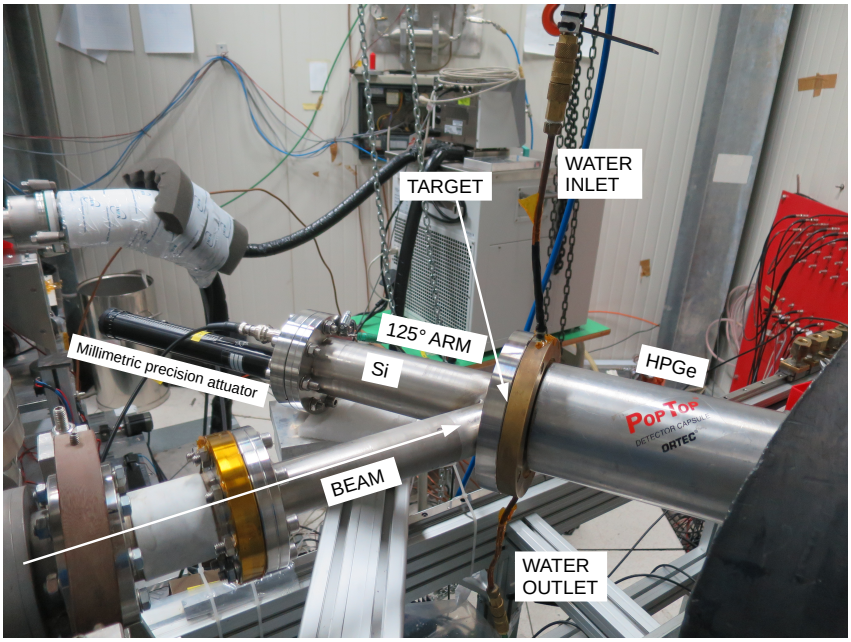

Figure 3.7: The experimental configuration during the measurement. The HPGe is in close geometry. The Silicon is not visible and it is inside the 125° arm.

The HPGe was on a movable frame allowing to move the detector back and forth to change the target and to study the True Coincidence Summing (TCS) effect, which is described in sec. 3.2.5 together with the measurement of the efficiency.

Si Detector

The direct measurements exploiting solid targets may be affected by high uncertainty mainly due to the inaccurate determination of the target profile during the run and/or of the charge collected on target. In order to reduce the uncertainties a relative approach may be performed. For the present work the ^{6}Li(p,γ)^{7}Be experimental data are compared with the experimental and literature data for the ^{6}Li(p,α)^{3}He reaction, more details about this method will be described in sec. 3.3. In order to investigate the ^{6}Li(p,α)^{3}He reaction a particle detector was needed.
The most common particle detectors are the Si detectors which have many advantages. They are used as detectors since many years, they do not need to be cooled and they can be of different size and shape, thus they are very adaptable. In addition the Si detectors have an intrinsic efficiency of 100% and they work in a large range of energy.
For the measurement of the ^{6}Li(p,α)^{3}He reaction an ultra low background Si detector by ORTEC, model BU-014-025-100, was installed at 125° w.r.t. the beam direction, see fig. 3.7. The active area of the Si detector was 25 mm^2 and its depletion depth was 100 μm. It was mounted on a movable holder fixed to the CF flange which closed the 125° arm. The actuator of the Si holder was outside the scattering chamber and it had a millimetric precision, see fig. 3.7 and fig. 3.8. The Si detector was inserted in a insulating PEEK support fixed to the movable holder. A circular copper collimator, diameter 1 mm, was positioned in front of the detector to limit the intensity of the particles impinging on the Si surface, see fig. 3.5.
The expected particles that can be detected by the Si are the scattered beam protons and the ^{3,4}He particles produced by the ^{6,7}Li + p reactions. The ^{3,4}He particles produced by the ^{6,7}Li + p reactions are expected to have very different energies, see tab. 3.2, thus no overlaps or beam induced background problems are expected in the spectra.

Source	Particle	E_{mylar} [MeV]	E_{Si} [MeV]
^{6}Li(p,α)^{3}He	^{3}He	2.2	1.2
^{6}Li(p,α)^{3}He	^{4}He	1.65	0.5
^{7}Li(p,α)^{4}He	^{4}He	8.5	8.1
p + target	p'	$\leq$ 0.4	0

Table 3.2: List of the expected particles detectable from the Si detector during the measurement. Their energies at the mylar foil surface (E_{mylar}, and after having passed through the mylar foil at the Si surface are reported, E_{Si}. The energy for the ^{3,4}He particles does not change significantly with the proton beam energy, thus the reported value is a mean E.

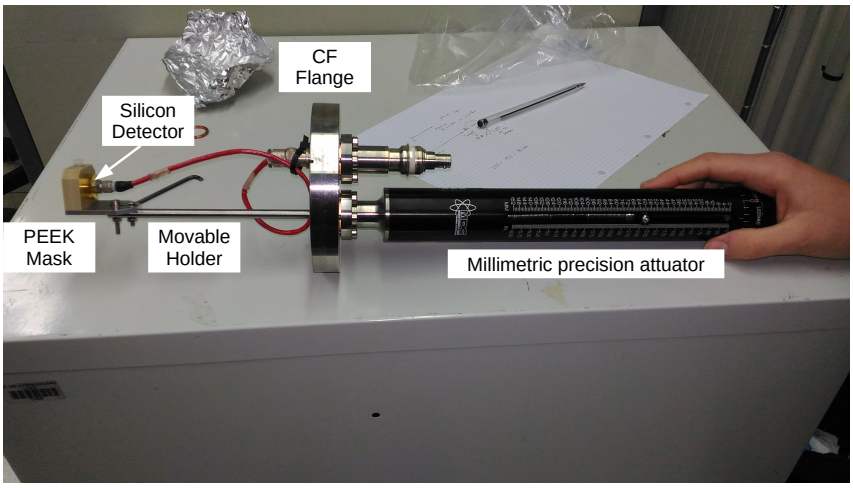

Figure 3.8: The Si detector and its holder before the installation on the scattering chamber.

The scattered beam protons are expected to represents a problem, they are expected to have a high counting rate which can damage the Si detector. In order to stop the protons a mylar foil 5 μm thick was inserted on the surface of the Si detector. The range of protons at $E_p \leq 400$ keV in mylar is ≤ 5 μm. The scattered beam protons stopped into the 5 μm mylar foil while the particles of interest are slowed down. The mylar foil was mounted between the collimator and the Si detector.

DAQ

A scheme of the Data Acquisition system is plotted in fig. 3.9. Each detector has a devoted digital acquisition chain and an independent power supply. The high voltage power supply is provided to the HPGe by a Dual 5kV Bias Supply by ORTEC, while the Si was connected to a 1 kV Quad Bias Supply by ORTEC. The HPGe required 4900 V, while the Si needed 50 V. The HPGe has its own preamplifier. The output from the HPGe preamplifier is processed by a spectroscopic amplifier by ORTEC. After having been processed by the amplifier the signal is delivered to channel 1 of the MCA Aspec 927 by ORTEC. The signal from the Si detector is processed by a preamplifier and then by an amplifier by ORTEC. Finally it is delivered to channel 2 of the MCA, which is connected via USB cable to a devoted pc in the control room. The signals are read by the MAESTRO multichannel analyzer software.

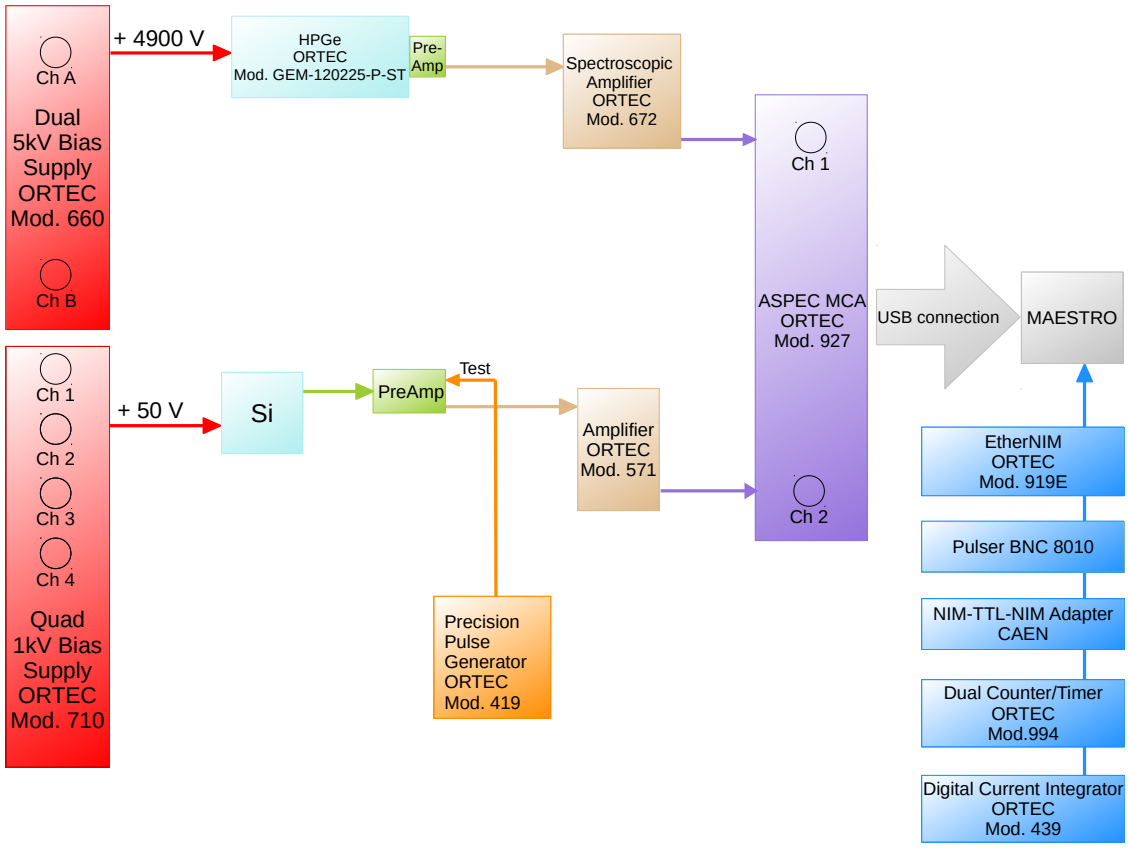

Figure 3.9: DAQ electronics scheme

A channel of MAESTRO is devoted to read the charge collected on the target. As a matter of fact, even if the current integrator connected to the target shows the charge on a digital display, this number must be manually noted at the end of each measurement. In addition the current integrator must be manually reset after each run and it must be started and stopped at the same time as the acquisition. In order to avoid to depend on the fragile manual reporting of the charge from the display on the logbook, it was decided to have an indipendent acquisition chain for the charge. The current integrator was connected to a dual counter/timer by ORTEC which allows to add online the information of time to the charge counts. The dual counter/timer output is then processed by a NIM-TTL-NIM adapter by CAEN. The adapted signal generates a pulse thanks to the Pulser BNC 8010. The pulses are processed by the EtherNIM by ORTEC and finally they are read by MAESTRO. The charge appears as a peak at channel 7540. After each run all the three spectra were saved in a .Spc format then converted in a more practical ASCII format.

3.2.5 Detection Efficiency

Si Efficiency

In order to reproduce the ^{6}Li(p,γ)^{7}Be measurement condition, as the beam size and position on the target, the Si efficiency was measured exploiting the isotropic resonance at 151 keV ($\omega\gamma$ =164.2 meV) of the ^{18}O(p,α)^{15}N [84]. A scan of the resonance was performed in order to fix the proper proton energy for the efficiency measurement, see fig. 3.10, The target composition was Ta_2O_5, 99% enriched in ^{18}O.

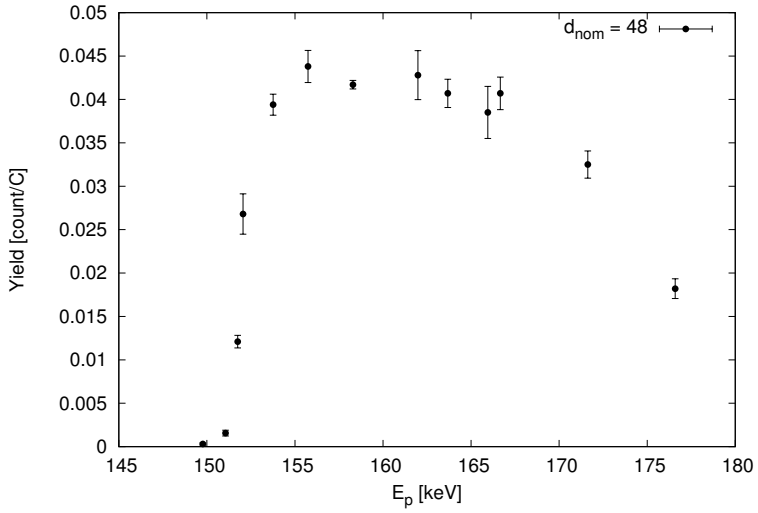

Figure 3.10: Investigation of the 151 keV ^{18}O(p,α)^{15}N resonance.

It was irradiated at E_p $\sim$158 keV at seven different source to detector distances from 48 mm up to 112 mm, in order to investigate the dependency of the efficiency on the distance.
The Si detectors efficiency should correspond to the relative solid angle defined as:

$$\frac{\Omega}{4\pi} = \frac{A_{active}}{(4\pi \cdot d^2)}, \tag{3.1}$$

where A_{active} is the active surface of the Si, which is defined by the collimator in the present study. The source to detector distance is d. The experimental data are plotted as black points in fig. 3.11 and they were obtained using the following relation valid in case of thick target ($\Delta E >> \Gamma_R$, the energy loss inside the target is higher than the resonance width):

$$Y_{max} = \frac{\lambda^2}{2} \cdot \frac{\omega\gamma}{\epsilon^r_{eff}} \cdot \frac{M_1}{M_1 + M_2}, \tag{3.2}$$

where $\omega\gamma$, λ and ϵ^r_{eff} are the resonance strength, de Broglie wavelength and the effective stopping power at the resonance energy. The Y_{max} is:

$$Y_{max} = \frac{A}{Charge \cdot \eta_{Si}}, \tag{3.3}$$

where A is the area of the peak of interest derived integrating in a proper region of interest, while charge is the total collected charge on the target and η_{Si} is the efficiency of the Si detector. Combining the two equations above, having all the information about the resonance and the target as well as all the necessary experimental data the η_{Si} can be derived for each source to detector distance. In fig. 3.11 the solid angle dependency on the source to detector distance is plotted with a blue line. A possible explanation of the discrepancy found was suggested in a previous experiment at LUNA [84], when it was observed the deviation of the beamspot size and position from the ideal condition of the centered pointlike source produced a 20% discrepancy in the efficiency. The experimental beamspot is highlighted in fig. 3.12. Because the target is tilted w.r.t. the beam direction the beamspot is an ellipse. The most intense beamspot is the real one while the halo is due to beam heating effect and to the beam focusing procedure. The beamspot is also off-centered. In order to

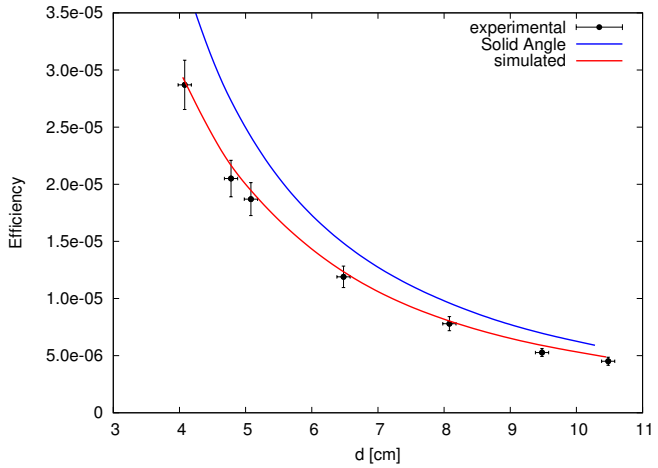

Figure 3.11: Comparison between the experimental data, black dots, the expected solid angle, blue line and the simulation results red line.

investigate the hypothesis above a Geant3 code was implemented which simulates the experimental setup. The measured efficiency was reproduced simulating a circular beamspot of radius R = 5 mm, which becomes an ellipse when projected on the target at 55° w.r.t. the beam direction, and 3 mm shifted w.r.t. the target center, red line in fig. 3.11.

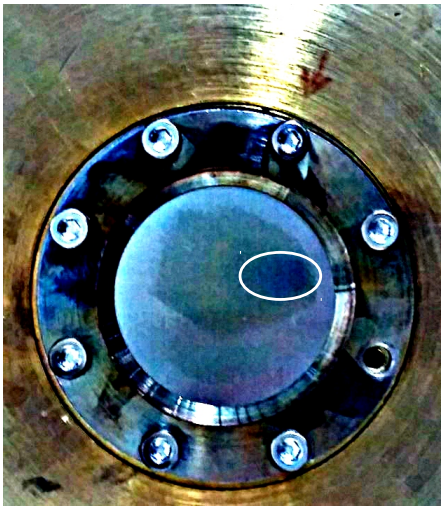

Figure 3.12: The target of Ta_2O_5 after the efficiency measurement. The beamspot is highlighted. The contrast of the picture was enhanced artificially in order to see better the beamspot and the halo.

HPGe Efficiency and Summing Correction

The efficiency calibration is usually performed at many γ-rays energies, covering the region of interest, at the measurement source to detector distance. The three γ-rays of interest lay between 400 keV and 6000 keV. The efficiency at low energies ($E_\gamma < 2000\,\text{keV}$) was fixed using three standard calibrated pointlike sources by PTB: the ^{137}Cs, the ^{60}Co and the ^{88}Y, more details are in table 3.3 and the half-life are listed in tab. 2.2. The ^{137}Cs decay radiation is dominated by the 662 keV γ-ray while the other two sources presented a two transitions cascade structure to the ground state. The ^{60}Co decays with 99% probability to the 2507 keV level of ^{60}Ni via beta emission, and this state de-excites by a γ-ray cascade through the 1332 keV level (lifetime: 0.7 ps). The ^{88}Y decays with 92% probability to the 2734 keV level of ^{88}Sr via beta emission, and this state de-excites by a γ-ray cascade through the 1836 keV level (lifetime: 0.15 ps). All the sources were located in a thin plastic layer which was fixed on the target holder in the same way as the targets. The efficiency calibration was extended up to 7 MeV exploiting the cascade structure of the resonant state of the ^{14}N(p,γ)^{15}O reaction [60]. Each excited state fed by the resonance dacays to the ground state with 100% probability, see fig. 3.13.

In case of γ-rays cascade with intermediate states lifetime shorter than the detector resolution time and big solid angle covered by the detector in order to obtain the efficiency curves one has to correct the experimental data for the True Coincidence

Isotope	E_{γ_1,γ_2} [keV]	I_{γ_1,γ_2} [kBq]	Ref. Activity [dd/mm/yy]	Ref. Date
^{60}Co	1173.2, 1332.5	99.85, 99.98	9.01 ± 0.07	1^{st} July 2016
^{88}Y	898, 1836.1	93.7, 99.2	0.76 ± 0.023	1^{st} June 2016
^{137}Cs	661.7	85.1	6.46 ± 0.07	1^{st} July 2016

Table 3.3: The features of the standard sources used to calibrate the HPGe at low energies

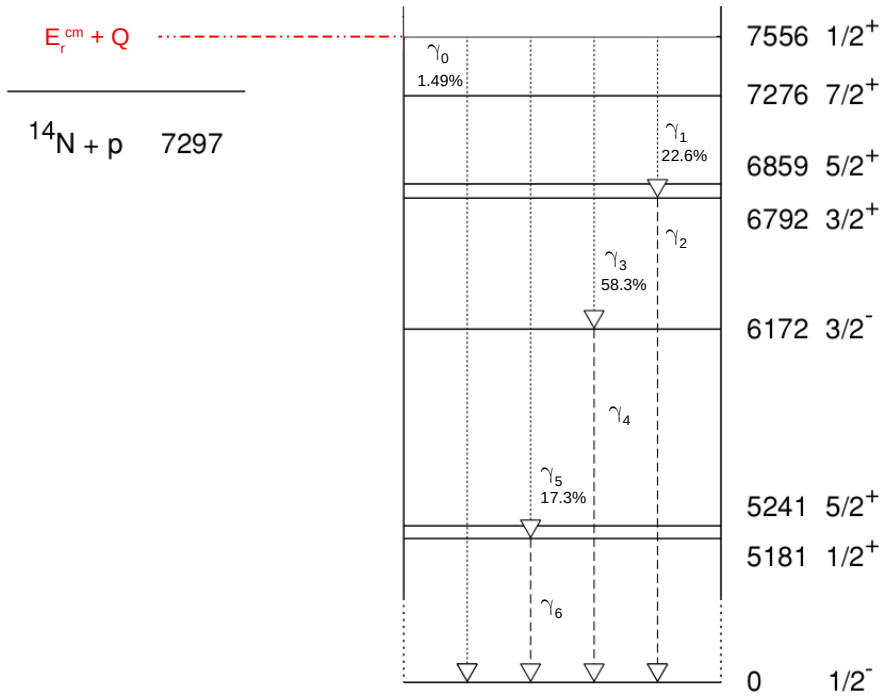

Figure 3.13: The cascade of ^{14}N(p,γ)^{15}O at the 278 keV resonance.

Summing (hereinafter TCS).
Assuming a simple decay scheme as in fig. 3.14 there is a high probability the HPGe in close geometry will record only one pulse for γ_1 and γ_2 at $E = E_{\gamma_1} + E_{\gamma_2}$. As a matter of fact γ_1 and γ_2 are *coincident* for the detector. The probability of TCS depends on the solid angle subtended by the detector, decreasing the solid angle (increasing the source-to-detector distance) the TCS becomes negligible. The effect of TCS on experimental efficiency data is to underestimate the efficiency at E_{γ_1} and at E_{γ_2} while the efficiency at the summing peak energy will be overestimated. It

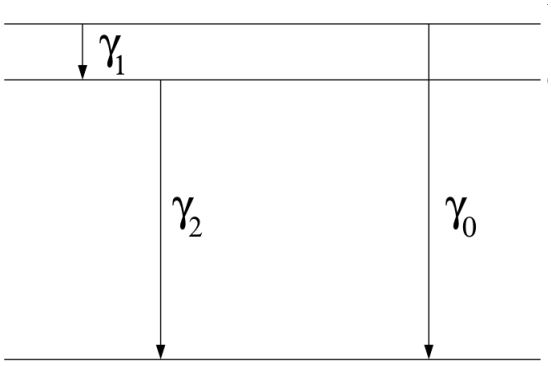

Figure 3.14: A simple decay scheme to illustrate the true coincidence summing.

is possible to correct for the TCS analytically or by the use of simulations. In the present work the first approach is used and it is described below taking as reference the cascade scheme shown in fig. 3.14.
The observed count rate in the full-energy peak of γ_1 would be without the TCS:

$$\eta_1 = R \cdot b_1 \cdot \eta_{fe1}, \tag{3.4}$$

where R is the true rate of the transition, b_1 is the branching-ratio of the transition and η_{fe1} is the full energy peak efficiency. Similar equations can be applied to the full energy peak count rate of γ_2 and γ_0. Because of the TCS some counts from the γ_1 peak will be lost by summing with γ_2, *summing-out* phenomenon, and thus the observed full energy peak count rate is:

$$\eta_1^{'} = R\, b_1\, \eta_{fe1} \; - \; R\, b_1\, \eta_{fe1}\, \eta_{tot2}. \tag{3.5}$$

The lost counts correspond to the conditional probability that γ_1 is detected in the full energy peak and γ_2 is detected anywhere in the spectrum: $R\, b_1\, \eta_{fe1}\, \eta_{tot2}$. The same equation as eq. 3.5 can be written for the observed count rate of γ_2 in case of 100% de-excitation to ground state:

$$\eta_2^{'} = R\, b_1\, \eta_{fe2} \; - \; R\, b_1\, \eta_{fe2}\, \eta_{tot1}. \tag{3.6}$$

On the other hand for each simoultaneous complete absorption of γ_1 and γ_2 a count would be produced in the summing peak, *summing-in* phenomenon, thus the observed count rate for γ_0 will be enhanced as following:

$$\eta_0^{'} = R\, b_0\, \eta_{fe0} \; + \; R\, b_1\, \eta_{fe1}\, \eta_{fe2}. \tag{3.7}$$

The equation above can be generalized for more complex decay schemes, as for example the resonant cascade of ^{14}N(p,γ)^{15}O fig. 3.13:

$$\eta_0^{'} = R\, b_0\, \eta_{fe0} \; + \; R\, b_1\, \eta_{fe1}\, \eta_{fe2} + \; R\, b_3\, \eta_{fe3}\, \eta_{fe4} + \; R\, b_5\, \eta_{fe5}\, \eta_{fe6}. \tag{3.8}$$

The equation above must be multiplied by W(θ), defined in sec. 3.2.4, in case of angular correlation between γ_1 and γ_2.
In order to perform the correction for the TCS the absolute full-energy peak efficiency (η_{fe}) is needed and it is defined as the ratio between the counts in the peak and the number of γ-rays emitted. It depends on the intrinsic efficiency of the detector and on the geometry. The relation between the full-energy efficiency, the source to detector distance and the γ-ray energy can be parametrized as [58]:

$$\eta_{fe} = A \cdot e^{(a+bln(E_\gamma)+cln(E_\gamma)^2)}, \tag{3.9}$$

where a, b and c are free parameters to be determine by a χ^2 fit and A is defined as following [58]:

$$A = \frac{1 - e^{\frac{d+d_0}{d_1+d_2\sqrt{E_\gamma}}}}{(d+d_0)^2}. \tag{3.10}$$

The free parameters d_0, d_1 and d_2 take into account for the exact position of the photon absorption event and for the dead layers between the end cup of the detector and the active volume of the crystal. The source to detector distance is d.
In addition the absolute total efficiency (η_{tot}) is needed for the present analysis, which relates the peak area with the number of γ-rays detected elsewhere in the spectrum due to incomplete absorption. A similar relation as eq. 3.9 exists for the total efficiency [58]:

$$\frac{\eta_{fe}}{\eta_{tot}} = e^{(K_1+K_2ln(E_\gamma)+K_3ln(E_\gamma)^2)}, \tag{3.11}$$

where K_1, K_2 and K_3 are free parameters.
In order to find the efficiency curve parameters in eq. 3.9 and 3.11 the efficiency measurement was performed acquiring spectra for all the sources at seven different source-to-detector positions from 4 mm up to 254 mm. The areas of primary and secondary γ-ray peaks listed in tab. 3.3 were obtained by integrating in a proper ROI and subtracting a linear background. The rates η'_{γ_i} were calculated as the ratio: Area/L.T. .
At the same detector positions a TiN target of unknown thickness was irradiated at E_p = 285 keV, which corresponds to the plateau of the 278 keV resonance scan performed before the efficiency measurement, as for the Si efficiency case. The analysis of the ^{14}N(p,γ)^{15}O was performed similarly as for the source peaks. At each target change or refill of the HPGe dewar the detector was moved back and forth. In order to estimate the systematic error originated by the repositioning of the HPGe during the measurement of the efficiency, both with radioactive sources and with the TiN target, the run at position 4 mm was repeated several times. It was found a 4% systematic error on the efficiency which was also useful to fix a lower limit for the expected uncertainty on the TCS correction procedure. The experimental results were fitted with the eq. 3.9 and 3.11 in two steps: first the

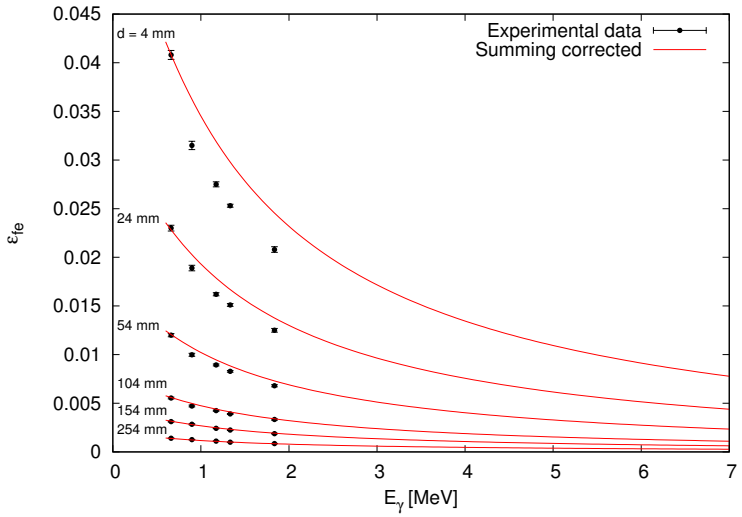

Figure 3.15: The experimental data in black compared with the corrected full-energy efficiency curves (red lines).

fitting procedure was applied only to the sources data in order to fix the parameters at low energies, then the ^{14}N(p,γ)^{15}O data was inserted in order to tune the fit at high energy. It must be noticed that in the case of the ^{14}N(p,γ)^{15}O data the real rate R in eq. 3.5, 3.6 and 3.7 was an additional free parameter, while for the sources R was calculated as the nominal activity at the measurement time. The multi-parametric fit was constrained by minimizing the discrepancy between the observed count rates (left sides of eq. 3.5, 3.6 and 3.7) and the expected count rates affected by the summing (right sides of the eq. 3.5, 3.6 and 3.7). In addition in order to get some initial guesses for the parameters the data for ^{137}Cs at all the source to detector distances and the data for all the sources at d = 254 mm were used. As a matter of fact the ^{137}Cs decay produces only one γ-ray at 662 keV thus it is not affected by TCS, moreover if the E_γ is fixed the eq. 3.9 becomes:

$$\eta_{fe} = \frac{1 - e^{\frac{d+d_0}{d_1+d_2\sqrt{E_\gamma}}}}{(d+d_0)^2} \cdot C, \tag{3.12}$$

where C is a constant. Thus fitting the ^{137}Cs data with the function above it is possible to obtain some initial values for d_0, d_1 and d_2.
On the other hand at d = 254 mm the summing correction is expected to be negligible, as a matter of fact the sum peak is not significantly higher than the background. Using the initial guesses for d_0, d_1 and d_2 and fitting the data acquired at 254 mm with the eq. 3.9 one obtains the values of parameters a, b and c.
The total efficiencies from the multi-prametric fit were compared to the experimen-

tal, calculated for the ^{60}Co, in order to check the fitting procedure. Additional constrains on the fitting procedure were applied as the decreasing trend of both the efficiencies and of their ratio (η_{fe}/η_{tot}) with increasing E_γ. The fitting function was forced to reproduce ^{137}Cs data, which are not affected by summing. The results are plotted in fig. 3.15. The best fit parameters are listed in table 3.4.

d_0	d_1	d_2	a	b	c	K_1	K_2	K_3
2.18	4.97	0.20	- 0.02	-0.455	-0.148	-1.560	-0.350	-0.177

Table 3.4: The multiparametric fit results.

3.3 Data Analysis and Results

Six different composition and thickness targets were irradiated by a high intensity proton beam at LUNA ($I \sim 50$ μ A), in order to investigate the ^{6}Li(p,γ)^{7}Be cross-section. The targets used are listed in tab. 3.5. The measurement on each target proceeded as following:

- The first run was acquired at $E_p \sim 290$ keV, the precise E_p was not the same for all targets. This energy was a reference energy to monitor the status of the target. Indeed the acquisition at the reference energy was repeated periodically during the measurement. In particular, the MAESTRO software allows to perform an online analysis, for example selecting a region of interest in the spectrum it can calculate a net area as the integral of the peak with a linear background subtraction. With the online net areas it was possible to immediately calculate the ratio between the counts in the peak of interest and the charge collected during the run, this ratio is referred as the experimental yield. Comparing the yield obtained for the first run with the following at the reference energy it was possible to have a preliminary estimation of the target degradation. As a matter of fact fixing the proton beam energy the experimental yield is directly proportional to the number of target atoms along the beam direction. From the online analysis it was observed that the Li_2O targets were more stable than the Li_2WO_4 targets. Indeed the online yield at the reference energy was almost constant during the whole measurement for the Li_2O targets, total charged collected ~ 7 C for each target. On the other hand the yield of the three Li_2WO_4 targets in tab. 3.5 dropped to the 88%, the 82% and the 94% respectively. The collected charge on these targets was 9C, 12C and 7C. The infinitely thick LiCl target was very stable during the measurement.

- The covered proton energy range was different for each target measurement, see tab. 3.5, and it was explored in steps of $\sim$10 keV starting from the high energies down to the lower. The only exception is the Li_2WO_4-4 target for which only few energies were measured because the high intensity of the beam degraded the target quite soon.
- During the lunch time and the night, long runs were launched at low energies. Because of the low counting rate and the low proton beam intensity at E_p <200 keV, long runs were required to have a good statistic.
- Completed the measurement for a target, this was dismounted and a fresh one was mounted on the target holder. Both the fresh and the irradiated targets were kept in a vacuum jar in order to prevent the Li hydroxidation by the air humidity.

A summary of the data acquired at LUNA is in tab. 3.5.

The analysis of the data collected at LUNA is still ongoing. However a complete

Target ID	E_p Range [keV]	Total Charge [C]
Li_2O-7	120 - 390	7.7
Li_2O-9	120 - 390	6.4
Li_2WO_4-3	102 - 393	9.1
Li_2WO_4-4	80 - 380	12.4
LiCl	76 - 379	8.7
Li_2WO_4-1	121 - 389	6.5

Table 3.5: The targets are sorted by irradiation order. For each target the proton beam energy range covered and the total charge collected are reported.

analysis was performed for the $^6Li_2WO_4$-1 target, see fig. 3.16, and it is described in the current section. The results presented are preliminary because the analysis must be extended to the other targets but it is self-consistent.

In order to reduce uncertainties coming from a not accurate knowledge of the target thickness and composition as well as of the collected charge run by run, it was decided as a first step to use a relative approach to derive the $^6Li(p,\gamma)^7Be$ S-factor. The relative method is presented in the following general description.
The Yield is defined as [3]:

$$Y = \frac{total\,number\,of\,nuclear\,reactions}{total\,number\,of\,incident\,beam\,particles} = \frac{N_R}{N_b}. \tag{3.13}$$

The quantity N_R can be calculated from the experimental spectra as the net counts in the peak of interest. Because the net counts we observed in the peak corresponds

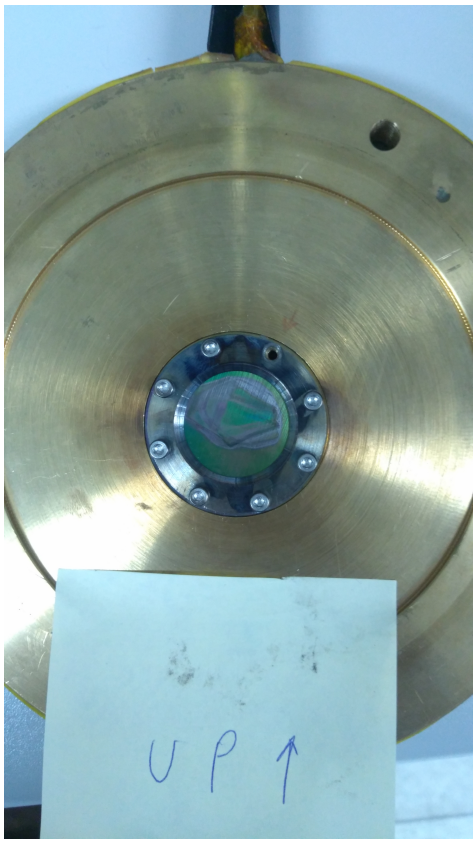

Figure 3.16: The $^{6}Li_2WO_4$-1 target after the irradiation at LUNA.

to the number of detected reactions, in order to get the total number of reactions the area of the peak must be corrected for the detector full-energy efficiency. In addition, in case of cascades, if only one transition peak is analyzed the net area must be divided by the intensity of that specific γ-ray (I_γ) to get the total reactions occurring. Thus, N_R can be defined as: $\frac{NetCounts}{\eta_{fe} \cdot I_\gamma}$. The total number of incident beam particles, N_b, can be obtained from the total collected charge. The Yield is related to the cross section by the following relation:

$$Y(E_p) = \int_{(E_p - \Delta E)}^{E_p} \frac{\sigma(E) \cdot P(E)}{\epsilon_{eff}(E)} dE = \int_{(E_p - \Delta E)}^{E_p} \frac{S(E_{cm}) \cdot e^{-2\pi\eta} \cdot P(E)}{\epsilon_{eff}(E) \cdot E_{cm}} dE, \tag{3.14}$$

where passing from the cross section, $\sigma(E)$, to the S-factor, $S(E_{cm})$, the following relation was used:

$$\sigma(E) = \frac{1}{E} e^{-2\pi\eta} S(E). \tag{3.15}$$

The initial beam energy is E_p while the total energy loss inside the target is ΔE. The quantity $e^{-2\pi\eta}$ is the Gamow factor, see sec. 1.1.1. $P(E)$ is the target profile

along the beam path inside the target itself. This was derived experimentally as already discussed in sec. 3.2.3. Finally the effective stopping power, $\epsilon_{eff}(E)$, is defined for compound X_aY_b as:

$$\epsilon_{eff} = \epsilon_X + \frac{n_Y}{n_X}\epsilon_Y, \tag{3.16}$$

where n_x is the number of active nuclei per square centimeter, in the current case the number of ^{6}Li nuclei. On the other hand n_y is the areal density of the inactive nucleus Y. The quantities $\epsilon_{x,y}$ are the stopping power for X and Y respectively. The stopping power, defined as the energy loss per unit length of a specific beam impinging on a specific target, can be calculated with SRIM [52]. The eq. 3.16 can be generalized to more complex target compounds. For the $^6Li_2WO_4$-1 target the ϵ_{eff} is:

$$\epsilon_{eff} = \epsilon_{Li} + \frac{n_{^7Li}}{n_{^6Li}}\epsilon_{Li} + \frac{n_W}{n_{Li}}\epsilon_W + \frac{n_O}{n_{Li}}\epsilon_O. \tag{3.17}$$

Because the dominant component of the stopping power is the electronic one, the stopping power does not change for isotopes of the same element, thus in the above equation the stopping power for Li isotopes is the same, ϵ_{Li}.
The S-factor is usually an almost constant function of the energy and thus as a first approximation eq. 3.14 can be written as:

$$Y(E_p) = S(E_{cm}) \cdot \int_{(E_p-\Delta E)}^{E_p} \frac{e^{-2\pi\eta} \cdot P(E)}{\epsilon_{eff}(E) \cdot E_{cm}}\, dE. \tag{3.18}$$

As described above the eq. 3.18 consists of all quantities that can be derived experimentally except the S(E), which is our goal.
In the present study eq. 3.18 was exploited in a relative approach. Indeed the γ-ray-to-α-particle branching ratio, BR(E) is defined as:

$$BR(E) = \frac{N_\gamma}{N_\alpha}, \tag{3.19}$$

where N_γ and N_α denote the total number of γ-rays and of α-particles from the ^{6}Li(p,γ)^{7}Be and the the ^{6}Li(p,α)^{3}He reaction respectively detected in each run. Looking at eq. 3.13 and taking in mind that the BR(E) is calculated for each run corresponding to a precise number of collected charge, it is clear that the BR(E) can be expressed as:

$$BR(E) = \frac{Y_{(p,\gamma)}}{Y_{(p,\alpha)}}. \tag{3.20}$$

Now using eq. 3.18 the following relation is obtained:

$$BR(E) = \frac{Y_{(p,\gamma)}}{Y_{(p,\alpha)}} = \frac{S_{(p,\gamma)}(E_{cm}) \cdot \int_{(E_p-\Delta E)}^{E_p} \frac{e^{-2\pi\eta} \cdot P(E)}{\epsilon_{eff}(E) \cdot E_{cm}}\, dE}{S_{(p,\alpha)}(E_{cm}) \cdot \int_{(E_p-\Delta E)}^{E_p} \frac{e^{-2\pi\eta} \cdot P(E) \cdot W(\theta,E)}{\epsilon_{eff}(E) \cdot E_{cm}}\, dE} \tag{3.21}$$

The ^{6}Li(p,γ)^{7}Be S-factor can be deduced from eq. 3.21, knowing or having derived experimentally all the other factors. The methods to calculate each quantity of eq. 3.21 are described below.

The $Y_{(p,\alpha)}$

The Yield can be obtained from the experimental spectra. In particular for the case of the $Y_{(p,\alpha)}$ an experimental Si spectrum is plotted in fig. 3.17a for the region of interest for the α-particles and the ^{3}He particles from the ^{6}Li(p,α)^{3}He. The spectrum was acquired at E_p = 121 keV with the $^{6}Li_2WO_4$-1 target. The left peak is produced by the α-particles while the right peak by the ^{3}He particles. The $Y_{(p,\alpha)}$ was obtained analyzing the ^{3}He peak because of the right tail of the α-particle peak going under the noise region at low energy. In order to get the total number of reactions the right peak was integrated in a proper region of interest. The background below the peak was observed to be negligible thus no background subtraction was needed. The area of the peak was then corrected for the efficiency of the Si detector at 103 mm which was found to be $4.5 \cdot 10^{-6}$ within 8% accuracy.

The $Y_{(p,\gamma)}$

The $Y_{(p,\gamma)}$ can be calculated by analyzing either the transition to the ground state peak or the transition to the first excited state peak. The analysis of the 429 keV peak is not recommended because the ^{10}B(p,$\alpha\gamma$)^{7}Be produces the same γ-ray. Indeed in previous experiments at LUNA the B contamination was found to be almost unavoidable in the setup. However in order to avoid the uncertainty coming from the relative intensities of γ_0 and γ_1, the $Y_{(p,\gamma)}$ was obtained using both the ground state transition and the first excited state transition.
As for the (p,α) channel the first step was to get the areas of the peaks corresponding to γ_0 and γ_1, the HPGe spectra acquired at E_p = 121 keV with the $^{6}Li_2WO_4$-1 target is reported in fig. 3.17b. The peak corresponding to the direct capture to the ground state is well resolved and it lays on a flat background except for the Compton continuum. This originates because γ-rays can be scattered by an atomic electron of the detector out of the crystal. Thus the final absorbed γ-ray will not produce a count in the full energy peak but at lower energies depending on how much energy was transmitted to the electron. The net counts in the peak were obtained integrating in a proper region of interest and then subtracting a linear background, fitted using the centroids of the background on the left and on the right of the peak, taking care of not including the Compton continuum in the left background centroid estimation.
The analysis of the γ_1 peak is less trivial. Indeed high energy γ-rays ($E_\gamma \geq 1022$ keV which corresponds to $2m_ec^2$) as $\gamma_{0,1}$ can create the e^-e^+ pair interacting with the

Ge crystal. The excess energy carried by the γ-ray is shared by the electron and the positron as kinetic energy. The positron annihilates immediately producing two gammas of 511 keV each with opposite direction. In case of intermediate size detector, as the current HPGe, there is the possibility that one of the positron annihilation γ-ray escapes from the detector and a count at $E = E_{\gamma_{0,1}} - 511\,keV$ is observed. This process populates the so called *first escape* peak of $\gamma_{0,1}$. If both the positron annihilation γ-rays escape from the detector a count at $E = E_{\gamma_{0,1}} - 1022\,keV$ populates the so called *double escape* peak [83]. The first escape peak of $\gamma_{0,1}$ and the double escape of $\gamma_{0,1}$ are visible in fig.3.17. As a matter of fact the γ_1 peak is only ~ 80 keV far from the *first escape* peak of γ_0, less than the peak width, see fig. 3.17. Being the HPGe resolution of ~ 2 keV at $E_\gamma = 1.3\,MeV$, distinguishing the transition to the first excited state peak from the γ_0 first escape peak should not be a problem. But it must be kept in mind that the non resonant proton capture peak shape represents the convolution of the cross-section and the target profile. Indeed while penetrating inside the target the beam loses energy and the rate of γ-rays production decreases proportionally to the exponential decrease of cross-section with decreasing beam energy. In addition to this the energy loss inside the target and also the γ-rays production depend on the target profile, as the stoichiometry and the active nuclei concentration along the beam path. The higher is the beam energy the deeper the beam can penetrate inside the target and the wider is the peak, see the HPGe spectrum acquired at $E_p = 270.3\,keV$ with the $^6Li_2WO_4$-1 target in fig. 3.18. Looking at fig. 3.18 is evident that in order to obtain the total counts corresponding to the γ_1 transition a method to estimate the γ_1 counts under the γ_0 first escape peak must be found.

For the present work the area of the γ_1 peak was estimated integrating the resolved part of the peak, indicated by the red vertical lines in fig. 3.19, and subtracting a linear background calculated from the average background level on the left and on the right of both γ_1 and the γ_0 first escape peaks, see fig. 3.19. Then γ_1 counts under the first escape peak were estimated fitting the tail of γ_1 peak with a line, see fig. 3.19a, and with an exponential, see fig. 3.19b. In the latter case both γ_1 peak and γ_0 first escape were fitted with a skewed gaussian which has an exponential tail on the left, in fig. 3.19b the total fit is indicated in magenta. The regions defined by the fits, the linear background and the left limit of the region of interest for the resolved peak, the yellow areas in fig. 3.19, were summed independently to the integral of the resolved peak leading to two different results. Then an average was performed to get the final area of the γ_1 peak. This method was applied for all the runs and it was found to work properly except for $E_p \sim 350\,keV$ because of the beam induced background by the already mentioned $^{19}F(p, \alpha\gamma)^{16}O$ reaction. The $^{19}F(p,\alpha\gamma)^{16}O$ reaction has a broad and strong resonance at $E_p = 340\,keV$ which produce a γ-ray at 6.13 MeV, close to the region of interest for the $^6Li(p,\gamma)^7Be$ reaction. A typical spectrum at proton beam energy close to that of the $^{19}F(p,\alpha\gamma)^{16}O$ resonance

is shown in fig. 3.20. The ^{6}Li(p,γ)^{7}Be γ-rays lay on the ^{19}F(p, $\alpha\gamma$)^{16}O Compton continuum. For $E_p \geq 380$ keV the beam induced background by the ^{19}F(p,$\alpha\gamma$)^{16}O reaction became negligible. Both γ_0 and γ_1 areas were corrected for the TCS, using η_{fe} and η_{tot} calculated from the functions described in sec. 3.2.5. The obtained areas were used to calculate $Y_{(p,\gamma_0)}$ and $Y_{(p,\gamma_1)}$ which were exploited to derive the branching ratio, *br*, of γ_0 and γ_1 defined as:

$$br = \frac{Y_{(p,\gamma_0)}}{Y_{(p,\gamma_1)}}. \tag{3.22}$$

The results for each proton energy investigated are in fig. 3.21. The present study results are compared with the branching ratio reported in He et al. 2013, blue line in fig. 3.21 and with the result reported in Switkowski et al. 1979, red line in fig. 3.21. A good agreement was found with the literature. The two data points, at $E_p = 349$ keV and at $E_p = 359$ keV, whose spectra showed strong beam induced background, are in agreement only with the value in Switkowski et al. 1979. In addition excluding these two data the branching ratio seems to be constant and a average value was calculated: 1.55 ± 0.02.
In order to calculate the ^{6}Li(p,γ)^{7}Be S-factor the total $Y_{(p,\gamma)}$ was calculated summing $Y_{(p,\gamma_0)}$ and $Y_{(p,\gamma_1)}$. Once having the $Y_{(p,\gamma)}$ and the $Y_{(p,\alpha)}$ for each run it was possible to calculate the BR(E).

The $S_{(p,\alpha)}$

Moving to the right side of eq. 3.21 the $S_{(p,\gamma)}$ is the unknown quantity to be derived, while $S_{(p,\alpha)}$ is the ^{6}Li(p,α)^{3}He S-factor which was taken from literature. As a matter of fact the ^{6}Li(p,α)^{3}He was studied by many groups and in a wide range of energy [79, 85, 86], see fig. 3.22. In order to use the eq. 3.21 for each run the $S_{(p,\alpha)}$ must be known at each proton energy. The $S_{(p,\alpha)}$ was studied in the range of energy of interest for the current measurement by Cruz et al. 2008, see fig. 3.22. In [85] the experimental data were fitted with a third degree polynomial, see fig. 3.22. The best fit result is: $3.522 - 4.423E + 4.918E^2 - 2.572E^3$ and it is reported in [87]. This function was used in the current approach.

The Gamow Factor

Moving to the integrals in eq. 3.21 the Gamow factor, $e^{-2\pi\eta}$, was express as [2]:

$$e^{-2\pi\eta} = e^{-31.29 \cdot Z_1 \cdot Z_2 \cdot \sqrt{\frac{\mu}{E_{cm}}}}, \tag{3.23}$$

where $Z_{1,2}$ are the atomic numbers of the projectile and the target respectively. The reduced mass of the system is defined as in sec. 1.1: $\mu = \frac{M_1 M_2}{M_1 + M_2}$. Finally E_{cm} is the projectile energy in the center of mass system in units of keV.

Target Characterization at HZDR

In order to calculate ϵ_{eff} for the $^6Li_2WO_4$-1 target, the composition must be known. In addition $P(E)$, the target profile along the beam path inside the target, is needed to derive the $S_{(p,\gamma)}$. These quantities were derived experimentally An independent method to calculate the target profile and the target composition run by run would be desirable but it was not possible for the present study as a matter of fact there are no resonances at energies explorable by LUNA in proton capture reactions on ^{6}Li. Thus the targets were characterized only after the measurement at LUNA. Indeed they were delivered to the Helmotz-Zentrum Dresden-Rossendorf laboratories in Dresden (Germany). Two Ion Beam Analysis techniques were exploited to get independent information on the composition, the target thickness and the target profile: the Nuclear Reaction Analysis (NRA) and the Elastic Recoil Detection Analysis (ERDA).
The ERDA was carried out by local researchers. The ERDA technique is one of the most useful tool to depth profile light elements ($1 \leq Z \leq 9$) [88]. ERDA uses high energy ($E_0 \sim 1\,MeV/amu$) heavy-ion beams to scatter and depth profile light target atoms, $M_1 > M_2$ in fig.3.23. In grazing incidence geometry, $\theta_1 \sim 90°$ in fig. 3.23 all the target particles lighter than the beam can be scattered outward and detected at angle θ_2 in fig. 3.23. However the beam particles too can be backscattered and in order to stop them before reaching the detector an absorber foil is positioned in front of the detector. The energy deposited on the detector by the scattered target particle (E_d in fig. 3.23) depends on the energy loss of the ion beam and of the scattered particle inside the target and also on the energy loss of the scattered target atom passing through the absorber. However, the lower is the E_d the deeper the scattering process took place. The resulting spectrum for a single element target is a continuum, which represents its abundance as a function of the depth of the target. In case of targets containing several elements these can be detected simultaneously in a single run with high probability of overlapping. In order to separate light target atoms from heavier target particles usually two or more detectors are used with different range foil.

In the current ERDA measurement a 43MeV $^{35}Cl^{7+}$ ion beam was used. Two detectors were exploited: one to detect carbon and oxygen positioned at 31° and the second devoted to H and Li detection at 41°. The 41° detector had a 18 μm thick Al foil to stop heavy recoils and scattered beam.
ERDA spectra can be easily analyzed to obtain full quantitative results, the yield of the detected particles is proportional to the concentration of that specific elements

and the distribution in energy can be converted as a distribution of the target element as a function of depth, see fig. 3.24 for the raw spectra for the $^6Li_2WO_4$ targets.. The results for the current study were obtained by a simultaneous fit of ERDA spectra using the program NDF v9.3g [89]. The results are reported in tab. 3.6. The ERDA analysis covered both fresh (in red in tab. 3.6) and irradiated targets. For two $^6Li_2O$ targets the ERDA was performed in two different areas of the target, inside the LUNA beamspot and outside it. The latter measurement is indicated with a * in tab. 3.6. The only fresh $^6Li_2WO_4$ target, namely Li_2WO_4-2, useful to check the composition before the irradiation at LUNA was so thick and rough that analysis became impossible.
Roughness and the presence of inhomogeneities inside the targets limited the accuracy of the measurement. A surface peak in carbon distribution was observed in $^6Li_2WO_4$ targets but the film appeared free from carbon impurities,see tab. 3.6, in addition the carbon values were obtained without any background subtraction. Because of these informations the carbon value was taken out form the analysis ant renormalizing the ERDA results for Li, O, H and W to 100% the final composition for the target analyzed in the current work was: 20% ^{6}Li, 1% ^{7}Li, 59% O, 10% W and 10% H. This is close to the nominal one (27.14% ^{6}Li, 1.43% ^{7}Li, 57.14% O and 14.29% W) keeping in mind the limited accuracy of the measurement. The ERDA results must be compared and completed with the NRA results for composition and thickness.

Target ID	Experimental Thickness [10^{15}atoms/cm^2]	H [%]	Li [%]	C [%]	O [%]	W [%]
Li_2O-5	4000	7	31	12	50	-
Li_2O-6	2300	5	27	15	53	-
Li_2O-7	6400	3	31	14	53	-
Li_2O-7*	6600	3	29	14	54	-
Li_2O-8	3300	5	27	15	53	-
Li_2O-9	3600	7	26	16	51	-
Li_2O-9*	3600	6	27	13	54	-
Li_2WO_4-1	3600	9	19	<6	54	9
Li_2WO_4-2	>4000	-	-	-	-	-
Li_2WO_4-3	2100	9	17	<7	56	10
Li_2WO_4-4	2400	11	16	<5	57	10

Table 3.6: The targets analyzed with ERDA technique. For some targets the ERDA was performed inside the LUNA beamspot and outside. The latter measurement is indicated by a * next to the target identification.

With the NRA it was possible to investigate the concentration of ^{6}Li along the beam path. In addition some indirect outputs on the target composition can be derived. For the present study was carried out performing a scan of a well known narrow resonance of the ^{6}Li(α,γ)^{10}B at 1175 keV ($\omega\gamma = 366 \pm 17$ meV and $\Gamma_r = 1.7$ eV) [90], see fig. 3.26. The NRA experiment was performed at a beamline of the 3MV Tandetron Accelerator of the Ion Beam Center at HZDR. A devoted setup was installed to host the LUNA target holder flange, see fig. 3.25. The flange was mounted at 55° w.r.t. the beam direction as during the measurement at LUNA. A copper tube was used in the same configuration as at LUNA to suppress the secondary electrons and to prevent the contamination of the target. A HPGe detector by Canberra was used to detect the γ-rays by the ^{6}Li(α,γ)^{10}B reaction.
The HPGe efficiency calibration was performed using three standard sources, namely the ^{60}Co, the ^{88}Y and the ^{137}Cs. The γ-ray used for the analysis corresponded to the transition from the 718 keV level to the ground state. Because of the HPGe size and the source-to-detector distance, of 7 cm, no summing correction was required in this case.

The target was irradiated at different energies starting from some keV below the resonance energy. For the present study the scan was performed with 5-10 keV steps but for the falling edge larger step were required. The beam with $E_b > E_R$ entering and passing through the target loses energy. At a certain target depth the beam energy will match the resonance energy and the corresponding cascade will be visible in the spectrum. The total yield is proportional to the number of active nuclei present at this depth. Increasing the energy of the beam more deeply the resonance is populated and the target explored. Before losing the right amount of energy to reach E_R non resonant reactions can take place in the target. The non resonant contribution must be taken into account. The resonance scan can be fitted with the following empirical function, the red line in fig. 3.26:

$$Y = Y_{max} \cdot \frac{1}{1 + e^{\frac{E_R - E_\alpha}{\delta_l}}} \cdot \frac{1}{1 + e^{\frac{E_\alpha - E_R - \Delta E}{\delta_r}}} + C. \tag{3.24}$$

Except for the beam energy, E_α, all the terms in equation 3.24 are free parameters, which however can be well constrained by the observational data. The Y_{max} is the maximum Yield of the scan. The resonance energy is E_R and ΔE is the total energy lost inside the target. The former corresponds to the x coordinate of the point at the half height of the left edge of the scan. The latter is the the width at half height of the whole scan plot. The $\delta_{l,r}$ determines the width of the left and the right edge of the scan respectively. C is an offset that accounts for the non-resonant contribution. Before converting the fitted scan in the profile of the target it must be corrected for the α-beam straggling, see sec. 2.2. The beam straggling may significantly affect the right edge of the scan. As a matter of fact straggling causes a decrease in the slope of the high-energy edge of the yield curve [3]. The fit obtained from

the experiemental data must be corrected for this effect because they were obtained irradiating the target with α-particles with energy between 1150 and 1450 keV while the measurement at LUNA exploited proton beams at an energy between 80 and 400 keV. The beam straggling effect can be analytically defined as [3]:

$$\Delta_{stragg} = 1.20 \cdot 10^{-9} \cdot \sqrt{\frac{Z_1 {Z_2}^2 (E_0 - E_R)}{\epsilon}} (keV). \tag{3.25}$$

$Z_{1,2}$ are the atomic numbers of the target and the projectile respectively. E_0 is the initial beam energy, thus $(E_0 - E_R)$ is the beam energy loss inside the target before reaching the exact resonance energy. ϵ is the stopping power. Once estimated the straggling effect using eq. 3.25, a typical value for $E_\alpha = 1400$ keV of Δ_{stragg} is 22 keV, the scan fit function becames:

$$Y = Y_{max} \cdot \frac{1}{1 + e^{\frac{E_R - E_\alpha}{\delta_l}}} \cdot \frac{1}{1 + e^{\frac{E_\alpha - E_R - \Delta E}{\sqrt{(\Delta_{stragg})^2 + (\Delta_{tar})^2}}}} + C, \tag{3.26}$$

where δ_r was expressed as $\sqrt{(\Delta_{stragg})^2 + (\Delta_t)^2}$. Δ_{stragg} is the already defined beam straggling while Δ_t is related to the particular depth profile of the target. The experimental data for the scan were fitted again by the eq. 3.26 and once the best parameters were fixed the beam straggling effect was subtracted together with the non resonant contribution, the offset C in eq. 3.26, thus obtaining the final profile in blue in fig. 3.26. The final parameters of the $^6Li_2WO_4$-1 target profile, reported in tab.3.7, provide information on the target which must be compared with those obtained by the ERDA analysis in order to proceed to the P(E) estimation and the $S_{(p,\gamma)}(E)$ calculation.

Y_{max} $[counts/part]$	E_R [keV]	δ_l	ΔE [keV]	Δ_{tar}
$(1.14 \pm 0.03) \cdot 10^{-11}$	1173±3	0.07±1	226±5	40±4

Table 3.7: The scan fit results for the $^6Li_2WO_4$-1 target.

The maximum Yield of the scan in case of thick target ($\Delta E >> \Gamma_R$), is defined as [3]:

$$Y_{max} = \frac{\lambda^2}{2} \cdot \frac{\omega\gamma}{\epsilon^r_{eff}} \cdot \frac{M_1}{M_1 + M_2}, \tag{3.27}$$

where $\omega\gamma$ is the resonance strength while $M_{1,2}$ are the target and projectile masses respectively. ϵ^r_{eff} is the effective stopping power at the resonance energy. Thus the eq. 3.27, once known Y_{max}, the resonance strength and other parameters of the reaction system, allows to derive the ϵ^r_{eff}, which is related to the target composition by

the eq. 3.16. This can provide some indirect information on the composition of the target. The expected ϵ^r_{eff} for the nominal composition is: $1.73{\cdot}10^{-13}\,\mathrm{eV\,cm^2/atom}$, which is not compatible with both results from ERDA and NRA, the discrepancy found was of about 20%. The ϵ^r_{eff} was found to be $(1.38 \pm 0.11) \cdot 10^{-13}\,\mathrm{eV\,cm^2/atom}$ analysing the NRA data and using eq. 3.27. On the other hand using the composition by ERDA the calculated ϵ^r_{eff} was $2.12 \cdot 10^{-13}\,\mathrm{eV\,cm^2/atom}$.

It must be noted that the ERDA results, as already described, are affected by high uncertainty. In addition both ERDA and NRA measurement were performed with the beam focused on the $^6Li_2WO_4$-1 LUNA beamspot. Referring to fig. 3.16, the beamspot corresponds to the most intense green coloured area but an halo is visible probably due to the heating of the target during the measurement. The ERDA and the NRA measureaments probably explored two different areas of the beamspot/halo characterized by different degradation of the target due to the irradiation or to the deliver from one laboratory to the other. To test this hypothesis a quick analysis of the NRA data for the $^6Li_2WO_4$-2 target was performed. The $^6Li_2WO_4$-2 target was not irradiated at LUNA, thus it should have the same composition as after the evaporation process. The ϵ^r_{eff} for this target was found to be $(1.63{\pm}0.13){\cdot}10^{-13}$ eV cm^2/atom, in agreement with the nominal one. Thus for the following analysis the nominal composition was used as well as for the calculation of ϵ_{eff} to be inserted in the $S_{(p,\gamma)}$ routine calculation.
The target thickness found fitting the NRA data was $\Delta E = 226\,\mathrm{keV}$ at 55°. This must be compared with the expected total nominal energy loss for a 130 μg/cm^2 thick $^6Li_2WO_4$ target. The ΔE was calculated at 55° as:

$$\Delta E = \frac{dE}{\rho dx} \cdot \rho \cdot \frac{1}{cos(55°)} = \frac{\epsilon \cdot \rho}{cos(55°)}, \tag{3.28}$$

where ϵ is the target compound stopping power and ρ is the nominal target density. The nominal energy loss was found to be about 60 keV lower with respect to the experimental ΔE, but this was something expected because the nominal thickness was a parameter not perfectly under control during the evaporation procedure. Using the eq. 3.28 it is possible to derive the $^6Li_2WO_4$-1 density to be compared with the one by ERDA, see tab. 3.6. Starting from the ΔE by the NRA a target density of (2900±57) 10^{15} atoms/cm^2 in disagreement with the density found by ERDA, 3600 atoms/cm^2. Because of the limited accuracy reported for the ERDA results in particular for the thick $^6Li_2WO_4$ targets the NRA result was maintained for the rest of the analysis.
In order to convert the profile obtained with the NRA, which is a function of the E_α, to a curve depending on the proton beam energy $P(E)$, which is the current study case, the following approach was used. The target profile was first converted to a function of the target depth. As a matter of fact the resonance scan can be expressed easily as a function of the energy lost by the beam inside the target before reaching the exact value of the resonance energy by the relation $\Delta E_\alpha = E_\alpha - E_R$.

This relation must be combined with the eq. 3.28 in an incremental calculation in dE to convert the target profile as a function of the target density. Finally exploiting again the eq. 3.28 but using the stopping power for the proton beam, for each proton beam energy measured at LUNA the target density was converted in the incremental energy loss of the beam penetrating inside the target. This last incremental calculation was inserted in the routine to calculate the ^{6}Li(p, γ)^{7}Be S-factor. It must be noted that in order to perform the incremental calculation the dependence on the beam energy of the ϵ must be know. For the present study the values of the stopping power for the α and the proton beam were fitted with a second degree polynomial in the region of interest for the measurement, see fig. 3.27. Once obtained $P(E)$, the number of active nuclei as a function of the proton energy energy loss, this was first was normalized to 1 and then it was inserted in the incremental calculation of the $S_{(p,\gamma)}(E)$.

The W(θ, E)

Having the target profile $P(E)$ and the nominal composition to calculate ϵ_{eff} as in 3.16, the last term to be derived in order to obtain the ^{6}Li(p,γ)^{7}Be S-factor is the angular distribution for the ^{6}Li(p,α)^{3}He reaction, $W(\theta, E)$ in eq. 3.21. Many groups studied the ^{6}Li(p,α)^{3}He angular distribution. It was found that W(θ, E) is dominated by the A_1 term, which has a dependence on the beam energy [79]. The data reported in [79] were fitted with a second degree polynomial function in the plane log(E)/A_1, see fig. 3.28. The dependence of A_2 on energy was directly reported in the paper. Both the curve are expressed below:

$$\begin{aligned} W(\Theta, E) \;=\; 1 + (-0.03 - 0.15 log(E_{cm}) + 0.037 log(E_{cm})^2) \cdot cos(\Theta) + \\ + (-0.03 - 0.0003 E_{cm}) \frac{1}{2} (3 cos(\Theta)^2 - 1). \end{aligned} \tag{3.29}$$

Results

All the above quantities were the inputs of the incremental calculation implemented in ROOT to get the ^{6}Li(p,γ)^{7}Be S-factor. The incremental calculation was performed for each run acquired at LUNA, excepted at the proton beam energy at which the ^{19}F(p,$\alpha\gamma$)^{16}O background was too high to perform an accurate analysis. The incremental calculation was performed from the initial beam energy down to the final beam energy after passing through the target. The measured Yield is thus proportional to the averaged value of the cross section over the interaction energies inside the target. But to evaluate the stellar reaction rates the local cross section values are needed. A method to assign an effective interaction energy the S-factor

is needed [91]. For the current study the effective energy was calculated as the weighted average energy between E_p and (E_p-ΔE):

$$E_{cm}^{eff} = \int_{(E_p - \Delta E)}^{E_p} \frac{e^{-2\pi\eta} \cdot P(E) \cdot E_{cm}}{e^{-2\pi\eta} \cdot P(E)} dE, \tag{3.30}$$

where the weight was $(e^{-2\pi\eta} \cdot P(E))$ the Gamow factor, which determines the cross section drop at low energies, multiplied by the target profile. The incremental calculation was stopped when the energy loss inside the target corresponded to a target depth of 10^{19} atoms/cm^2 in order to take into account the whole target. The results of the routine are shown in fig. 3.29 with red diamonds. The estimated total error on the calculated S factor is of about 11% and it derives from the sources in tab. 3.8 and described below.

- The statistical error was calculated for the $Y_{(p,\alpha)}$ as the square root of the counts in the ^{3}He peak. For what concern the $Y_{(p,\gamma)}$ the statistical uncertainty of the $\gamma_{0,1}$ peak areas were propagated for the TCS correction formulas and in order to be more conservative the peak areas were considered indipendent. The statistical uncertainty of γ_0 peak area, $\sigma_{A_{\gamma_0}}$, was obtained using the relation [58]:

  $$\sigma_{A_{\gamma_0}} = \sqrt{[A_{\gamma_0} + B \cdot (1 + n/2m)]}, \tag{3.31}$$

  where B is the backround beneath the peak while n and m are the numebr of channels used for the estimation of the peak integral and the background respectively. The latter is multiply by 2 because the background is estimated both on the left side and on the right side of the peak. The error on the γ_1 peak area was found calculating the half-difference between the two different area results obtained by the two fitting procedures used to estimate the contribution of counts under the γ_0 first escape peak.

- The total uncertainty of the η_{fe} was calculated combining the systematic error due to the HPGe repositioning and the error by the multi-parametric fit. Tha former was estimated to be 4%, see sec. 3.2.5. The latter was estimated considering the distribution of the residuals between the experimental data and the fit results for the efficiency at all positions and taking the interval where the 68% of the residual lays. This was found to be$\pm$ 2.3% giving, together with the uncertainty on the HPGe repositioning, a final error on the η_{fe} of 4.3%.

- The error on the η_{tot} was estimated as the mean value of the residual between the experimental value from the analysis of the ^{60}Co spectra and the fit results. This was found to be of 5.1%. Both the error on the η_{fe} and on the η_{tot} were combined with the statistical errors for $A_{\gamma_{0,1}}$ in order to get the total error on the $Y_{(p,\gamma)}$.

- The uncertainty of the Si efficiency was calculated with the propagation of the error on the 151 keV resonance strength [84], on the ϵ^r_{eff} [52] and on the Yield, see eq. 3.2. The total error on the Si efficiency is 7.7% and this must be combined with the statisical error on the $A_{^3He}$ in order to obtain the final error on the $Y_{(p,\alpha)}$.

- The error on the $S_{(p,\alpha)}$ was calculated taking into acount the distribution of the error on the literature data in the range of energy of interest for the current study [85]. The interval where the 68% of the errors lays was assumed as the $S_{(p,\alpha)}$ uncertainty.

- The angular correlation for the ^{6}Li(p,α)^{3}He reaction is dominated by the A_1 coefficient [79]. The error on this coefficient reported in literature were propagated through the defnition of $W(\theta, E)$. The final error on the angular correlation was found to be 1.6%.

- The possible effect of the uncertainty of the Si detector position was estimated assuming the Si 0.1 cm on the left and then on the right w.r.t. the nominal position. With this assumption θ changed of 0.01 rad and as a consequence the $W(\theta, E)$ changed. The new $W(\theta, E)$ was exploited to perform a new calculation of the $S_{(p,\gamma)}$ which differs from the nominal one by 0.3%.

- The $S_{(p,\gamma)}$ was calculated also assuming a box-like target and the discrepancy with the $S_{(p,\gamma)}$ calculated taking into account the profile of the target was assumed as the effect of the uncertainty of the target profile on the calculation of the ^{6}Li(p,γ)^{7}Be S-factor.

- The possible effect of the uncertainty of the composition of the target was estimated from the difference between the $S_{(p,\gamma)}$ calculated with the nominal composition and with the composition from the ERDA results.

- The uncertainty reported by SRIM for the stopping power of Li, W, and O were propagated in order to obtain the total error on the ϵ_{eff}.

3.4 Discussion

The comparison of the current experiment results and the results in literature clearly show that at E larger than 200 keV there is a good agreement with the experimental data reported in [71] and [78]. The resonance observed by [78] is not confirmed by the current study results, indeed the present $S_{(p,\gamma)}$ increases with decreasing proton energy, in qualitatively agreement with the theoretical expectation by [72]. The analysis must be completed by the results for the other targets in order to verify if

Source	Error
Statistical	1%-3%
η_{fe}	2.3%
η_{tot}	5.1%
HPGe position	4%
Si eff.	7.7%
$S_{(p,\alpha)}$	4.9%
$W(\theta, E)$	1.6%
Si position	0.3%
P(E)	0.3%
Target composition	0.2%
ϵ_{eff}	1.7%

Table 3.8: Error budget for the present ^{6}Li(p,γ)^{7}Be S-factor.

there is any systemetic effect due to target composition and thickness. The target degradation must be investigated more in detailed in order to provide an absolute measurement of the $S_{(p,\gamma)}$.

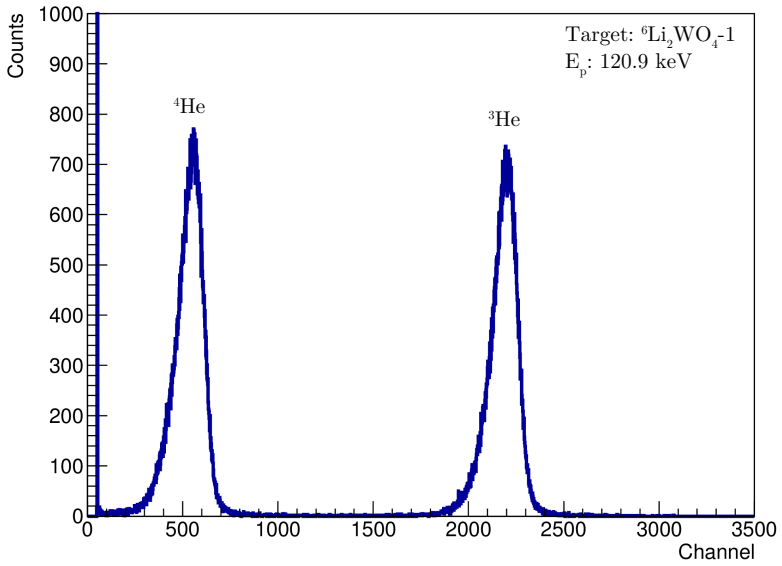

(a)

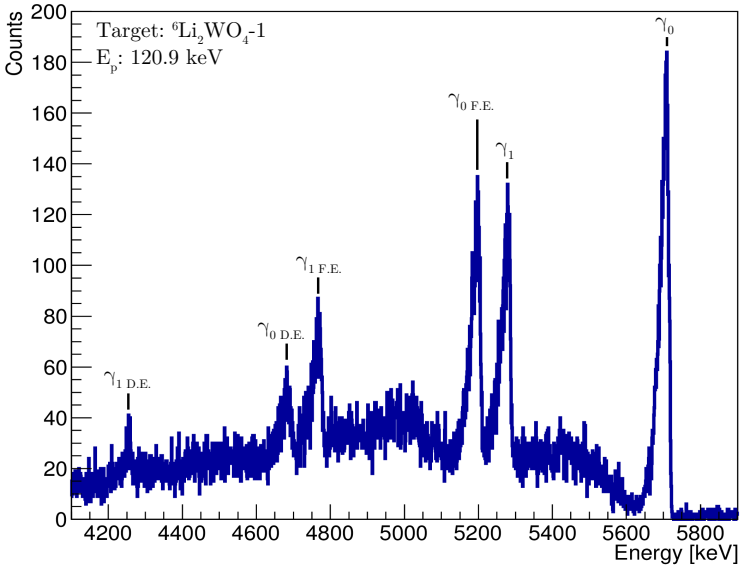

(b)

Figure 3.17: a): A Si spectrum acquired with the $^{6}Li_{2}WO_{4}$-1 target irradiated by a proton beam of 120.9 keV. b): An HPGe spectrum acquired with the $^{6}Li_{2}WO_{4}$-1 target irradiated by a proton beam of 120.9 keV.

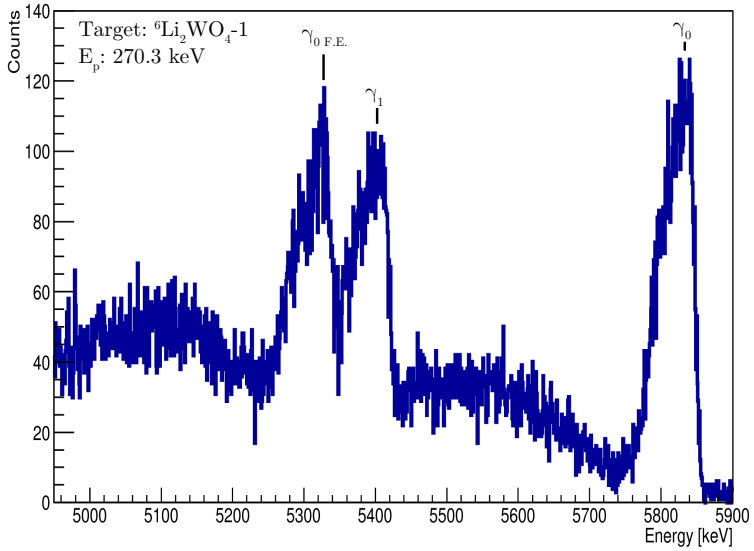

Figure 3.18: A HPGe spectrum acquired with the $^6Li_2WO_4$-1 target irradiated by a proton beam of 270.3 keV.

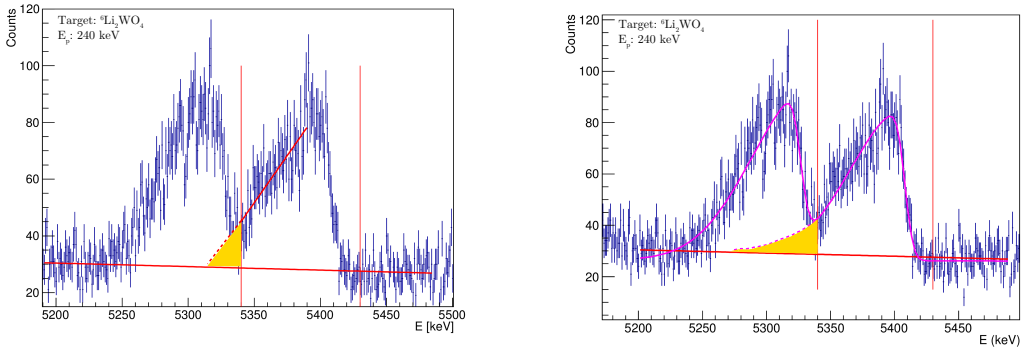

(a) (b)

Figure 3.19: a): Region of interest for the resolved peak limited by the red vertical lines. Linear bacgkround and linear fit of the tail of the γ_1 peak in red too. The counts under the γ_0 first escape peak found are indicated in yellow b): Region of interest for the resolved peak limited by the red vertical lines. Linear bacgkround in red too. The total fit for the two peaks is in magenta. The counts under the γ_0 first escape peak found are indicated in yellow.

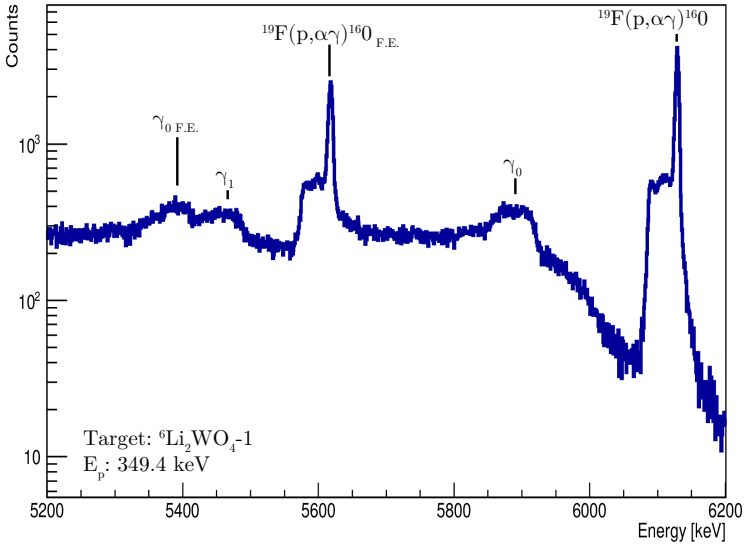

Figure 3.20: A HPGe spectrum acquired with the $^6Li_2WO_4$-1 target irradiated by a proton beam of 349.4 keV.

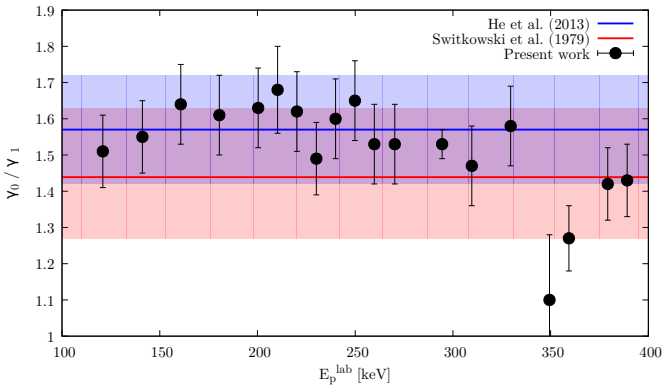

Figure 3.21: The results for the branching ratio obtained by the present analysis. The blue line is the value reported by He et al. 2013 for the branching ratio, in red the one reported in Switkowski et al. 1979. The uncertainties both for current results and literature values are reported. The black line is the average branching ratio calculated with the present data

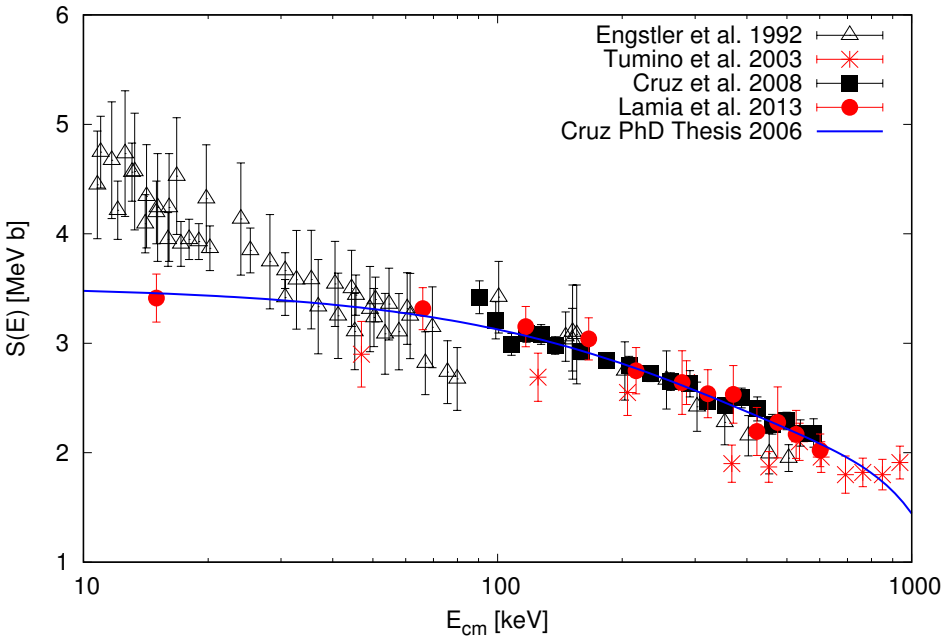

Figure 3.22: The ^{6}Li(p,α)^{3}He S-factor reported in literature.

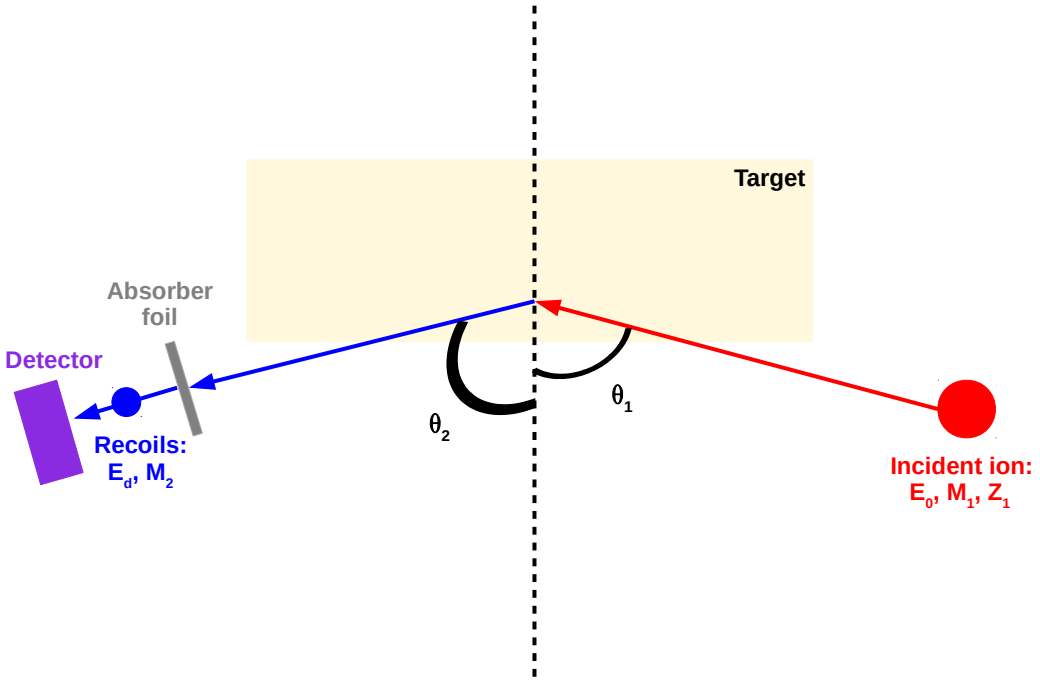

Figure 3.23: A schematic plot of ERDA technique.

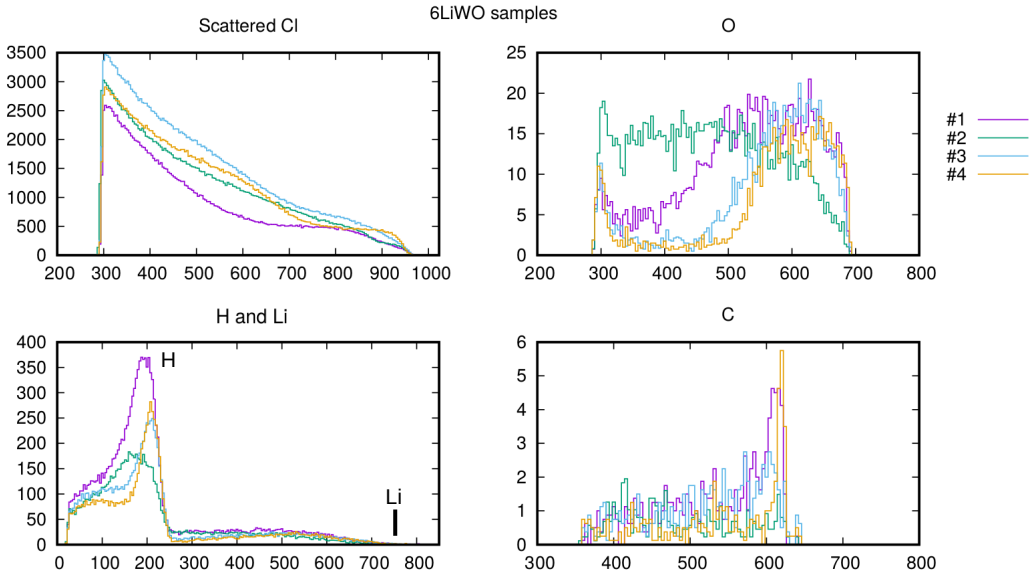

Figure 3.24: Raw spectra from the ERDA measurement on the $^{6}Li_2WO_4$ targets.

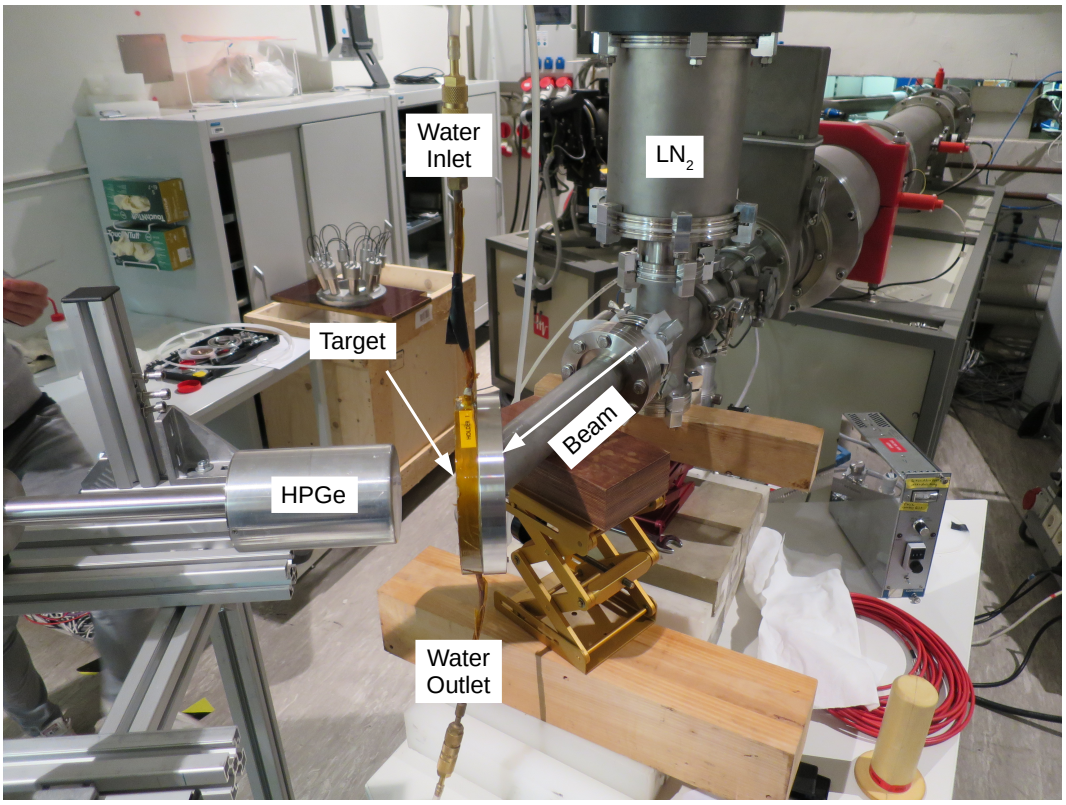

Figure 3.25: The scattering chamber and the detector used for the NRA measurement.

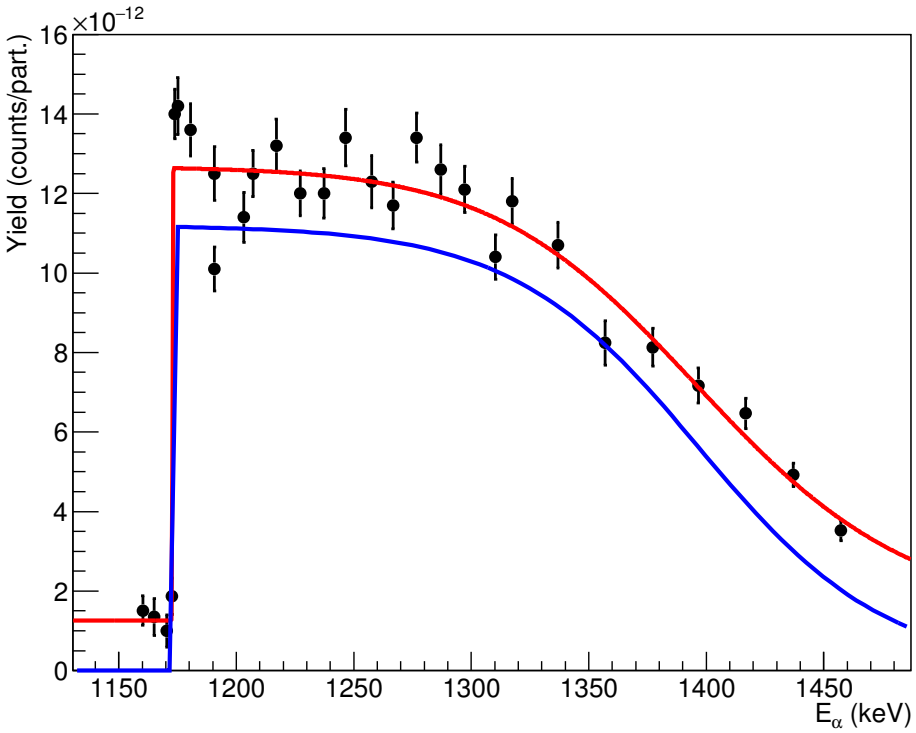

Figure 3.26: The scan of the 1175 keV ^{6}Li(α,γ)^{10}B resonance performed with target Li_2WO_4-1.

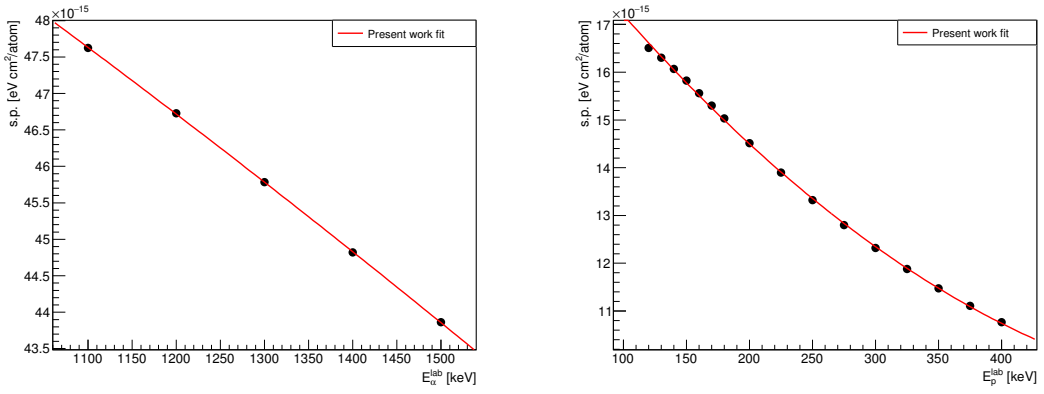

(a) (b)

Figure 3.27: a): Stopping power for α-beam at energies exploited for NRA. b): Stopping power for proton beam at energies explored at LUNA.

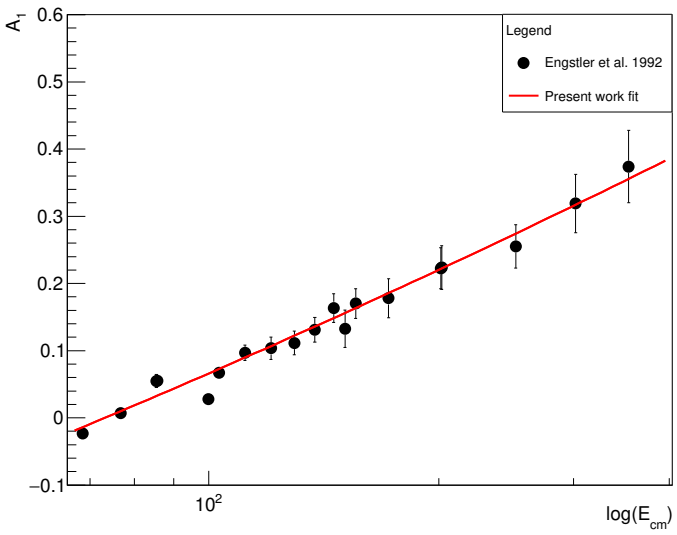

Figure 3.28: Experimental data for A_1 coefficient in the nergy range of interest for the current studyreported in [79]. The red line is the best fit second order polynomial function used for the present analysis

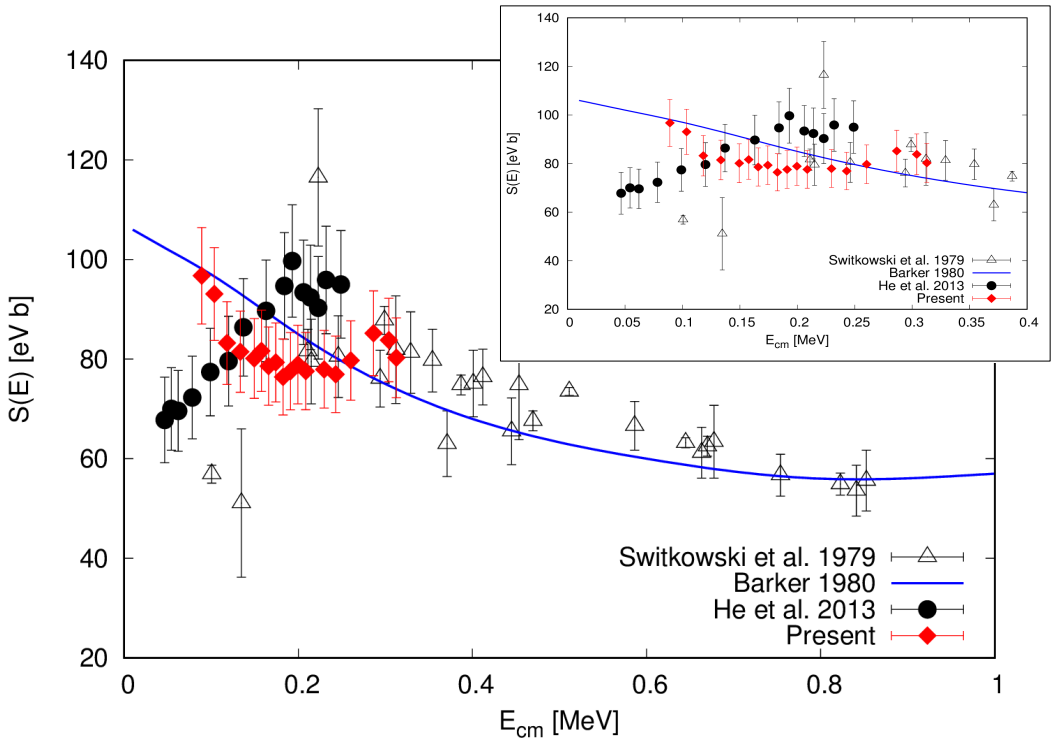

Figure 3.29: The results of the present work for the ^{6}Li(p,γ)^{7}Be S-factor compared with literature data.

Conclusion

In the present thesis the study of the ^{22}Ne(α,γ)^{26}Mg and the ^{6}Li(p,γ)^{7}Be reactions at LUNA have been described. LUNA, located at the Gran Sasso ultra-low background Laboratory, gives the unique opportunity of directly measuring the cross sections down to energies of astrophysical interest.
The ^{22}Ne(α,γ)^{26}Mg reaction has a fundamental role in the nucleosynthesis of s-nuclei in low-mass AGB stars and in massive stars being the competitor of the ^{22}Ne(α,n)^{25}Mg reaction an effective neutron source for s-process. The current work was focused on the study of the 395 keV resonance of the ^{22}Ne(α,γ)^{26}Mg reaction, whose strength was previously derived only by indirect measurements reporting very different results ($10^{-15} - 10^{-9}$ eV). This spread of values is the main source of the current high uncertainty on the ^{22}Ne(α,γ)^{26}Mg reaction rate. The study presented in this thesis was performed at the gastarget beamline of the LUNA400kV accelerator using an high efficiency setup based on six optically independent BGO crystals arranged in order to surround the scattering chamber leading to a covered solid angle of $\sim 4\pi$. An accurate comparison between the laboratory background spectra and the experimental spectra was performed. No significant signal was observed and the first direct upper limit was calculated for the 395 keV resonance, $\omega\gamma = 1 \cdot 10^{-10}$ eV. The new LUNA result has a great impact on the ratio between the ^{22}Ne(α,n)^{25}Mg reaction rate and the ^{22}Ne(α,γ)^{26}Mg reaction rate in the region of interest for neutron production during the He-burning in low-mass AGB stars and massive stars. With the new LUNA result the neutron production becomes effective at
T = 0.31 GK, in disagreement with all the previous results, with consequences on the predicted s-nuclei production in low-mass AGB stars and in massive stars. The second campaign of the ^{22}Ne(α,γ)^{26}Mg reaction study will be performed next year and the expected impact is either to detect the resonance or to decrease the limit by one order of magnitude making it irrelevant for nuclear astrophysics.
The ^{6}Li(p,γ)^{7}Be reaction is involved in many astrophysical scenarios, as depletion of ^{6}Li in pre-main and in main sequence stars and in the Big Bang Nucleosynthesis. Many groups studied this reaction in the past either using theoretical models either using direct measurements. A recent work claimed the discovery of a new resonance at $E_{cm} = 195$ keV, renewing the interest on this reaction. The claimed resonance would solve the problem of the ^{6}Li(p,α)^{3}He angular distribution and may affect the extrapolation at low energy of the ^{3}He(α,γ)^{7}Be cross section. The study performed at LUNA had the goal of investigating this resonance and to measure the ^{6}Li(p,γ)^{7}Be cross section down to low energies in order to better constrain the S-factor extrapolation at astrophysical energies. The experiment was performed at the solid target beamline of the LUNA400kV. Targets with different composition and thickness were irradiated in the proton energy range between 80 and 390 keV. An HPGe detector and a Si detector were used in order to detect both γ-rays and

α-particles produced by ^{6}Li(p,γ)^{7}Be and by ^{6}Li(p,α)^{3}He reactions, respectively. The analysis was performed exploiting a relative approach and the S factor was found to be in agreement with previous experimental results for E 200 keV. No evidence of the 195 keV resonance were found and the S-factor shows the same trend as predicted by theoretical models.
Finally, a further result I obtained (given in Appendix A) concerns the study of the astrophysical impact of the new LUNA rate of ^{22}Ne(p,γ)^{23}Na reaction. A sensitivity study was performed whose major result was a significant decrease of the uncertainty on the predicted ^{22}Ne and ^{23}Na ejecta by intermediate-mass AGB stars. In addition, the LUNA reaction rate gave rise to a predicted ^{23}Na ejecta with which for the first time we could reproduce the Na-O anticorrelation observed in Galactic globular clusters [92]. This last results is a textbook example of the strong impact of accurate direct cross section measurements on stellar models and on the following predictions on the chemical evolution of the Galaxy.

Appendix A

Astrophysical Impact of Underground Measurement

My master degree thesis and the very first part of my PhD time were devoted to the study of the ^{22}Ne(p,γ)^{23}Na reaction at LUNA. At that time the first experimental phase was already completed and the results published [24], while the second phase was ongoing.
During the first phase three new resonances were observed for the first time and for two of them more precise ^{23}Na excitation energies were found. New upper limits were obtained for other three resonances. These results were combined with those for higher energy resonances [93] leading to evaluate a new total reaction rate.
LUNA reaction rate lies between those of the main reaction rate compilations, hereinafter indicated as NACRE [42] and IL10 [44], see fig. 3.30. In particular the new reaction rate from LUNA increases by a factor of 3-5 with respect to IL10 at temperatures $0.12\,GK \leq T \leq 0.20\,GK$. For 0.08 GK < T < 0.25 GK, the 1σ lower limit of the new reaction rate is above the upper limit calculated by IL10. Another effect of LUNA results is the reduction of the uncertainty on the reaction rate with respect to NACRE. This is not the case comparing with IL10 because of the different treatment of two poorly constrained resonances.

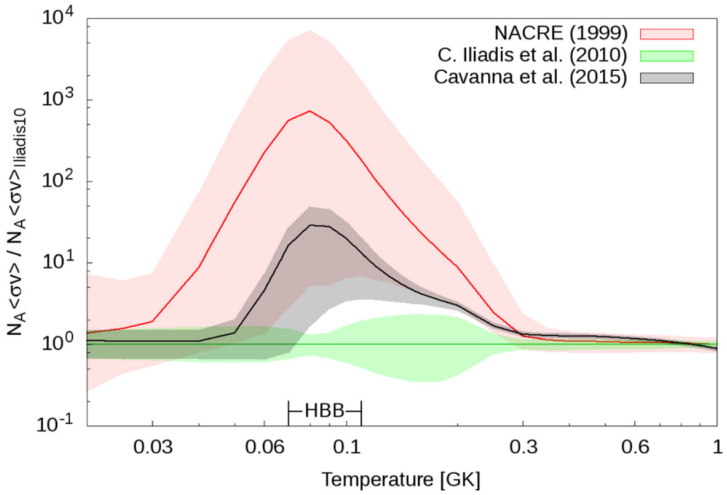

Figure 3.30: Total reaction rate normalized to IL10, as a function of tempera- ture, calculated by NACRE (red line), IL10 (green line) and [24](black line). The colored regions show the corresponding uncertainties. The range of temperatures relevant for the occurrence of HBB is also indicated [92].

One of my first activities during my PhD was to collaborate with the Padova astrophysicists of LUNA in order to investigate the astrophysical impact of the new reaction rate of ^{22}Ne(p,γ)^{23}Na [92]. Our study was focused on the case of low- and intermediate-mass stars which have a key role in the chemical evolution of the Universe. Indeed they are sites of rich nucleosynthesis and mixing events eventually followed by ejection of newly synthesized elements into the interstellar medium. Despite their importance that triggered remarkable efforts, large uncertainties still affects the predicted yields of various elements. Because of the new LUNA results for the ^{22}Ne(p,γ)^{23}Na we investigated only the ^{22}Ne and the ^{23}Na ejecta.
Stars with $M_i > 3 - 4\,M_\odot$ are known to experience the Asymptotic Giant Branch (AGB) stage and to activate the hot-bottom-burning process (HHB), see sec. 2.1 for more details. During the quiescent AGB evolution the temperature at the base of the convective envelope exceeds 0.06 GK and CNO, NeNa and MgAl cycles are activated. The NeNa cycle is the one responsible for the production of all isotopes between ^{20}Ne and ^{24}Mg. The large uncertainty affecting the few reaction rates involved in the NeNa cycle is the main source of the high (up to a factor 10) uncertainties of ^{22}Ne and of the ^{23}Na ejecta from AGB stars. In a recent systematic study it was demonstrated that most of these uncertainties are due to only ^{22}Ne(p,γ)^{23}Na reaction rate [94].
The aim of our work was to test the impact of LUNA revised reaction rate for ^{22}Ne(p, γ)^{23}Na reaction on the ^{22}Ne and ^{23}Na ejecta for a few sets of stellar models with initial masses in the range 3 $M_\odot$-6 $M_\odot$ and with three different values of metallicity Z_i = 0.0005, 0.006, 0.014. The results of the `PARSEC` [95] and `COLIBRI` [96] codes were compared with those obtained using NACRE and IL10 reaction rate. Finally the impact of LUNA on the suggested explanation of the O-Na anti-correlation in Galactic globular clusters stars as the action of primordial AGB and super-AGB stars was investigated, for more details see [97, 98] and references therein.
The main results of our study were the following: the ^{23}Na ejecta predicted with the LUNA reaction rate are lower than those derived with NACRE and larger than with IL10, see fig. 3.31. The opposite behavior applies to ^{22}Ne. Then the uncertanties on ^{23}Na and ^{22}Ne ejecta are significantly lower than those reported in similar studies, for example for ^{23}Na ejecta the relative uncertainty decreased from 100 in [94] to 1.25. Therefore we concluded that the remaining uncertainties of the chemical ejecta are mainly dominated by stellar evolution aspects.
Finally we inserted our results in the framework of the O-Na anti-correlation observed in stars of Galactic globular clusters. The new LUNA reaction rate, together with our reference AGB model were able to reproduce the Na-richest stars of the anti-correlation. Starting from this results, changing inputs for oxygen and CNO content, we could reproduce for the first time with AGB ejecta only the observed O-Na anti-correlation. However, this is not a exhaustive results and further quantitative analysis should be performed.

Anyway, our work is an illuminating example of the strong impact of precise direct measurement of cross section on astrophysical models and the following predictions on the chemical evolution of our galaxy as well as on the processes taking place in stars.

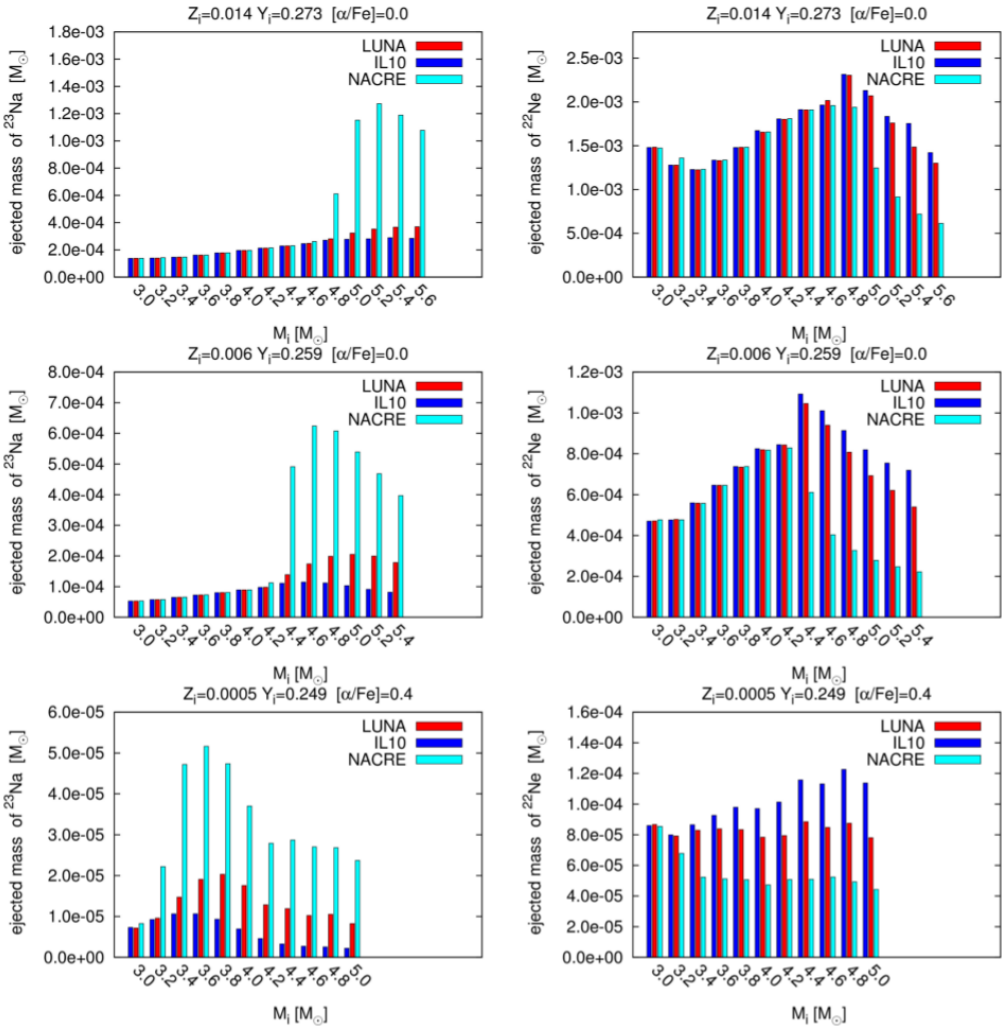

Figure 3.31: ^{22}Ne and ^{23}Na ejecta expelled into the interstellar medium by stellar winds during the AGB phase by intermediate-mass stars with HBB as a function of the initial mass and for three choices of the original metallicity, namely: $Z_i = 0.014$, 0.006 and 0.0005. The plots compare the results obtained with four choices for the ^{22}Ne(p,γ)^{23}Na rate (as indicated in the upper labels) [92].

Bibliography

[1] D. Clayton, *Handbook of Isotopes in the Cosmos: Hydrogen to Gallium*. Cambridge Planetary Science, Cambridge University Press, 2003.

[2] C. Rolfs and W. Rodney, *Cauldrons in the Cosmos: Nuclear Astrophysics*. Theoretical Astrophysics, University of Chicago Press, 1988.

[3] C. Iliadis, *Nuclear Physics of Stars*. Physics textbook, Wiley, 2007.

[4] M. Kunitomo, T. Guillot, T. Takeuchi, and S. Ida, "Revisiting the pre-main-sequence evolution of stars I. Importance of accretion efficiency and deuterium abundance," *Astronomy and Astrophysics*, vol. 599, p. A49, Mar. 2017.

[5] G. Hausser, "Cosmic ray-induced background in Ge-spectrometry," *Nuclear Instruments and Methods in Physics Research Section B: Beam Interactions with Materials and Atoms*, vol. 83, no. 1, pp. 223 – 228, 1993.

[6] P. Vojtyla, "Influence of shield parameters on cosmic-muon induced backgrounds of Ge γ-spectrometers," *Nuclear Instruments and Methods in Physics Research Section B: Beam Interactions with Materials and Atoms*, vol. 111, no. 1, pp. 163 – 170, 1996.

[7] K. Thomas, E. Norman, A. Smith, and Y. Chan, "Installation of a muon veto for low background gamma spectroscopy at the LBNL low-background facility," *Nuclear Instruments and Methods in Physics Research Section A: Accelerators, Spectrometers, Detectors and Associated Equipment*, vol. 724, pp. 47 – 53, 2013.

[8] A. Cagniant, G. Douysset, J.-P. Fontaine, P. Gross, and G. L. Petit, "An introduction to γ3 a new versatile ultralow background gamma spectrometer. Background description and analysis," *Applied Radiation and Isotopes*, vol. 98, pp. 125 – 133, 2015.

[9] T. Szücs et al., "An actively vetoed Clover γ-detector for nuclear astrophysics at LUNA," *European Journal A*, vol. 44, pp. 513–519, June 2010.

[10] H. Wulandari, J. Jochum, W. Rau, and F. von Feilitzsch, "Neutron flux at the Gran Sasso underground laboratory revisited," *Astroparticle Physics*, vol. 22, pp. 313–322, Nov. 2004.

[11] E. Aprile et al., "XENON100 dark matter results from a combination of 477 live days," *PhysRevD*, vol. 94, p. 122001, Dec. 2016.

[12] G. Heusser, "Low-radioactivity background techniques," *Annual Review of Nuclear and Particle Science*, vol. 45, pp. 543–590, 1995.

[13] A. Caciolli et al., "Ultra-sensitive in-beam γ-ray spectroscopy for nuclear astrophysics at LUNA," *European Physical Journal A*, vol. 39, pp. 179–186, Feb. 2009.

[14] D. Bemmerer et al., "Feasibility of low-energy radiative-capture experiments at the LUNA underground accelerator facility," *European Physical Journal A*, vol. 24, pp. 313–319, May 2005.

[15] M. Anders et al., "Neutron-induced background by an α-beam incident on a deuterium gas target and its implications for the study of the ^{2}H(α,γ)^{6}Li reaction at LUNA," *European Physical Journal A*, vol. 49, p. 28, Feb. 2013.

[16] C. Broggini, D. Bemmerer, A. Caciolli, and D. Trezzi, "LUNA: Status and prospects," *Progress in Particle and Nuclear Physics*, vol. 98, pp. 55–84, Jan. 2018.

[17] C. G. Bruno et al., "Improved direct measurement of the 64.5 kev resonance strength in the ^{17}O$(p,\alpha)^{14}$N reaction at LUNA," *Phys. Rev. Lett.*, vol. 117, p. 142502, Sep 2016.

[18] U. Greife et al., "Laboratory for Underground Nuclear Astrophysics (LUNA)," *Nuclear Instruments and Methods in Physics Research A*, vol. 350, pp. 327–337, Oct. 1994.

[19] R. Bonetti et al., "First Measurement of the ^{3}He(^{3}He,2p)^{4}He Cross Section down to the Lower Edge of the Solar Gamow Peak," *Physical Review Letters*, vol. 82, pp. 5205–5208, June 1999.

[20] C. Casella et al., "First measurement of the d(p,γ)^{3}He cross section down to the solar Gamow peak," *Nuclear Physics A*, vol. 706, pp. 203–216, July 2002.

[21] A. Formicola et al., "The LUNA II 400 kV accelerator," *Nuclear Instruments and Methods in Physics Research A*, vol. 507, pp. 609–616, July 2003.

[22] G. Gyürky et al., "^{3}He(α,γ)^{7}Be cross section at low energies," *Physical Review C*, vol. 75, p. 035805, Mar. 2007.

[23] D. Bemmerer et al., "Low energy measurement of the $^{14}N(p,\gamma)^{15}O$ total cross section at the luna underground facility," *Nuclear Physics A*, vol. 779, pp. 297 – 317, 2006.

[24] F. Cavanna et al., "Three New Low-Energy Resonances in the $^{22}Ne(p,\gamma)^{23}Na$ Reaction," *Physical Review Letters*, vol. 115, p. 252501, Dec. 2015.

[25] A. Boeltzig, A. Best, R. J. deBoer, A. DiLeva, G. Imbriani, M. Junker, and M. Wiescher, "$^{23}Na(p,\gamma)^{24}Mg$ Cross Section Measurements," in *European Physical Journal Web of Conferences*, vol. 165 of *European Physical Journal Web of Conferences*, p. 01006, Jan. 2018.

[26] F. Herwig, "Evolution of Asymptotic Giant Branch Stars," *Annual Review of Astronomy and Astrophysics*, vol. 43, pp. 435–479, Sept. 2005.

[27] R. G. Couch, A. B. Schmiedekamp, and W. D. Arnett, "S-PROCESS Nucleosynthesis in Massive Stars: Core Helium Burning," *The Astrophysical Journal*, vol. 190, pp. 95–100, May 1974.

[28] A. I. Karakas, M. A. Lugaro, M. Wiescher, J. Görres, and C. Ugalde, "The Uncertainties in the $^{22}Ne+\alpha$-Capture Reaction Rates and the Production of the Heavy Magnesium Isotopes in Asymptotic Giant Branch Stars of Intermediate Mass," *The Astrophysical Journal*, vol. 643, pp. 471–483, May 2006.

[29] C. Arlandini, F. Käppeler, K. Wisshak, R. Gallino, M. Lugaro, M. Busso, and O. Straniero, "Neutron Capture in Low-Mass Asymptotic Giant Branch Stars: Cross Sections and Abundance Signatures," *The Astrophysical Journal*, vol. 525, pp. 886–900, Nov. 1999.

[30] F. Kaeppeler et al., "Reaction rates for $^{18}O(\alpha,\gamma)^{22}Ne$, $^{22}Ne(\alpha,\gamma)^{26}Mg$, and $^{22}Ne(\alpha,n)^{25}Mg$ in stellar helium burning and s-process nucleosynthesis in massive stars," *The Astrophysical Journal*, vol. 437, pp. 396–409, Dec. 1994.

[31] R. Gallino, C. Arlandini, M. Busso, M. Lugaro, C. Travaglio, O. Straniero, A. Chieffi, and M. Limongi, "Evolution and Nucleosynthesis in Low-Mass Asymptotic Giant Branch Stars. II. Neutron Capture and the S-Process," *The Astrophysical Journal*, vol. 497, pp. 388–403, Apr. 1998.

[32] L. A. Willson, "Mass Loss From Cool Stars: Impact on the Evolution of Stars and Stellar Populations," *Annual Review of Astronomy and Astrophysics*, vol. 38, pp. 573–611, 2000.

[33] R. Reifarth, C. Lederer, and F. Käppeler, "Neutron reactions in astrophysics," *Journal of Physics G: Nuclear and Particle Physics*, vol. 41, no. 5, p. 053101, 2014.

[34] N. Prantzos, M. Arnould, and J.-P. Arcoragi, "Neutron capture nucleosynthesis during core helium burning in massive stars," *The Astrophysical Journal*, vol. 315, pp. 209–228, Apr. 1987.

[35] W. D. Arnett and J. W. Truran, "Carbon-Burning Nucleosynthesis at Constant Temperature," *The Astrophysical Journal*, vol. 157, p. 339, July 1969.

[36] C. M. Raiteri, M. Busso, R. Gallino, and G. Picchio, "S-process nucleosynthesis in massive stars and the weak component. II - Carbon burning and galactic enrichment," *The Astrophysical Journal*, vol. 371, pp. 665–672, Apr. 1991.

[37] M. Pignatari, R. Gallino, M. Heil, M. Wiescher, F. Käppeler, F. Herwig, and S. Bisterzo, "The Weak s-Process in Massive Stars and its Dependence on the Neutron Capture Cross Sections," *The Astrophysical Journal*, vol. 710, pp. 1557–1577, Feb. 2010.

[38] D. Yong, D. L. Lambert, and I. I. Ivans, "Magnesium Isotopic Abundance Ratios in Cool Stars," *The Astrophysical Journal*, vol. 599, pp. 1357–1371, Dec. 2003.

[39] D. Yong, F. Grundahl, D. L. Lambert, P. E. Nissen, and M. D. Shetrone, "Mg isotopic ratios in giant stars of the globular cluster NGC 6752," *Astronomy & Astrophysics*, vol. 402, pp. 985–1001, May 2003.

[40] Y. Fenner, B. K. Gibson, H.-c. Lee, A. I. Karakas, J. C. Lattanzio, A. Chieffi, M. Limongi, and D. Yong, "The Chemical Evolution of Magnesium Isotopic Abundances in the Solar Neighbourhood," *Publications of the Astronomical Society of Australia*, vol. 20, pp. 340–344, 2003.

[41] P. E. Koehler, "Constraints on the ^{22}Ne(α,n)^{25}Mg s-process neutron source from analysis of ^{nat}Mg+n total and ^{25}Mg(n,γ) cross sections," *Physical Review C*, vol. 66, p. 055805, Nov. 2002.

[42] C. Angulo et al., "A compilation of charged-particle induced thermonuclear reaction rates," *Nuclear Physics A*, vol. 656, pp. 3–183, Aug. 1999.

[43] R. Longland, C. Iliadis, G. Rusev, A. P. Tonchev, R. J. Deboer, J. Görres, and M. Wiescher, "Photoexcitation of astrophysically important states in ^{26}Mg," *Physical Review C*, vol. 80, p. 055803, Nov. 2009.

[44] C. Iliadis, R. Longland, A. E. Champagne, A. Coc, and R. Fitzgerald, "Charged-particle thermonuclear reaction rates: II. Tables and graphs of reaction rates and probability density functions," *Nuclear Physics A*, vol. 841, pp. 31–250, Oct. 2010.

[45] C. E. Moss, "Excitation energies of levels in ^{23}Na, ^{24}Mg and ^{26}Mg," *Nuclear Physics A*, vol. 269, pp. 429–442, Oct. 1976.

[46] U. Giesen et al., "The astrophysical implications of low-energy resonances in ^{22}Ne + α," *Nuclear Physics A*, vol. 561, pp. 95–111, Aug. 1993.

[47] C. Ugalde et al., "Experimental evidence for a natural parity state in ^{26}Mg and its impact on the production of neutrons for the s process," *Physical Review C*, vol. 76, p. 025802, Aug. 2007.

[48] R. Longland, C. Iliadis, and A. I. Karakas, "Reaction rates for the s-process neutron source ^{22}Ne + α," *Physical Review C*, vol. 85, p. 065809, June 2012.

[49] A. L. Sallaska, C. Iliadis, A. E. Champange, S. Goriely, S. Starrfield, and F. X. Timmes, "STARLIB: A Next-generation Reaction-rate Library for Nuclear Astrophysics," *The Astrophysical Journal Supplement Series*, vol. 207, p. 18, July 2013.

[50] F. Ferraro, M. P. Takács, D. Piatti, and V. Mossa et al., "A high-efficiency gas target setup for underground experiments, and redetermination of the branching ratio of the 189.5 keV ^{22}Ne(p,γ)^{23}Na resonance," *European Physical Journal A*, vol. 54, p. 44, Mar. 2018.

[51] D. Piatti, "Studio della reazione ^{22}Ne(p,γ)^{23}Na a energie astrofisiche," October 2015.

[52] J. F. Ziegler, M. D. Ziegler, and J. P. Biersack, "SRIM - The stopping and range of ions in matter (2010)," *Nuclear Instruments and Methods in Physics Research B*, vol. 268, pp. 1818–1823, June 2010.

[53] J. Görres, K. Kettner, H. Kräwinkel, and C. Rolfs, "The influence of intense ion beams on gas target densities," *Nuclear Instruments and Methods*, vol. 177, no. 2, pp. 295 – 303, 1980.

[54] J. Osborne, C. Barnes, R. Kavanagh, R. Kremer, G. Mathews, J. Zyskind, P. Parker, and A. Howard, "Low-energy behavior of the ^{3}He$(\alpha,\gamma)^7$Be cross section," *Nuclear Physics A*, vol. 419, no. 1, pp. 115 – 132, 1984.

[55] A. Caciolli et al., "Revision of the ^{15}N(p,γ)^{16}O reaction rate and oxygen abundance in H-burning zones," *Astronomy and Astrophysics*, vol. 533, p. A66, Sept. 2011.

[56] C. L. Melcher, "Scintillators for well logging applications," *Nuclear Instruments and Methods in Physics Research B*, vol. 40, pp. 1214–1218, Apr. 1989.

[57] R. Brun, F. Bruyant, M. Maire, A. C. McPherson, and P. Zanarini, "GEANT3," 1987.

[58] G. Gilmore, *Practical Gamma-ray Spectroscopy*. Wiley, 2011.

[59] S. Agostinelli et al., "Geant4—a simulation toolkit," *Nuclear Instruments and Methods in Physics Research Section A: Accelerators, Spectrometers, Detectors and Associated Equipment*, vol. 506, no. 3, pp. 250 – 303, 2003.

[60] M. Marta et al., "The ^{14}N(p,γ)^{15}O reaction studied with a composite germanium detector," *Physical Review C*, vol. 83, p. 045804, Apr. 2011.

[61] A. Coc, J.-P. Uzan, and E. Vangioni, "Standard big bang nucleosynthesis and primordial cno abundances after planck," *Journal of Cosmology and Astroparticle Physics*, vol. 2014, no. 10, p. 050, 2014.

[62] D. Clayton, *Principles of Stellar Evolution and Nucleosynthesis*. University of Chicago Press, 1983.

[63] R. D. Jeffries, *Pre-Main-Sequence Lithium Depletion*, p. 163. ESO ASTROPHYSICS SYMPOSIA, 2006.

[64] C. A. Bertulani, A. M. Mukhamedzhanov, and Shubhchintak, "The cosmological lithium problem revisited," *AIP Conference Proceedings*, vol. 1753, no. 1, p. 040001, 2016.

[65] M. Asplund, D. L. Lambert, P. E. Nissen, F. Primas, and V. V. Smith, "Lithium isotopic abundances in metal-poor halo stars," *The Astrophysical Journal*, vol. 644, no. 1, p. 229, 2006.

[66] M. Kusakabe, T. Kajino, and G. J. Mathews, "^{6}Li production by the radiative decay of long-lived particles," *Phys. Rev. D*, vol. 74, p. 023526, Jul 2006.

[67] S. C. Curran and J. E. Strothers, "The Excitation of γ -Radiation in Processes of Proton Capture," *Proceedings of the Royal Society of London Series A*, vol. 172, pp. 72–89, July 1939.

[68] K. L. Erdman et al., "Minutes of the pacific northwest meeting, held at seattle, washington, and on mount painter, july 7, 8, 9, and 10, 1954 (corresponding to bulletin of the american physical society, volume 29, no. 6)," *Phys. Rev.*, vol. 96, pp. 842–842, Nov 1954.

[69] S. Bashkin and R. R. Carlson, "Gamma Rays from Proton Bombardment of Li^6," *Physical Review*, vol. 97, pp. 1245–1249, Mar. 1955.

[70] J. B. Warren, T. K. Alexander, and G. B. Chadwick, "Reaction $Li^6(p,\gamma)Be^7$," *Physical Review*, vol. 101, pp. 242–245, Jan. 1956.

[71] Z. E. Switkowski, J. C. P. Heggie, D. L. Kennedy, D. G. Sargood, F. C. Barker, and R. H. Spear, "Cross section of the reaction ^{6}Li(p,γ)^{7}Be," *Nuclear Physics A*, vol. 331, pp. 50–60, Nov. 1979.

[72] F. C. Barker, "Neutron and proton capture by ^{6}Li," *Australian Journal of Physics*, vol. 33, pp. 159–176, May 1980.

[73] T. A. Tombrello, "A model to relate levels in an isobaric multiplet," *Physics Letters*, vol. 23, pp. 134–136, Oct. 1966.

[74] F. E. Cecil, D. Ferg, H. Liu, J. C. Scorby, J. A. McNeil, and P. D. Kunz, "Radiative capture of protons by light nuclei at low energies," *Nuclear Physics A*, vol. 539, pp. 75–96, Mar. 1992.

[75] K. Arai, D. Baye, and P. Descouvemont, "Microscopic study of the ^{6}Li$(p,\gamma)^7$Be and ^{6}Li$(p,\alpha)^3$He reactions," *Nuclear Physics A*, vol. 699, no. 3, pp. 963 – 975, 2002.

[76] R. M. Prior et al., "Energy dependence of the astrophysical S factor for the ^{6}Li(p,γ)^{7}Be reaction," *Phys. Rev.C*, vol. 70, p. 055801, Nov. 2004.

[77] J. Huang, C. Bertulani, and V. Guimarães, "Radiative capture of nucleons at astrophysical energies with single-particle states," *Atomic Data and Nuclear Data Tables*, vol. 96, no. 6, pp. 824 – 847, 2010.

[78] J. He et al., "A drop in the ^{6}Li$(p,\gamma)^7$Be reaction at low energies," *Physics Letters B*, vol. 725, no. 4, pp. 287 – 291, 2013.

[79] S. Engstler, G. Raimann, C. Angulo, U. Greife, C. Rolfs, U. Schröder, E. Somorjai, B. Kirch, and K. Langanke, "Isotopic dependence of electron screening in fusion reactions," *Zeitschrift fur Physik A Hadrons and Nuclei*, vol. 342, pp. 471–482, Dec. 1992.

[80] F. Barker, "Electron screening in reactions between light nuclei," *Nuclear Physics A*, vol. 707, no. 1, pp. 277 – 300, 2002.

[81] G. Dong et al., "Gamow shell model description of radiative capture reactions ^{6}Li$(p,\gamma)^7$Be and ^{6}Li$(n,\gamma)^7$Li," *Journal of Physics G: Nuclear and Particle Physics*, vol. 44, no. 4, p. 045201, 2017.

[82] Z.-H. Li, E.-T. Li, J. Su, Y.-J. Li, Y.-B. Wang, S.-Q. Yan, B. Guo, D. Nan, and W.-P. Liu, "New determination of the ^{7}Be ground state spectroscopic factor

and the ^{6}Li$(p,\gamma)^{7}$Be astrophysical $S(E)$ factors," *Chinese Physics C*, vol. 42, no. 6, p. 065001, 2018.

[83] G. F. Knoll, *Radiation detection and measurement; 4th ed.* New York, NY: Wiley, 2010.

[84] C. G. Bruno et al., "Resonance strengths in the ^{17,18}O(p, α)^{14,15}N reactions and background suppression underground. Commissioning of a new setup for charged-particle detection at LUNA," *European Physical Journal A*, vol. 51, p. 94, Aug. 2015.

[85] J. Cruz et al., "Experimental study of proton-induced nuclear reactions in ^{6,7}Li," *Journal of Physics G Nuclear Physics*, vol. 35, p. 014004, Jan. 2008.

[86] L. Lamia et al., "An Updated ^{6}Li(p,α)^{3}He Reaction Rate at Astrophysical Energies with the Trojan Horse Method," *The Astrophysical Journal*, vol. 768, p. 65, May 2013.

[87] J. D. N. Cruz, *Experimental Study of Proton Induced Nuclear Reactions in ^{6,7}Li.* PhD thesis, Universidade NOVA de Lisboa (Portugal, 2006.

[88] J. Tesmer and M. Nastasi, *Handbook of Modern Ion Beam Materials Analysis.* Mrs Symposium Proceedings Series, Materials Research Society, 1995.

[89] N. P. Barradas, C. Jeynes, and R. P. Webb, "Simulated annealing analysis of Rutherford backscattering data," *Applied Physics Letters*, vol. 71, pp. 291–293, July 1997.

[90] G. Gyürky, Z. Fülöp, E. Somorjai, G. Kiss, and C. Rolfs, "Absolute resonance strengths in the ^{6,7}Li(α,γ)^{10,11}B reactions," *European Physical Journal A*, vol. 21, pp. 355–358, 2004.

[91] A. Lemut, "The definition of the effective interaction energy for astrophysical relevant reactions," *European Physical Journal A*, vol. 36, pp. 233–241, May 2008.

[92] A. Slemer, P. Marigo, and D. Piatti et al., "^{22}Ne and ^{23}Na ejecta from intermediate-mass stars: the impact of the new LUNA rate for ^{22}Ne(p,γ)^{23}Na," *Monthly Notices of the RAS*, vol. 465, pp. 4817–4837, Mar. 2017.

[93] R. Depalo et al., "Strengths of the resonances at 436, 479, 639, 661, and 1279 keV in the ^{22}Ne(p,γ)^{23}Na reaction," *PhysRevC*, vol. 92, p. 045807, Oct. 2015.

[94] R. G. Izzard, M. Lugaro, A. I. Karakas, C. Iliadis, and M. van Raai, "Reaction rate uncertainties and the operation of the NeNa and MgAl chains during

HBB in intermediate-mass AGB stars," *Astronomy and Astrophysics*, vol. 466, pp. 641–648, May 2007.

[95] A. Bressan, P. Marigo, L. Girardi, B. Salasnich, C. Dal Cero, S. Rubele, and A. Nanni, "PARSEC: stellar tracks and isochrones with the PAdova and TRieste Stellar Evolution Code," *Monthly Notices of the RAS*, vol. 427, pp. 127–145, Nov. 2012.

[96] P. Marigo, A. Bressan, A. Nanni, L. Girardi, and M. L. Pumo, "Evolution of thermally pulsing asymptotic giant branch stars - I. The COLIBRI code," *Monthly Notices of the RAS*, vol. 434, pp. 488–526, Sept. 2013.

[97] F. D'Antona, E. Vesperini, A. D'Ercole, P. Ventura, A. P. Milone, A. F. Marino, and M. Tailo, "A single model for the variety of multiple-population formation(s) in globular clusters: a temporal sequence," *Monthly Notices of the RAS*, vol. 458, pp. 2122–2139, May 2016.

[98] P. A. Denissenkov and F. D. A. Hartwick, "Supermassive stars as a source of abundance anomalies of proton-capture elements in globular clusters," *Monthly Notices of the RAS*, vol. 437, pp. L21–L25, Jan. 2014.

Acknowledgments

I would like to thank all the people who contributed to this work. I am very grateful to Rosanna Depalo and Antonio Caciolli for all the things they taught me. Special thanks to Federico Ferraro, Marcell Takács and Thomas Chillery for their work at LUNA. I am thankful to Carlo Broggini for supervising my work and for his wise advice. I am also indebted to Roberto Menegazzo for the help. Finally, I would like to thank all the LUNA collaborators.